Wideband Multi-carrier Underwater Acoustic Communications: Synchronization under High Doppler

A Project Report

submitted by

SAMEER BABU T. P.

in partial fulfilment of the requirements
for the award of the degree of

MASTER OF TECHNOLOGY

DEPARTMENT OF ELECTRICAL ENGINEERING
INDIAN INSTITUTE OF TECHNOLOGY MADRAS.

MAY 2012

THESIS CERTIFICATE

This is to certify that the thesis titled **Wideband Multi-carrier Underwater Acoustic Communications: Synchronization under High Doppler**, submitted by **Sameer Babu T.P.**, to the Indian Institute of Technology, Madras, for the award of the degree of **Master of Technology**, is a bona fide record of the research work done by him under our supervision. The contents of this thesis, in full or in parts, have not been submitted to any other Institute or University for the award of any degree or diploma.

Prof. R. David Koilpillai
Research Guide
Professor
Dept. of Electrical Engineering
IIT-Madras, 600 036

Place: Chennai

Date: 1st May 2012

ACKNOWLEDGEMENTS

I sincerely express my gratitude to my guide, Prof. R. David Koilpillai for his guidance and the encouragement I received all along in spite of his heavy academic and administrative responsibilities at IIT Madras. He readily accepted my request to work in an area, namely Underwater Acoustic Communications, which is very much interested to me personally because of my background, and to my organization, NPOL Cochin, DRDO even though his major interests are in the area of DSP applications in Wireless. His open mind showed me how to look at the problems in many different ways, and try to solve them by seeking innovative methods.

Special thanks to Prof Arogyaswamy Paulraj, Professor (Emeritus) Stanford University for listening to my presentation at NCC-2012 and giving valuable feedback and insight in to the Doppler tolerance nature of hyperbolic frequency modulation based on his prior sonar experience.

I also express gratitude to my colleague at NPOL, Dr.Muralikrishna, Sc-E, for the several fruitful brainstorming sessions we had. The orientation of this work towards immediate practical applicability would not have been possible without the system development experience and many field trials conducted as part of my prior work at NPOL. I deeply indebted to all colleagues, team mates and people who had associated with me in all such endeavours at NPOL.

And last but not least, I would like to give thanks to all my family, specially my wife, who supported me either in the good or in the bad moments.

ABSTRACT

The demand for robust and high data rate Underwater Wireless Acoustic Communication Systems have increased significantly over last decade both from military and commercial sectors. The underwater acoustic channel is unique in many ways. Even if the velocities of underwater platform are low compared to terrestrial and aerial platforms, the velocity of the underwater information carrier, namely the longitudinal acoustic waves is 2×10^5 times lower than the transversal electromagnetic waves used in conventional RF communications above water. This makes problems due to Doppler, particularly unique among the many other challenges faced in underwater acoustic channels. Secondly, the channel should be treated as ultra wideband even with very low absolute bandwidth because of the low carrier frequency used based on attenuation criterion. Along with this, the fast fading nature of the channel makes the underlying principle in the design of underwater communication systems, and in particular multi-carrier systems, radically different from the conventional narrowband RF communication systems.

In this work, we have developed with a novel solution for the compensation of Doppler by re-sampling. The method is analysed under different scenarios both theoretically and by simulation. The trade-offs and performance bounds involved are clearly brought out.

A practical re-sampling filter with arbitrary re-sampling factor is designed and its performance is analysed. It is shown that re-sampling/rescaling in time essentially convert the wideband problem in to a narrowband problem. At this stage, conventional synchronization techniques applicable to narrowband OFDM systems have become relevant. Hence, a comparative study of such techniques available in literature has been carried out.

Doppler tolerant waveforms and modulation schemes are studied using analytical tools and simulation. Several unconventional techniques to combat uncertainties in Phase and Phase Derivatives are studies to further improve the robustness of the system.

In addition to simulation, the techniques are tried out in realistic environments with a Software Defined LabVIEW Test bed and with respect to the earlier field measurements carried at NPOL test facilities. Throughout the work, the focus was on the immediate practical applicability of the techniques to improve the performance and robustness of the existing operational system.

KEYWORDS: Underwater Acoustic Communication; Wideband Multi-carrier systems; Synchronization; Doppler; Re-sampling filter; Differential and Double Differential modulations.

TABLE OF CONTENTS

LIST OF TABLES

LIST OF FIGURES

ABBREVIATIONS

UWA	Underwater Wireless Acoustic
UWACS	Underwater Wireless Acoustic Communications Systems
OFDM	Orthogonal Frequency Division Multiplexing
BPSK	Binary Phase Shift Keying
QPSK	Quadrature Phase Shift Keying
DPSK	Differential Phase Shift Keying
DDPSK	Double Differential Phase Shift Keying
AF	Ambiguity Function
MF	Matched Filter
SNR	Signal to Noise Ratio
LFM	Linear Frequency Modulation
HFM	Hyperbolic Frequency Modulation
QFM	Quadratic Frequency Modulation
Log FM	Log-arithmetic Frequency Modulation
MLS	Maximal Length Sequence
FEC	Forward Error Correction
AUV	Autonomous Underwater Vehicles
UWB	Ultra Wide Band
ZP	Zero Padded
ML	Maximum Likelihood
CRLB	Cramer Rao Lower Bound
STO	Symbol Time Offset
CFO	Carrier Frequency Offset
CP	Cyclic Prefix
AWGN	Additive White Gaussian Noise
MSE	Mean Square Error
STBC	Space Time Block Codes
CSIT	Channel State Information at Transmitter

CSIR	Channel State Information at Receiver
ACF	Auto Correlation Function
PSD	Power Spectral Density

NOTATION

A	Attenuation
f	Frequency in Hz
ω	Angular frequency in rad/s
t	Time in sec
n	Index
v	Velocity in m/s
τ	Delay
c	Velocity of propagation
a	Time scale due to Doppler
T_s	Sampling Interval$= 1/F_s$
N_0	Noise Power Spectral Density
B	Bandwidth
χ	Ambiguity Function
R	Autocorrelation Function
ϵ	Carrier Frequency Offset
δ	Symbol Timing Offset
$I_m(x)$	Modified Bessel function of the first kind of order m and argument x.
P_E	Probability of Error
h	Impulse response

CHAPTER 1

Underwater Acoustic Communications: Design Considerations At the Physical Layer

1.1 Introduction

The field of digital communications has made rapid strides in the past two decades due to the availability of improved algorithms and high performance hardware platforms for their implementation (Feher, 1996). The increased commercial interest in RF wireless systems has also helped to accelerate the growth in this area. On comparing the performance improvement and services that are available in RF systems, it is seen that acoustic wireless systems lag significantly. A cursory glance at the reasons for the same reveal that there are both technological as well as lack of user demands which has resulted in this state. A matter of positive note is that this perception is improving rapidly with demands being made by various users desirous of having an underwater digital wireless communication system (Arthur B. Baggeroer, 1984), (Kilfoyle and Baggeroer, 2000),(Anthony G. Bessios and Caim, 1996),(Stojanovic, 1996), (M. Zheng *et al.*, 1999). Some of the main applications for an underwater wireless digital communication system are

- Naval Sensor Networks (Joseph A. Rice *et al.*, 2005),(J. G. Proakis *et al.*, 2001)
- Remotely Operated Underwater Vehicles (ROVs) (Eric T. M. Law *et al.*, 2002)
- Environmental Monitoring Systems
- Tsunami Early Warning Networks (Christian Meinig *et al.*, 2005), (Christian Meinig *et al.*, 2006)
- Oil and Natural Gas Exploration

The technological demands for each of these systems are quite different and each one has to be seen as a complete system in itself. The demand for this technology in the commercial area is also quite high because of the multi-disciplinary use of the same.

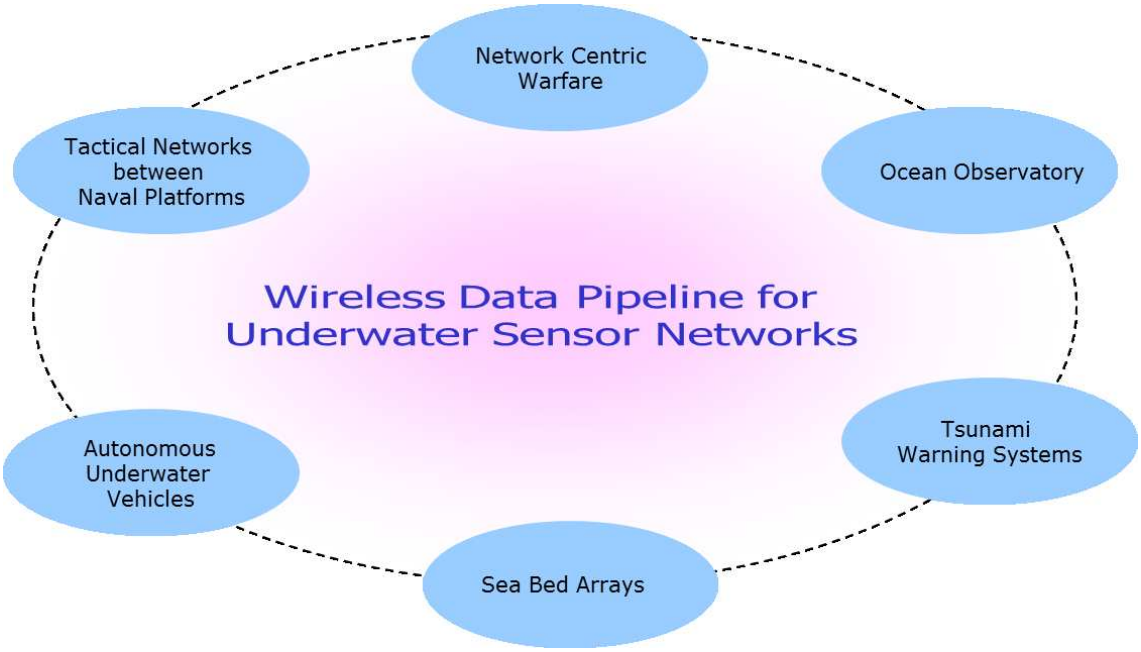

Figure 1.1: Applications of Underwater Modems

The key technology towards the realization of these applications is the availability of a wireless digital underwater modem capable of operating at various data rates and ranges. As an example of tactical application, a sensor network encompassing a submarine with a surface ship will be able to assess the overall threat scenario than a single platform. This is a classic example of the much talked off data fusion by interchanging radar / sonar displays or target position estimates and threat perceptions

Although radio and optical techniques can be used for very short range applications, acoustic signals are generally used for communicating underwater (UW). Radio waves that propagate underwater are the extra low frequency ones (30 Hz - 300 Hz), but these require very large antennas and extremely high transmission power (Coates, 1989). Optical techniques do not suffer from the problem of attenuation as much; however, they are affected by scattering. Moreover, optical communication requires very high precision in pointing a narrow laser beam in the right direction, which is still being perfected for practical use. Hence acoustic transmission looks like the best possible option for UW transmission for now. A comparison of the three transmission techniques in sea water is given in Table 1.1 (L. Liu *et al.*, 2008).

Table 1.1: Comparison of Acoustic, EM and Optical waves in seawater environments (L. Liu *et al.*, 2008)

	Acoustic	Electromagnetic	Optical
Nominal speed (m/s)	~ 1,500	~ 33,333,333	~3 3,333,333
Power Loss	> 0.1 dB/m/Hz	~28dB/1km/100MHz	∝ turbidity
Bandwidth	~ kHz	~ MHz	~ 10-150 MHz
Frequency band	~ kHz	~ MHz	~ 10^{14}–10^{15} Hz
Antenna size	~ 0.1 m	~ 0.5 m	~ 0.1 m
Effective range	~ km	~ 10 m	~ 10-100 m

1.2 Channel Measurements

The measured impulse response in a mini acoustic tank (at NPOL Cochin) with Tx-Rx separation of 4m and both placed at 1.5m depth from surface water level is shown in the Fig. 1.2. A half sine/cosine is used as an approximation for impulse as it can be generated using standard function generator. The impulse response can be directly viewed in an oscilloscope without any further processing as against the cross correlation operation required in the case of chirping. But when the Tx-Rx separation is moderate to high, this method won't work because of the reduction in SNR and chirping is preferred. The acoustic transducers used were directional with a beam width of 90^0. The top waveform in Fig. 1.2 is the transmitted impulse signal and the bottom waveform is the corresponding response. It can be well-approximated as a one-sided exponential power delay profile commonly encountered in RF channels. The average and RMS delay spread are the same for exponentially distributed power delay profiles (Goldsmith, 2005) and in this case it is approximately 30ms. The second step was to measure the channel frequency response. We transmitted a maximal length sequence (MLS) of length 218 and estimated the power spectral density of the recorded the signal (Mommertz and Muller, 1995). The power spectral density gave us an estimate of the channel's magnitude response characteristics which is shown in Fig. 1.3. This frequency response measurement was carried out in a large acoustic tank (at NPOL Cochin) with a Tx-Rx separation of 40m and both placed at a depth of 9m from the surface water level using the same acoustic transducers mentioned earlier.

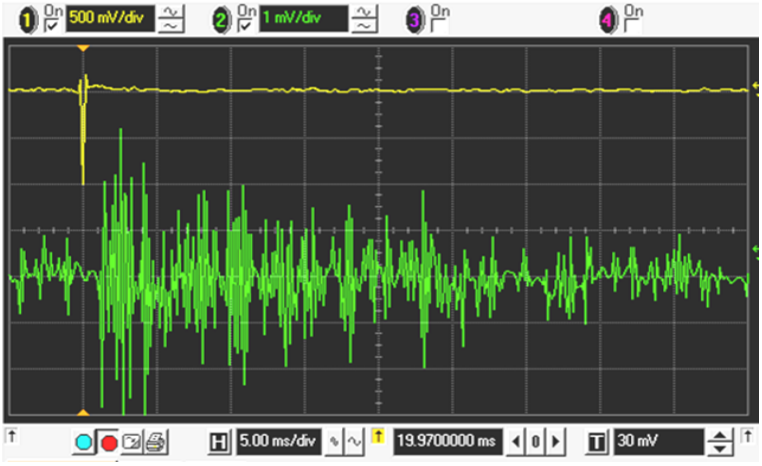

Figure 1.2: Impulse response of UWA channel: Oscilloscope Measurement (X-axis scale: 5ms/div)

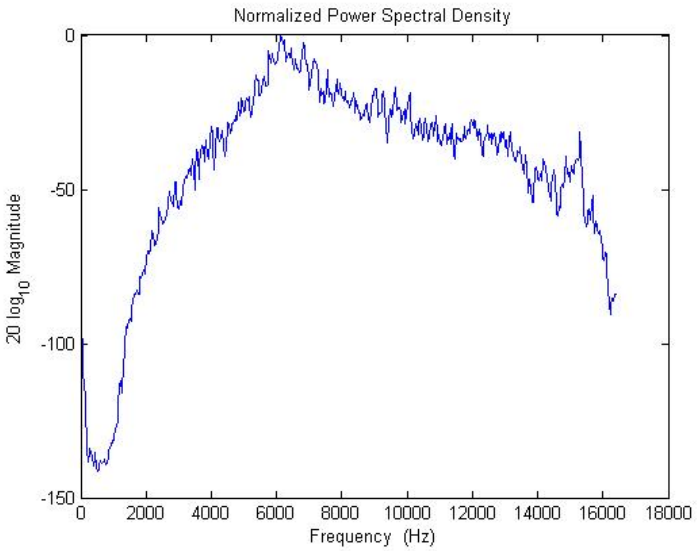

Figure 1.3: Frequency Response of UWA channel

1.3 Problems and Possible Solutions for Underwater Channels

The Table 1.2 (Anthony G. Bessios and Caim, 1996) compares the underwater acoustical channel to terrestrial RF channels. It is important to note the large multipath time dispersion and hence low coherence bandwidth. The underwater channel is typically a double spread channel in that it has both time dispersion and frequency dispersion. Due to high delay spread, spectral nulls will be present in the channel transfer function. The channel will exhibit both frequency selective fading and fast fading. The total available bandwidth will be constrained by the transducers used as well as the range. The underwater channel has the combination of the worst properties of both terrestrial cellular channel (high multipath and fading) and satellite channel (low SNR).

Table 1.2: Comparison of Underwater channels and RF channels (Anthony G. Bessios and Caim, 1996)

Channel	Coherence Bandwidth	Delay Spread	Doppler Spread
Troposcatter	1MHz	1μs	0.1 -10 Hz
Ionosphere	100Hz-10kHz	100μs – 10ms	0.1Hz – 100Hz
Outdoor	1MHz	1μs	10Hz
Indoor	1-10 MHz	0.1 – 0.5 μs	-
Underwater Acoustics	*0.3-Several Hz*	*0.3ms – 3s*	*3 – 60Hz*

There is significant difference between the behaviour of horizontal and vertical (e.g. sea bed to sea surface or vice versa) transmission channels (Stojanovic, 1996). The horizontal channel is characterized by very high delay spreads and frequency selective fading. The vertical path on the other hand is much more constrained with respect to delay spread and the data rates achievable in vertical channel can be an order of magnitude greater than those for the horizontal channels. Table 1.3 list the major problems and possible solutions for UWA channels.

Table 1.3: Major problems and possible solutions for UWA channels

Problems	Solutions
▪ Existence of Spectral Nulls ▪ Existence of Fast Fading	Error Coding + Interleaving + Multi Carrier
▪ Existence of High Delay Spread ▪ Complexity of Adaptive Equalization	Adjustable Cyclic Prefix Length (Guard Time) Selection
▪ Impracticality of Coherent Modulation	Differentially Coherent Modulation

1.4 System Design

Fig. 1.5 gives the overall block schematic of the transmitter and receiver. The binary data is first applied to a rate 1/2 convolutional encoder. We are using the IS95 standard adopted polynomial for the encoding. The encoded data is then passed to an interleaver. The interleaved pair of bits are mapped into the QPSK constellation with Gray encoding so as to reduce the probability of bit error for a given Symbol Error. It is based on the fact that the most likely symbol errors result in one bit error only. Hence, Gray mapping is used as shown in Fig. 1.4. The complex number symbols are so chosen for ease of generation of differential symbols.

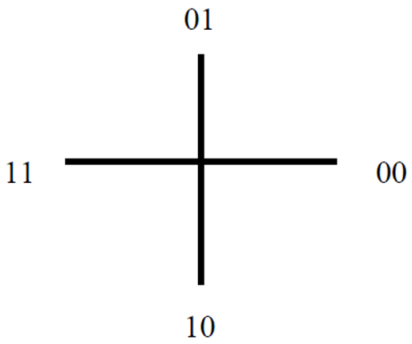

00	1
01	j
10	-j
11	-1

Figure 1.4: Gray Mapping of Symbols

The information is encoded as a change of phase with respect to the phase of the previous symbol on the same sub-carrier. The differential encoding itself is carried out by multiplication of the complex symbol with the previous complex symbol. For this purpose, a block of initial reference symbols is placed at the beginning of the data blocks. The insertion/removal of CP and other synchronization aiding waveforms are

not shown in the Fig. 1.5. The details of Differential encoding and synchronization will be discussed in depth in later chapters.

For our experiments we used 95 or 190 carriers in the band 6 - 9 kHz or 6 - 12 kHz range. Thus one OFDM symbol contained information mapped from either 190 bits or 380 bits.

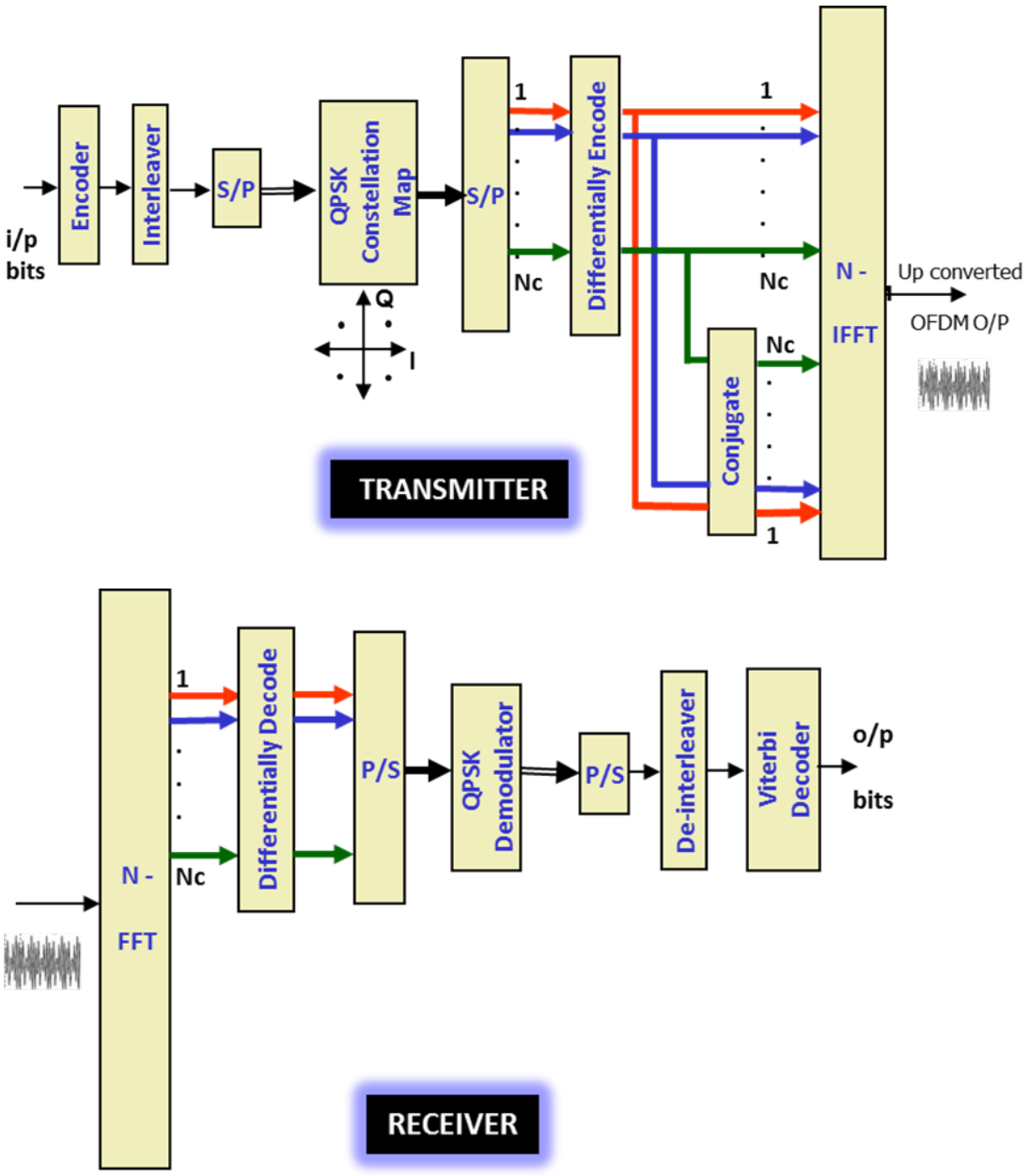

Figure 1.5: OFDM Communications System : Transmitter and Receiver

The receiver consists of the OFDM demodulator implemented using FFT followed by the DQPSK demapping block. The demodulated data is then de-interleaved and applied to the error correction block. The FEC decoding and error correction is done using the Viterbi algorithm. The depth of the trellis was kept as 150 after repeated trials

based on the observed results. The key design parameters are given in Table 1.4

Table 1.4: System Specifications

Modulation	DQPSK over OFDM
Error Control Coding	Convolutional Encoder (IS-95 std): • Rate ½, Constraint Length = 9 • Min. Free Distance =12 • Polynomial: $G_1(x) = x^8 + x^7 + x^5 + x^3 + x^2 + x + 1$ $G_2(x) = x^8 + x^4 + x^3 + x^2 + 1$
Interleaver	Block interleaver (1024 bits)
# of sub carriers	95 Carriers in the band 6 to 9 KHz
Data Rate	300 bps - 3kbps
Spectral Efficiency	0.34-1.8 bits/s/Hz
Viterbi Algorithm	Trellis Depth 150
Mobility Support	± 3 m/s

Fig. 1.6 illustrate the power spectral density recorded at the transmitter side (before the power amplifier) of the OFDM waveform. It can be seen that the band 6 - 9 kHz is used entirely by the system.

OFDM schemes performs very poorly under mobile conditions when Inter Carrier Interference(ICI) induced by the Doppler Effect. The challenges and mitigation techniques in the presence of Doppler are the major topic of study in this work and the details will be presented in the following chapters.

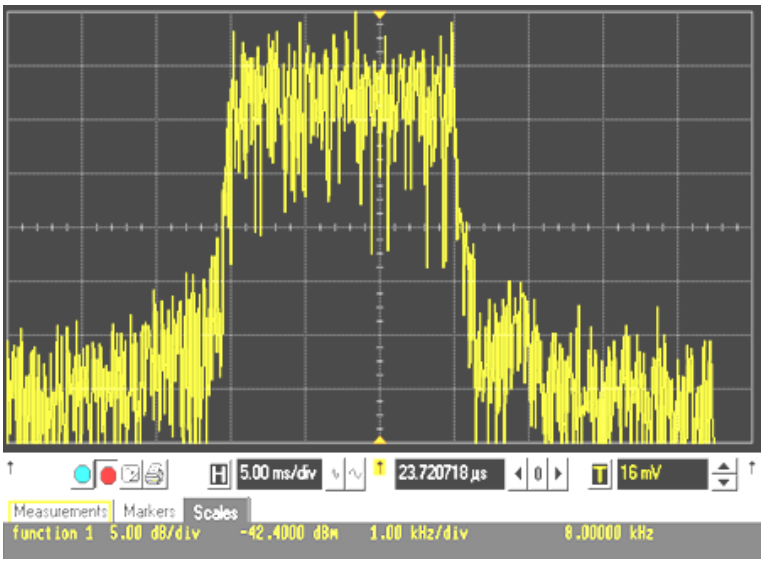

Figure 1.6: Measured Spectrum of OFDM signal at Transmitter in the band 6-9kHz viewed on Agilent Spectrum Analyzer

CHAPTER 2

Wideband Multi-carrier Underwater Acoustic Communications under High Doppler

Motion of the transmitter or receiver contributes to the changes in the channel response. This occurs through the Doppler effect which causes frequency shifting as well as additional frequency spreading. The magnitude of the Doppler effect is proportional to the ratio $a = v/c$ of the relative transmitter/receiver velocity to the speed of sound. Since the speed of sound is very low as compared to the speed of electromagnetic waves, motion-induced Doppler distortion of an acoustic signal can be extreme. The only comparable situation in radio communications occurs in the Low Earth Orbiting satellite systems, where the relative velocity of satellites flying overhead is extremely high. (The channel there, however, is not nearly as dispersive.) Autonomous underwater vehicles (AUVs) move at speeds that are on the order of few m/s, but even without intentional motion, underwater instruments are subject to drifting with waves, currents and tides, which may occur at comparable velocities. In other words, there is always some motion present in the system, and a communication system has to be designed taking this fact into account. The major implication of the motion-induced distortion is on the design of synchronization algorithms.

As the transmitter and receiver move relative to each other, the distance between them changes, and so does the signal delay. As a consequence, the leading edge of a transmitted signal may experience one delay, while the trailing edge will experience another. Focusing on a single path, and neglecting the path dispersion, let us look at a single pulse $g(t)$ modulated onto a carrier of frequency f_c. For a constant velocity v, the received signal is

$$s'(t_0 + t) = s(t_0 + t - \frac{l(t_0) - vt}{c}) \tag{2.1}$$

where $l(t_0)$ is the distance travelled by the signal arriving at t_0. Setting this time as the

reference at the receiver, we have that $r(t) = s(t_0 + t)$, i.e.,

$$r(t) = s(t + at - \tau) = \Re\{g(t + at - \tau)e^{j2\pi f_c(t+at-\tau)}\} \tag{2.2}$$

where $\tau = l(t_0)/c - t_0$ and $a = v/c$. With respect to the centre frequency f_c, the baseband received signal is

$$f(t) = e^{-j2\pi f_c t\tau} g(t + at - \tau)e^{j2\pi a f_c t\tau} \tag{2.3}$$

Not counting the phase $2\pi f_c\tau$, this signal is distorted in two ways: first, it is scaled in time by $(1 + a)$, so that a transmitted pulse of duration T is observed at the receiver as having duration $T/(1 + a)$. Equivalently, its bandwidth B is observed as $(1 + a)B$. Second, a frequency offset af_c is introduced. The first type of distortion accounts for motion-induced Doppler spreading, while the second accounts for Doppler shifting.

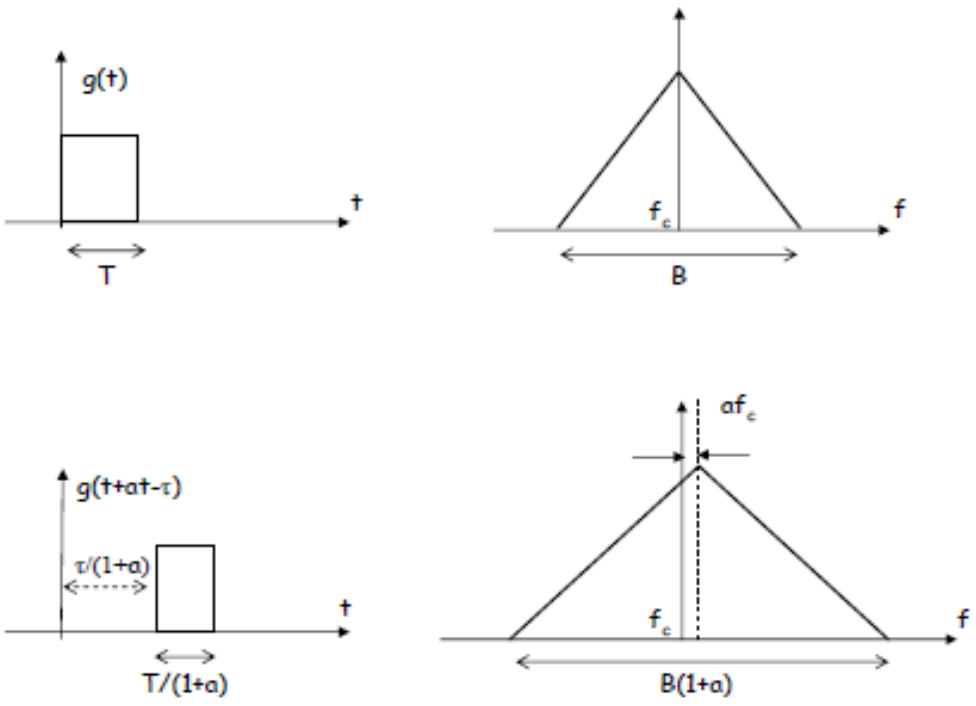

Figure 2.1: Motion causes changes in the signal duration and frequency.

The way in which these distortions affect signal detection depends on the actual value of the factor a. For comparison, let us look at a highly mobile radio system. At 160 km/h (100 miles/h), we have that $a = 1.5 \times 10^{-7}$. This value is low enough that Doppler

spreading can be neglected. In other words, there is no need to account for it explicitly in symbol synchronization. The error made in doing so is only $1/1000$ of a bit per 10,000 bits. Hence, a simplified model can be adopted using an approximation $g(t+at) \approx g(t)$. In contrast to this situation, a stationary acoustic system may experience unintentional motion at 0.5 m/s (1 knot), which would account for $a = 3 \times 10^{-4}$. For an AUV moving at several m/s (submarines can move at greater velocities), the factor a will be on the order of 10^{-3}, a value that cannot be ignored. In such a case, the approximation $g(t + at) \approx g(t)$ cannot be justified.

To highlight the challenges of multi-carrier communication over underwater acoustic channels relative to those faced by wireless radio channels, let us consider three example systems. One is the multi-carrier experiment of the present study, another is the multi-carrier system of the IEEE 802.11a/g standard for wireless local area networks (R. D. J. van Nee and Halford, 1999), and the last is the OFDM based ultra-wideband (UWB) system (A. Batra and Dabak, 2004). Table 2.1 provides the key parameters for these three systems.

Table 2.1: Comparison of OFDM Parameters in Underwater Acoustic, Radio and UWB Channels

	Experiments for this paper	Wireless LAN	UWB OFDM
Propagation speed, c	1500 m/s	3×10^8 m/s	3×10^8 m/s
Bandwidth, B	6 kHz	20 MHz	528 MHz
Carrier Freq f_c	8 kHz	5.2 GHz	3 – 10 GHz Freq Hopping
Narrowband or Wideband?	$B/f_c = 0.75$ Wideband	$B/f_c=0.0038 << 1$ Narrowband	B > 500MHz Wideband
Time scale factor (a = v/c)	$a=1.3 \times 10^{-3}$ for v = 2m/s	$a = 7\times 10^{-8}$ for v = 20m/s	$a = 7\times 10^{-9}$ for v = 2 m/s
Typical multipath spread	10-300 ms	~ 500 ns	~ 100 ns
Typical coherence time	~ 1 s	~ 5 ms	~ 2 ms
one OFDM symbol duration	48 – 352ms	4μs	0.3μs

The following facts should be noted.

- **Underwater Acoustic Channels should be treated as (Ultra) Wideband even with low absolute BW.**

  A common definition of an (ultra) wideband radio is that the system bandwidth is more than 500 MHz or greater than a 25% fraction of the carrier frequency. Although the underwater acoustic channel has limited bandwidth, the signalling must be treated as (ultra) wideband. Receiver design for wideband signals is considerably more complicated than that for narrowband signals. Note that text-book treatments usually focus on radio channels and simplifies the design directly based on the narrowband assumption. That analysis should be re-examined for underwater acoustic communications. Respecting the wideband nature of the system is particularly important in multichannel (array) processing and synchronization for mobile acoustic systems.

- **Need to consider waveform compression/dilation.**

  Relative motion between a source and a receiver results in a Doppler-scaled communication signal, whose distortion is proportional to the ratio of the platform speed to the propagation speed. Due to the slow sound propagation which is 2×10^5 times slower than EM waves in free space, the amount of the time compression or expansion cannot be ignored in underwater acoustic channels. This situation is not commonly found in radio communications. To handle the time-scale change, a re-sampling methodology proved effective in underwater communications (B. Sharif *et al.*, 2000), (T.P. SameerBabu *et al.*, 2007*b*),(T.P. SameerBabu *et al.*, 2007*a*). The re-sampling module, a key to underwater communications, is not needed in wireless radio systems.

- **Need to consider symbol wise channel variation.**

  In high-rate wireless communications applications, the symbol block period is small relative to the channel coherence time. Consequently, the channel can be viewed as time-invariant within one block. On the other hand, channel time-variation within one data block is not negligible for underwater applications, and thus it should be explicitly dealt with.

  In short, the underwater channel should be treated as ultra wideband, which implies frequency dependent Doppler distortion. In addition, significant channel variation occurs even within one OFDM block. Due to the wideband nature of the system, the variation is also frequency dependent. These effects destroy the orthogonality of OFDM sub-carriers, thus inducing significant ICI. Conventional ICI reduction techniques used in radio channels are based on the narrowband system model, and as such they may not be effective for underwater channels. On the positive side, due to the low absolute bandwidth, one can afford to use advanced decoding algorithms to handle the challenging underwater acoustic channels.

In this work, we adopt zero-padded (ZP) OFDM (Z. Wang and Giannakis, 2000), (B. Muquet *et al.*, 2002) for UWA communications instead of the conventional cyclic prefix (CP) in order to save transmission power during the (long) guard interval.

For an OFDM duration of T and guard interval of T_g.

- Data rate reduction by $\frac{T}{T+T_g}$ for both CP and ZP

- No Tx power for ZP, saving by $\frac{T}{T+T_g}$ relative to CP
- However, the noise from the received tail is added back into the beginning of the symbol, which increases the noise power by $\frac{T+T_g}{T}$ Thus, the difference in SNR is not significant for both the methods.
- CP and ZP are similar to Overlap-Save and Overlap-Add method for efficient DSP Implementation of Filtering/Linear Convolution of a long sequence (incoming sequence) with a finite filter/window as Multiplication in the Frequency Domain using FFT algorithm.

2.1 ZP-OFDM with a conventional receiver

Let T denote the OFDM duration and T_g the guard interval. The total OFDM block duration is $T' = T + T_g$. The frequency spacing is $\Delta f = 1/T$. The k^{th} sub-carrier is at frequency

$$f_k = f_c + k\Delta f,\ k = -K/2, ..., K/2 - 1 \tag{2.4}$$

where f_c is the carrier frequency and K sub-carriers are used so that the bandwidth is $B = K\Delta f$.

Let us consider one ZP-OFDM block. Let $d[k]$ denote the information symbol to be transmitted on the k^{th} sub-carrier. The non-overlapping sets of active sub-carriers S_A and null sub-carriers S_N satisfy $S_A \cup S_N = \{K/2, ..., K/2-1\}$. The transmitted signal in passband is then given by

$$s(t) = \Re\left\{\left[\sum_{k\in S_A} d[k]e^{j2\pi k\Delta f t}g(t)\right]e^{j2\pi f_c t}\right\},\ t \in [0, T+T_g] \tag{2.5}$$

where we define $g(t)$ as

$$g(t) = \begin{cases} 1 & \text{if } t \in [0, T] \\ 0 & \text{if } t \in [T, T+T_g] \end{cases} \tag{2.6}$$

to describe the zero-padding operation.

We consider a multipath underwater channel that has the impulse response

$$c(\tau, t) = \sum_p A_p(t)\delta(\tau - \tau_p(t)) \tag{2.7}$$

where $A_p(t)$ is the path amplitude and $\tau_p(t)$ is the time-varying path delay. We assume that all paths have similar Doppler rate

$$\tau_p(t) \approx \tau_p - at \tag{2.8}$$

and that the path gains A_p and the Doppler rate a are constant over the block duration T'. The received signal in passband is then

$$\tilde{y}(t) = \Re\left\{\sum_p A_p \left[\sum_{k\in S_A} d[k]e^{j2\pi k\Delta f(t+at-\tau_p)}g(t+at-\tau_p)\right] e^{j2\pi f_c(t+at-\tau_p)}\right\} + \tilde{n}(t) \tag{2.9}$$

where $\tilde{n}(t)$ is the additive noise. The baseband band version $y(t)$ of received signal satisfies $\tilde{y}(t) = \Re\left\{y(t)e^{j2\pi f_c t}\right\}$, and can be written as

$$\begin{aligned} y(t) &= \sum_p A_p \left[\sum_{k\in S_A} d[k]e^{j2\pi k\Delta f(t+at-\tau_p)}g(t-at+\tau_p)\right] e^{j2\pi f_c(at-\tau_p)} + n(t) \\ &= \sum_{k\in S_A} d[k]e^{j2\pi k\Delta f t}e^{j2\pi a f_k t}\left[\sum_p A_p e^{-j2\pi f_k\tau_p}g(t+at-\tau_p)\right] + n(t) \end{aligned} \tag{2.10}$$

where $n(t)$ is the additive noise in baseband. Based on the expression (2.10), we observe two effects:

- The signal from each path is scaled in duration from T to $T/(1+a)$
- Each sub-carrier experiences a Doppler shift $e^{j2\pi a f_k t}$, which depends on the frequency of the sub-carrier. Since the bandwidth of the OFDM signal is comparable to the center frequency, the Doppler shifts on different OFDM sub-carriers differ considerably as illustrated in Fig. 2.2; i.e., the narrowband assumption does not hold.

Let us consider the performance of a conventional OFDM receiver that does not perform any Doppler compensation. At the output of the demodulator in the m-th sub

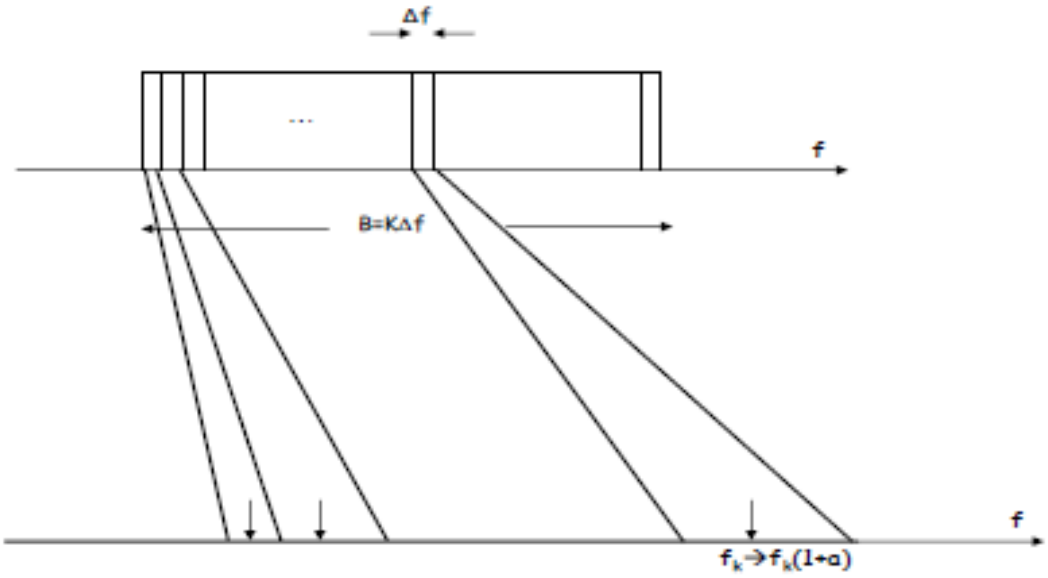

Figure 2.2: Motion-induced Doppler shift is not uniform in a wideband system

channel, we have

$$y_m = \frac{1}{T}\int_0^{T_g+T} y(t)e^{-j2\pi m\Delta f t}dt = \frac{1}{T}\int_0^{T}[y(t)+y(t+T)u(t)]e^{-j2\pi m\Delta f t}dt \qquad (2.11)$$

where $u(t) = 1 \ \forall \ 0 \leq t \leq T_g$ and $u(t) = 0$ elsewhere. The last step implies that the correlation can be performed by overlap-adding of the received signal, followed by FFT processing. Substituting (2.75) into (2.11) and assuming that T_g is greater than the channel delay spread, we obtain

$$\begin{aligned} y_m &= \sum_{k\in S_A} d[k] \sum_p A_p e^{-j2\pi f_k \tau_p} \quad \frac{1}{T}\int_{\tau_p/1+a}^{(T+\tau_p)/(1+a)} e^{j2\pi[(k-m)\Delta f + a f_k]t}dt + n_m \\ &= C\left(\frac{f_m}{1+a}\right)\sum_{k\in S_A} d[k]\rho_{m,k} + n_m \end{aligned} \qquad (2.12)$$

where

$$C(f) = \sum_p A_p e^{-j2\pi f \tau_p}, \quad \alpha_{m,k} = \frac{(m-k) + a f_k/\Delta f}{1+a}, \quad \rho_{m,k} = \frac{1}{1+a} e^{j\alpha_{m,k}} sinc(\alpha_{m,k}) \tag{2.13}$$

The desired signal in y_m is $C\left(\frac{f_m}{1+a}\right)\rho_{m,m}d[m]$, and the rest is ICI plus noise. The signal to interference-plus-noise ratio is

$$\gamma_k = \frac{|\rho_{m,m}|^2 \sigma_d^2}{\sigma_v^2/|C(f_m/(1+a))|^2 + \sum_{k\neq m} |\rho_{m,k}|^2 \sigma_d^2} \tag{2.14}$$

where σ_v^2 is the noise variance and $\sigma_d^2 = E\left[|d[m]|^2\right]$. Note that γ_m has a floor which does not depend on the channel frequency response when σ_v^2 goes to zero. Regarding the Doppler scale a, we observe that there are two special cases. **Case 1: Time-invariant channel**

Consider the special case where $\tau_p(t)$ is time-invariant, i.e., $a = 0$ in (2.8). Disregarding the noise, the received baseband signal is

$$y_0(t) = \sum_{k\in S_A} d[k] e^{j2\pi k\Delta f t} \left[\sum_p A_p e^{-j2\pi f_k \tau_p} g(t-\tau_p)\right] \tag{2.15}$$

which does not suffer from any Doppler distortion. As a result, $\rho_{m,m} = 1$ and $\rho_{m,k} = 0, \forall\, m \neq k$. The correlator output in (9) is then ICI-free:

$$y_m = C(f_m)d[m] + n_m \tag{2.16}$$

In this case, channel equalization in the frequency domain amounts to simple scalar inversion on each sub-carrier. This is the advantage of OFDM over highly-dispersive multipath channels.

Case 2: Narrowband system

If the Doppler scaling is negligible, i.e., $a \to 0$, one could adopt the narrowband

assumption as $af_k \approx af_c$ Disregarding noise,(2.15) reduces to

$$\begin{aligned} y(t) &\approx e^{j2\pi f_c t} \sum_{k \in S_A} d[k] e^{j2\pi k \Delta f t} \left[\sum_p A_p e^{-j2\pi f_k \tau_p d(t+at-\tau_p)} \right] \\ &\approx e^{j2\pi a f_c t} y_0(t) \end{aligned} \tag{2.17}$$

where $y_0(t)$ is the signal corresponding to a time-invariant, purely frequency-selective channel

Since a is extremely small in radio channels, the narrowband model in (2.17) is widely adopted. In radio applications, a carrier frequency offset (CFO) between the transmitter and the receiver leads to an expression of the received signal in the form (2.17). For this reason, we call the term af_c in (2.17) CFO when a narrowband model is concerned. The re-sampling module $-$ key to underwater communications $-$ is not needed in wireless radio systems.

2.2 Mitigating Doppler Effect in Fast time varying Channels

For a single frequency component, at say f_n, the Doppler effect can be modelled as a scaling of frequency

$$\tilde{f_n} = f_n(1+a) \tag{2.18}$$

In wideband signals, the Doppler effect is more accurately modelled as a time scaling (expansion or contraction) of the signal waveform. Hence each frequency component is shifted by an amount which is significantly different from that at other frequencies.

$$r(t) = s\left((1+a)t\right) \tag{2.19a}$$

$$r(nT_s) = s\left((1+a)nT_s\right) \tag{2.19b}$$

If the relative Doppler shift is known, the Doppler effect can be negated by inverse time scaling the received signal. In a multi rate DSP system this is equivalent to re-sampling the received signal by the factor $(1+a)$.Re-sampling can be done either in

passband or in baseband. For convenience, let us present these steps using passband signals.

$$s\left(nT_s\right) = r\left(\left(\frac{n}{1+a}\right)T_s\right) \tag{2.20}$$

Hence, correcting the received signal for Doppler involves scaling the sampling frequency $(\tilde{f}_s) = (1+a)f_s$

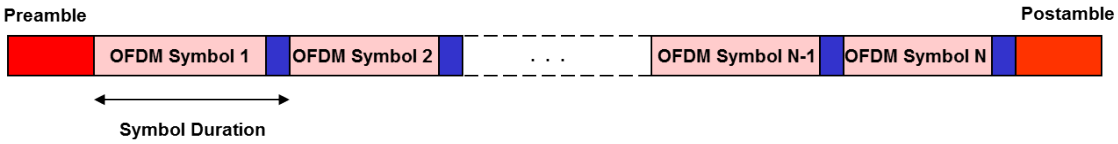

Figure 2.3: Packet Structure

This Frame Structure can also be used for Symbol Synchronization and Sampling Skew Correction

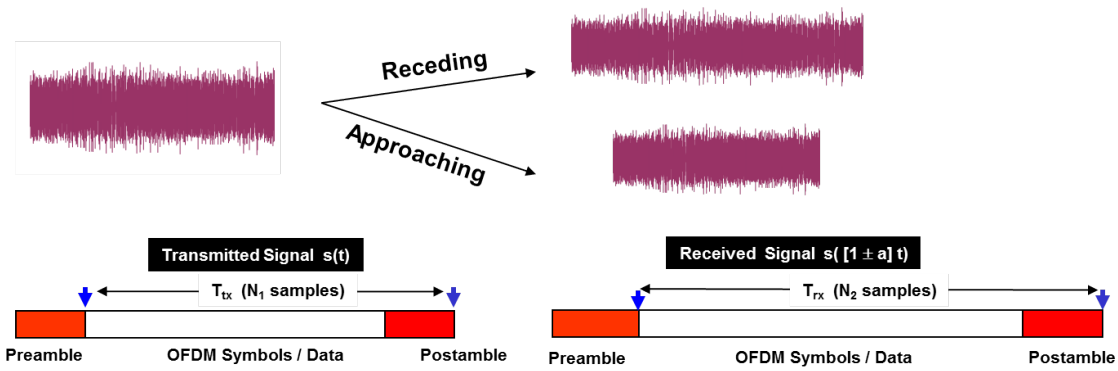

Figure 2.4: Transmitted and Received Packet under Doppler

The relative Doppler scale can be estimated using the pre-amble and post-amble appended to each data packet.

$$\hat{T}_{rx} = (1+\hat{a})T_{tx} \quad \Longrightarrow \quad \hat{a} = \frac{T_{rx}}{T_{tx}} - 1 \tag{2.21}$$

The receiver then re-samples the packet with the re-sampling factor $1+\hat{a}$

$$Resampling\ Factor = 1+\hat{a} = \frac{\hat{T}_{rx}}{T_{tx}} = \frac{N_2}{N_1} \tag{2.22}$$

Again as mentioned earlier, re-sampling can be done either in passband or in baseband. For convenience, let us present these steps using passband signals. From (2.9), we

Figure 2.5: Sensitivity to error in estimated re-sampling factor on decoded test image

re-sample the received waveform $\tilde{y}(t)$ using a re-sampling factor b :

$$\tilde{z}(t) = \tilde{y}\left(\frac{t}{1+b}\right) \tag{2.23}$$

Re-sampling has two effects: (1) it rescales the waveform, and (2) it introduces a frequency-dependent Doppler compensation. With $\tilde{y}(t)$ from (2.9) and $\tilde{z}(t) = \Re\left\{z(t)e^{j2\pi f_c t}\right\}$, the baseband signal $z(t)$ is

$$z(t) = e^{j2\pi\frac{a-b}{1+b}f_c t}\sum_{k\in S_A} d[k]e^{j2\pi k\Delta f\frac{1+a}{1+b}t}\left[\sum_p A_p e^{-j2\pi f_k\tau_p} g\left(\frac{1+a}{1+b}t-\tau_p\right)\right] \tag{2.24}$$

As $\frac{1+a}{1+b} \longrightarrow 1$

$$z(t) \approx e^{j2\pi\frac{a-b}{1+b}f_c t}\sum_{k\in S_A} d[k]e^{j2\pi k\Delta f t}\left[\sum_p A_p e^{-j2\pi f_k\tau_p} g\left(t-\tau_p\right)\right] \tag{2.25a}$$

$$= \underbrace{e^{-j2\pi\epsilon t}}_{\text{Common CFO}} \underbrace{\sum_{k\in S_A} d[k]e^{j2\pi k\Delta f t}\left[\sum_p A_p e^{-j2\pi f_k\tau_p} g\left(t-\tau_p\right)\right]}_{\text{ICI-free Freq-Sel Channel}} \tag{2.25b}$$

where $\epsilon = \frac{a-b}{1+b}f_c$. In (2.25b), the first factor represents *common CFO* and second factor represents *ICI-free Freq-Selective channel*. Common CFO is normally dealt with CFO

compensation Techniques and ICI-free Frequency selective channel is normally dealt with Channel Estimation and Compensation. Now the residual Doppler effect can be viewed as the same for all sub-carriers. Hence, a wideband OFDM system is converted into a narrowband OFDM system with a common CFO

2.3 Waveform Analysis and Design based on Ambiguity Diagram

2.3.1 Wideband Ambiguity Function

Let the transmitted pulse be $s(t)$. We can write the expression for the delayed and Doppler scaled pulse as $s(at-\tau)$, where a is the time scaling factor which is a function of the target velocity. Note that in this discussion, we are not assuming any attenuation in the signal due to the medium properties. The problem is now to estimate the Doppler parameter a and the delay (range) τ. The maximum likelihood estimator of these parameters is the maximum of the cross correlation function between the transmitted pulse and the scaled and time shifted replicas of the same. i.e,

$$\arg\max_{a,\tau} \left| \int_{-\infty}^{\infty} s(t)s(at-\tau) \right| \tag{2.26}$$

We can define[1] the wideband ambiguity function as

$$WA_{f,g}(a',\tau) = \int_{-\infty}^{\infty} f(t)g\left(a'(t-\tau)\right) \tag{2.27}$$

The relation between the wideband and narrow band ambiguity function can be derived as follows. Let $s(t)$ and $S(f)$ be Fourier transform pairs. Then

$$\begin{aligned} s(a'(t-\tau)) &= \int_{-\infty}^{\infty} S(f)\, e^{j2\pi f a'(t-\tau)} df \\ &= \int_{-\infty}^{\infty} e^{-j2\pi f a'\tau}\, S(f) e^{j2\pi f a' t} df \end{aligned} \tag{2.28}$$

[1]Note the change from $at-\tau$ to $a'(t-\tau)$ (Weiss, 1994). These forms are mathematically equivalent, as shown by (Chaiyasena *et al.*, 1992). The second form is easier for Fourier Transform analysis.

Let f_0 be the center frequency of the spectrum $S(f)$. Denote $\Delta f = f - f_0$, the frequency deviation, $\delta = 2v/(c_s + v)$, the relative velocity and $a' = 1 - (2v/(c_s + v))$, the Doppler factor. It is possible write (2.27) as

$$s(a'(t-\tau)) = e^{-j2\pi f_0 \delta(t-\tau)} \int_{-\infty}^{\infty} S(f) e^{j2\pi f(t-\tau)} e^{-i2\pi \Delta f \delta(t-\tau)} df \tag{2.29}$$

There are two factors that affect the signal behaviour. They are $e^{-j2\pi f_0 \delta(t-\tau)}$ and $e^{-i2\pi \Delta f \delta(t-\tau)}$. The first term shifts the signal spectra and the second term stretches/compresses the signal envelope. If the target velocity $v \ll c_s$, then $\delta \ll 1$ and thus it is possible to approximate the term as $e^{-i2\pi \Delta f \delta(t-\tau)} \approx 1$. In this case, we can write

$$s(a'(t-\tau)) = e^{j2\pi f_d (t-\tau)} s(t-\tau) \tag{2.30}$$

where $f_d = -f_0 \delta = f_0(a' - 1)$ is the classical Doppler shift. Incorporating the above results, we can write the expression for the wideband ambiguity function as

$$\begin{aligned} WA_{h,g}(a', \tau) &= \int_{-\infty}^{\infty} h(t) e^{-j2\pi f_0 (a'-1)(t-\tau)} g(t-\tau) dt \\ &= e^{j2\pi f_0 (a'-1)\tau} \int_{-\infty}^{\infty} h(t) g(t-\tau) e^{-j2\pi f_0 (a'-1)t} dt \\ &= e^{j2\pi f_0 (a'-1)\tau} NA_{h,g}(a', \tau) \end{aligned} \tag{2.31}$$

where

$$\begin{aligned} NA_{h,g}(a', \tau) &= \int_{-\infty}^{\infty} h(t) g(t-\tau) e^{-j2\pi f_0 (a'-1)t} dt \\ &= \int_{-\infty}^{\infty} h(t) g(t-\tau) e^{-j2\pi f_d t} dt \end{aligned} \tag{2.32}$$

is the narrowband ambiguity function.

The approximation error between the wideband and the narrowband ambiguity function is given by (L. Auslander and Gertner, 1992) as

$$WA_{h,g}(a', \tau) - NA_{h,g}(a', \tau) = NA_{h,g}(a', \tau) \left\{ e^{j2\pi f_0 (a'-1)\tau} \right\} \tag{2.33}$$

An upper bound on the relative approximation error in terms of signal duration T

and bandwidth B is given by (L. Auslander and Gertner, 1992)

$$|WA_{h,g}(a',\tau)| - \sqrt{a'}|NA_{h,g}(a',\tau)| \leq \frac{\sqrt{a'}}{2\pi}|\delta|TB \tag{2.34}$$

The factors affecting the narrowband approximation are δ, the target velocity, Δf, the signal frequency deviation and $(t-\tau)$, the observation interval.

2.3.2 Narrowband Ambiguity Function

For a pulse $u(t)$ when using the matched filter (which maximises SNR) (2.32) can be re-written as

$$\chi(\tau,\nu) = \int_{-\infty}^{\infty} u(t)u^*(t-\tau)exp(j2\pi\nu t)dt \tag{2.35}$$

where τ and ν are delay and Doppler shift respectively

The narrowband AF as defined in (2.35) is sufficient to explain our purpose, hence ambiguity function (AF) refers to narrowband AF here after in this document.

The ambiguity function (AF) has an important practical meaning-it describes the output of a matched filter when the input signal is delayed by τ and Doppler shifted by ν relative to nominal values for which the matched filter was designed. The AF was introduced by (Woodward, 1953) and is the main tool in several important radar text-books (Cook and Bernfeld, 1967),(Rihaczek, 1969) . Unfortunately, those references differ as to exactly what the signs of τ and ν imply regarding longer or shorter delay, and closing or opening velocities(in the context of radar/sonar). There are also differences with regard to the function as is, or its magnitude or its square or its magnitude squared. An attempt to standardize the definition (Sinsky and Wang, 1974) proposes the format.

$$|\chi(\tau,\nu)|^2 = \left|\int_{-\infty}^{\infty} u(t)u^*(t+\tau)exp(j2\pi\nu t)dt\right|^2 \tag{2.36}$$

where a target farther from the radar/sonar than the reference ($\tau = 0$) position will correspond to positive τ and a positive ν implies a target moving toward the radar/sonar. Representation of the AF of various signals is more often done through graphic plots than through analytic expressions. In the plots there is an emphasis on side-lobes relative to the main-lobe. Using the magnitude square will suppress the side-lobes in the

graphs, while using logarithmic scale may boost the side-lobe appearance too much. We have therefore elected to use and plot $|\chi(\tau,\nu)|$ rather than $|\chi(\tau,\nu)|^2$. So in this report the term ambiguity function will usually refer to

$$|\chi(\tau,\nu)| = \left| \int_{-\infty}^{\infty} u(t)u^*(t+\tau)exp(j2\pi\nu t)dt \right| \tag{2.37}$$

2.3.3 Constant Frequency Pulse

The complex envelope of a constant-frequency (or unmodulated) pulse appears in Fig. 2.6 and is given by

$$u(t) = \frac{1}{\sqrt{T}} rect\left(\frac{t}{T}\right) \tag{2.38}$$

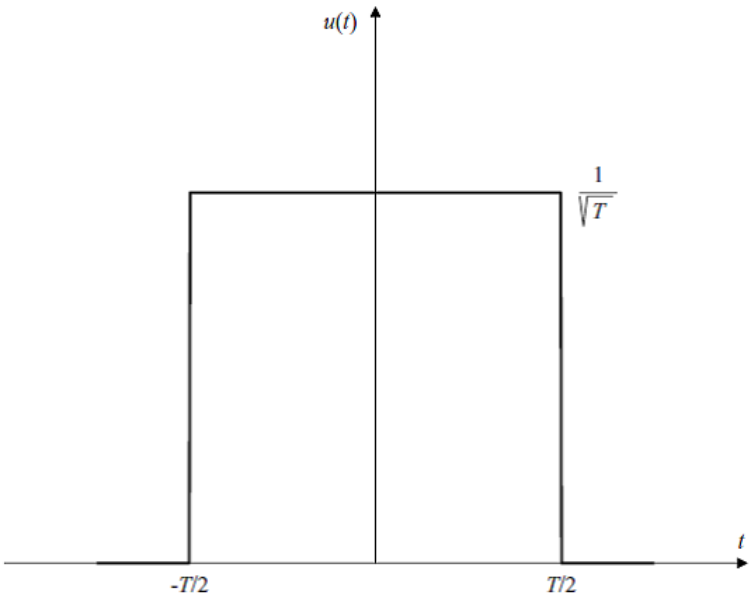

Figure 2.6: Complex envelope of a constant-frequency pulse

The ambiguity function is obtained by using (2.38) in (2.37)

$$\chi(\tau,\nu) = \begin{cases} \frac{1}{T}\int_{-(T/2)+\tau}^{T/2} exp(j2\pi\nu t)dt, & 0 \le \tau \le T \\ \frac{1}{T}\int_{-(T/2)}^{(T/2)+\tau} exp(j2\pi\nu t)dt, & -T \le \tau < 0 \\ 0, & elsewhere \end{cases} \tag{2.39}$$

Solving the integrals and taking absolute value yields

$$|\chi(\tau,\nu)| = \begin{cases} \left|\left(1-\frac{|\tau|}{T}\right)\frac{sin[\pi T\nu(1-|\tau|/T)]}{\pi T\nu(1-|\tau|/T)}\right|, & |\tau| \le T \\ 0, & elsewhere \end{cases} \tag{2.40}$$

The cut along the delay axis is obtained by setting $v = 0$, yielding

$$|\chi(\tau,0)| = \begin{cases} 1-\frac{|\tau|}{T}, & |\tau| \le T \\ 0, & elsewhere \end{cases} \tag{2.41}$$

The cut along the Doppler axis is obtained by setting $\tau = 0$, yielding

$$|\chi(0,\nu)| = \left|\frac{sin\pi T\nu}{\pi T\nu}\right|, \quad -\infty < \nu < \infty \tag{2.42}$$

The first two quadrants of the ambiguity function are plotted in Fig. 2.7. A contour plot of the AF, covering all four quadrants, appears in Fig. 2.8. Two contour levels are plotted; the solid line represents $|\chi(\tau,\nu)| = 0.707$ and the dotted contours represent $|\chi(\tau,\nu)| = 0.1$. Fig. 2.7 clearly shows the triangular zero-Doppler cut of the ambiguity function, described in (2.41). The delay response reaches zero at the pulse width T. The zero-delay cut is less obvious from Fig. 2.7 and is plotted separately in Fig. 2.9. The first Doppler null is at the inverse of the pulse duration: namely, $|\chi(0,1/T)| = 0$. We can therefore approximately state that the delay resolution is T and the Doppler resolution is $1/T$.

2.3.4 Linear FM effect

If a given complex envelope $u(t)$ has an ambiguity function $|\chi(\tau,\nu)|$: namely,

$$u(t) \iff |\chi(\tau,\nu)| \tag{2.43}$$

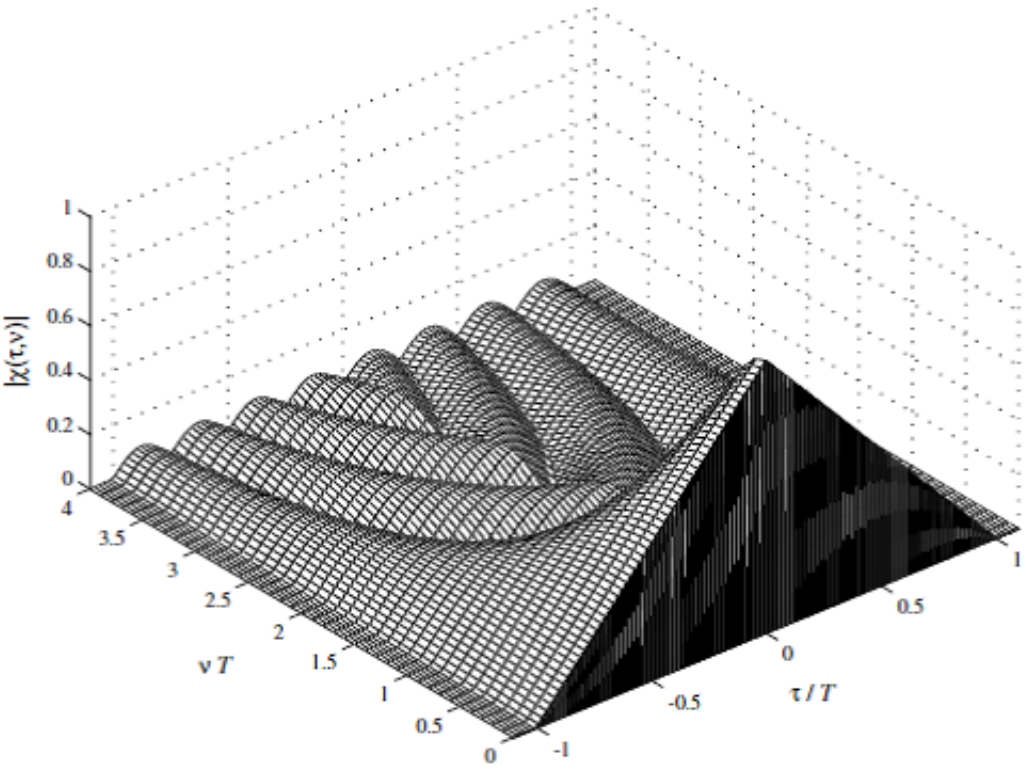

Figure 2.7: Partial ambiguity function of a constant-frequency pulse of length T

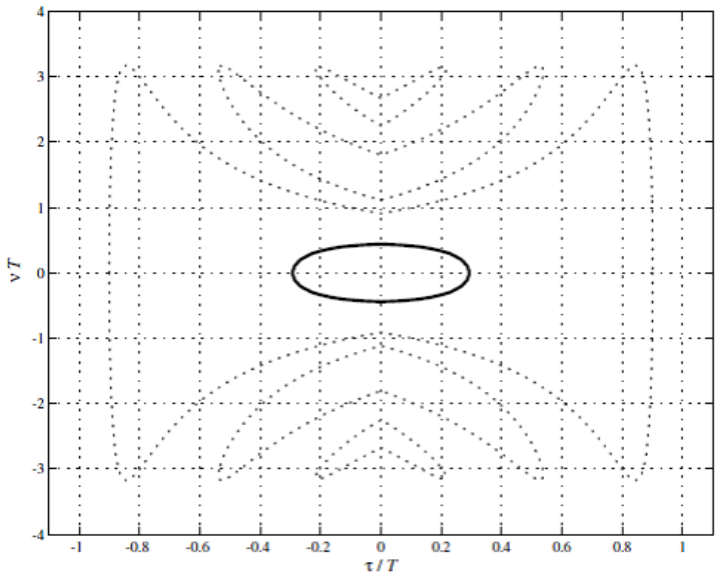

Figure 2.8: Contours 0.1 (dotted) and 0.707 (solid) of the AF of a pulse.

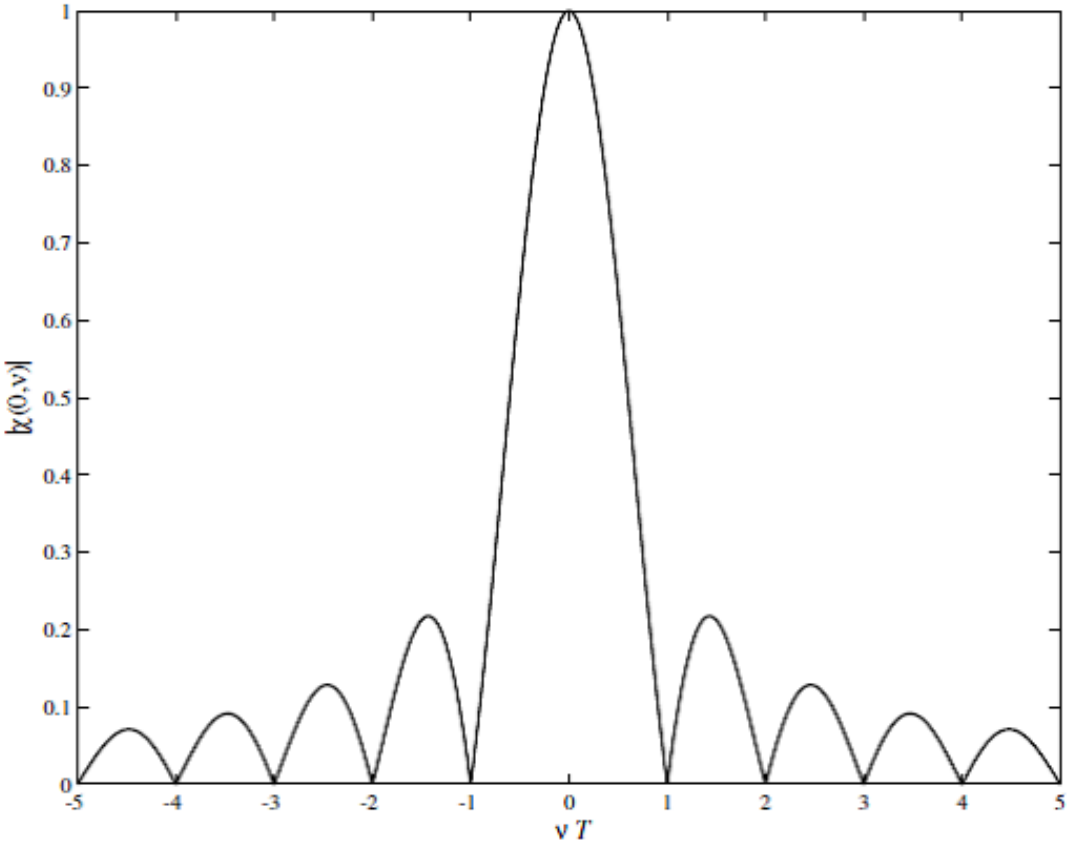

Figure 2.9: Zero-delay cut of the AF of a pulse

then adding linear frequency modulation (LFM), which is equivalent to a quadratic-phase modulation, implies that

$$u(t)exp(j\pi kt^2) \iff |\chi(\tau, \nu - k\tau)| \tag{2.44}$$

This property says that adding LFM modulation shears the resulting ambiguity function. This important property is the basis for an important pulse compression technique.

Interpretation of the property

We explain the shearing caused by the LFM effect with the help of Fig. 2.10. Let the horizontal ellipsoid $|\chi(\tau, \nu)| = c$ be the contour of the original ambiguity function having a specific value c. The contour intersects the negative Doppler axis at point A with the coordinates ($\tau = 0, \nu = v_A$), and it intersects the positive delay axis at point B. Representing the AF for LFM as

$$|\chi_1(\tau, \nu)| = |\chi(\tau, \nu - k\tau)| \tag{2.45}$$

with the coordinates ($\tau = \tau_B, \nu = 0$). The corresponding points A_1 and B_1, of $|\chi_1(\tau, \nu)| = c$, have the same delay coordinates, respectively ($\tau_{A_1} = 0, \tau_{B_1} = \tau_B$). We use (2.45) to find their respective Doppler coordinates, A_1 and ν_{B_1}. Because the delay coordinate of the original intersection of A is zero, we get for A_1

$$c = |\chi_1[0, (\nu - k.0)]| = |\chi_1[0, \nu_A]| \tag{2.46}$$

Implying that the Doppler coordinate of A_1 is identical to the Doppler coordinate of A. Next we ask where the contour $|\chi_1(\tau, \nu)| = c$ meets the delay τ_B; or what is ν_{B_1} so that $|\chi_1(\tau_B, \nu_{B_1})| = c$? Using (2.45), we get

$$|\chi_1(\tau_B, \nu_{B_1})| = |\chi(\tau_B, \nu_{B_1} - k\tau_B)| = c \tag{2.47}$$

However, Fig. 2.10 in we note that $|\chi(\tau_B, 0)| = c$, which implies that $\nu_{B_1} - k\tau_B = 0$,

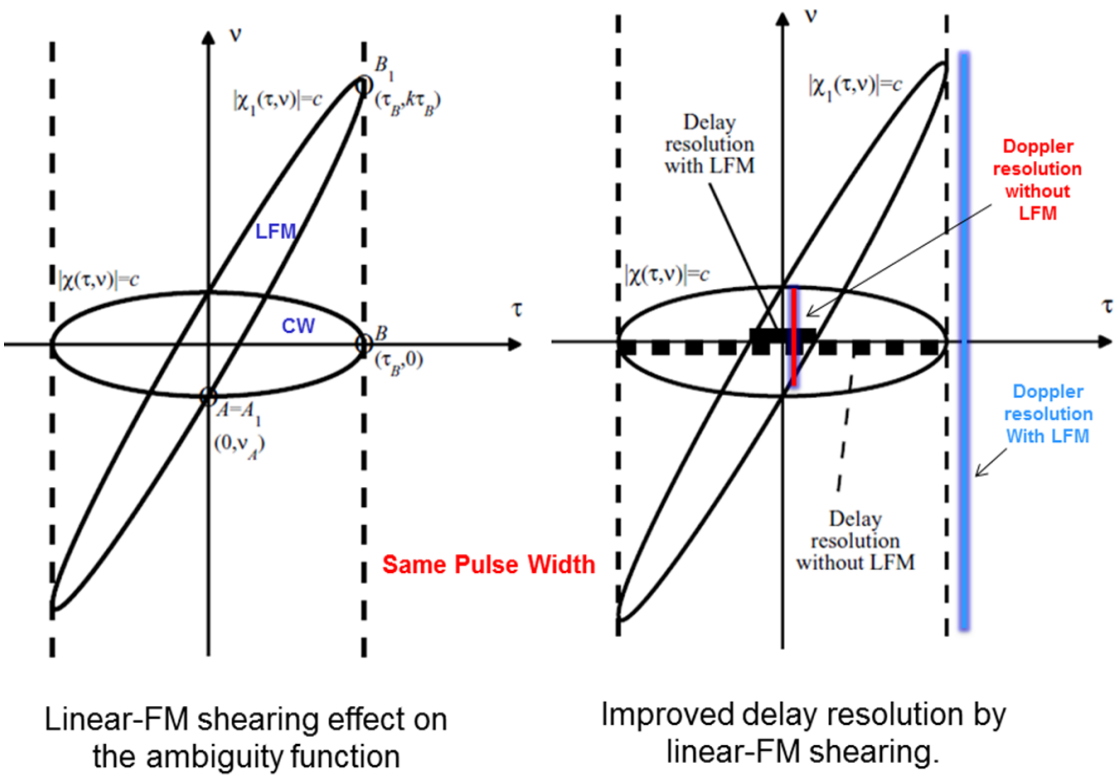

Figure 2.10: Linear FM Shearing Effect

or

$$\nu_{B_1} = k\tau_B \tag{2.48}$$

We thus found that point B at the coordinates $(\tau = \tau_B, \nu = 0)$, whose delay coordinate is the largest delay through which the contour $|\chi(\tau,\nu)| = c$ passes, was moved, by adding LFM, to point B_1 at the coordinates $(\tau = \tau_B, \nu = k\tau_B)$. Other points of the contour $|\chi(\tau,\nu)| = c$, at delays $0 < \tau < \tau_B$, were moved in a similar way, thus resulting in the sheared contour $|\chi_1(\tau,\nu)| = c$, also shown in Fig. 2.10. The shearing property of linear FM, which we just studied, reduces (improves) the delay resolution, as pointed out in Fig. 2.10.

Finally, note that for the definition of the ambiguity function used here, the shape of the LFM ridge passing from the third quadrant to the first quadrant of the delay-Doppler space is typical for positive LFM slope ($k > 0$). This implies that for positive LFM slope signal a positive error in estimating range (the range is assumed to be farther than it really is) will translate to lower closing velocity (negative Doppler).

Cuts through the Ambiguity Function

Some insight into the two-dimensional ambiguity function (AF) can be obtained from its one-dimensional cuts. Consider first the cut along the delay axis. Setting $\nu = 0$ in (2.37) gives

$$|\chi(\tau, 0)| = \left| \int_{-\infty}^{\infty} u(t)u^*(t+\tau)dt \right| = |R(\tau)| \tag{2.49}$$

where $R(\tau)$ is the autocorrelation function (ACF) of $u(t)$. We got that the zero-Doppler cut of the AF, known as the range window for a matched-filter receiver, is the ACF. On the other hand, the ACF equals the inverse Fourier transform of the power spectral density. Thus, we obtain the relationship

$$RangeWindow \Longleftrightarrow Autocorrelation \Longleftrightarrow F^{-1}\{PowerSpectrum\}$$

This relationship reiterates the importance of LFM. Adding linear frequency modulation broadens the power spectrum, hence narrows the range window, as shown in Fig. 2.11.

The second interesting cut is along the Doppler frequency axis. Setting $\tau = 0$ in (2.37)) results in

$$|\chi(0, \nu)| = \left| \int_{-\infty}^{\infty} |u(t)|^2 exp(j2\pi\nu t)dt \right| \tag{2.50}$$

Equation (2.50) indicates that the zero-delay cut is the Fourier transform of the magnitude squared of the complex envelope $u(t)$. In other words, this cut is indifferent to any phase or frequency modulation in $u(t)$; it is a function only of the amplitude.

2.3.5 Linear Frequency-Modulated Pulse

Linear frequency modulation (LFM) is the first and probably still is the most popular pulse compression method. It was conceived during World War II, independently on both sides of the Atlantic, as can be deduced from German, British, and U.S. patents (Cook and Bernfeld, 1967), (Cook and Seibert, 1988). The basic idea is to sweep the

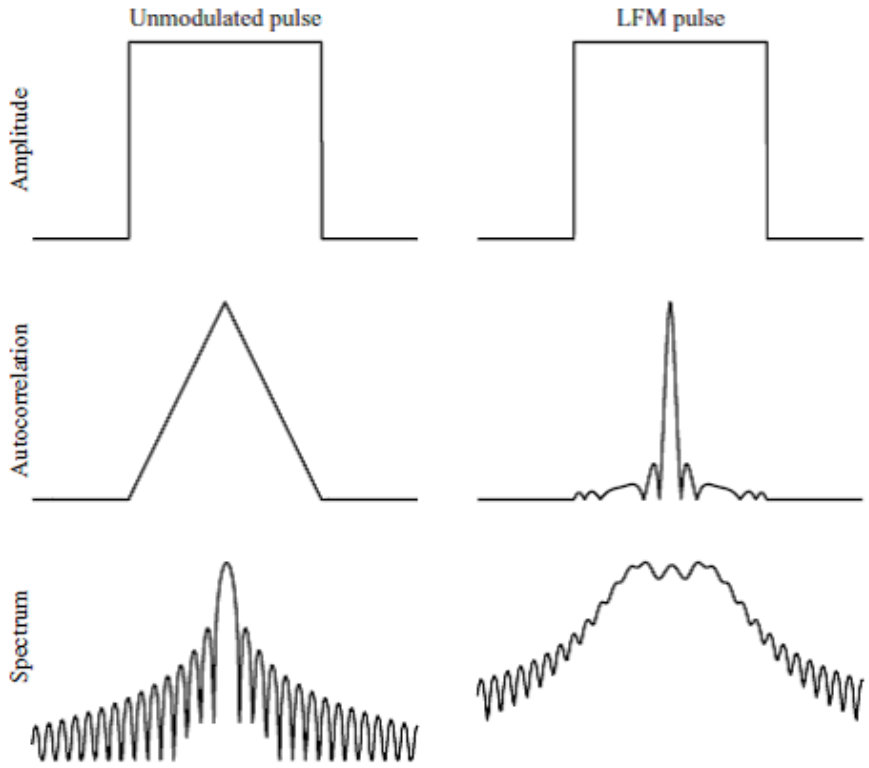

Figure 2.11: Comparison between unmodulated pulse and linear-FM pulse

frequency band B linearly during the pulse duration T Fig. 2.12.

The complex envelope of a linear-FM pulse is given by

$$u(t) = \frac{1}{\sqrt{T}} rect\left(\frac{t}{T}\right) exp(j\pi t^2), \quad k = \pm\frac{B}{T} \tag{2.51}$$

The instantaneous frequency $f(t)$ is obtained by differentiating the argument of the exponential,

$$f(t) = \frac{1}{2\pi}\frac{d(\pi k t^2)}{dt} = kt \tag{2.52}$$

The instantaneous frequency is indeed a linear function of time. The frequency slope k has the dimension s^2.

The ambiguity function (AF) is obtained by applying property to the AF of an unmodulated pulse. Replacing ν in (2.40) with $\nu - k\tau$ yields the AF of a linear-FM (LFM)

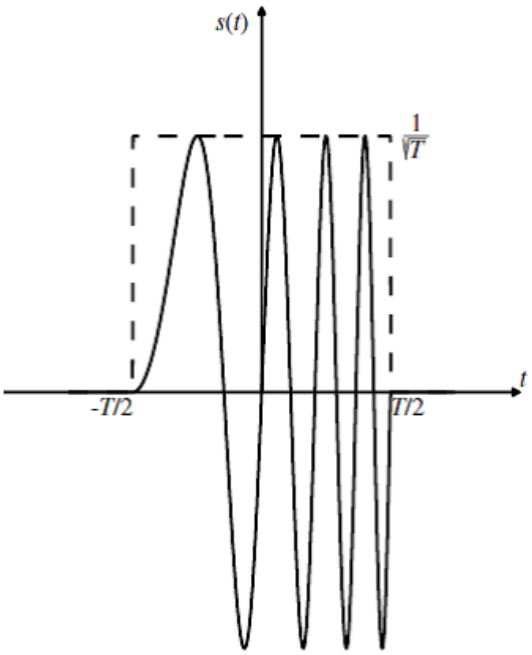

Figure 2.12: Linear-FM signal

pulse:

$$|\chi(\tau,\nu)| = \begin{cases} \left|\left(1-\frac{|\tau|}{T}\right)\frac{sin[\pi T(\nu \mp B(\tau/T))(1-|\tau|/T)]}{\pi T(\nu \mp B(\tau/T))(1-|\tau|/T)}\right|, & |\tau| \leq T \\ 0, & elsewhere \end{cases} \tag{2.53}$$

Fig. 2.13 presents an example of the AF of an LFM pulse calculated using the MATLAB code. The phase and frequency of the complex envelope are shown in Fig. 2.14. The effective time-bandwidth product of the signal is $kT^2 = BT = 10$, where B is the total frequency deviation. Note that the total deviation of the normalized frequency plot is BT, and the total phase deviation is $BT\pi/4$.

The zero-Doppler cut of the AF is obtained by setting $\nu = 0$ in (2.53). Using $kT = B$ yields

$$|\chi(\tau,0)| = \begin{cases} \left|\left(1-\frac{|\tau|}{T}\right)\frac{sin[\pi B\tau(1-|\tau|/T)]}{\pi B\tau(1-|\tau|/T)}\right|, & |\tau| \leq T \\ 0, & elsewhere \end{cases} \tag{2.54}$$

For a large time-bandwidth product ($kT^2 = BT \gg 4$) the first null of $|\chi(\tau,0)|$

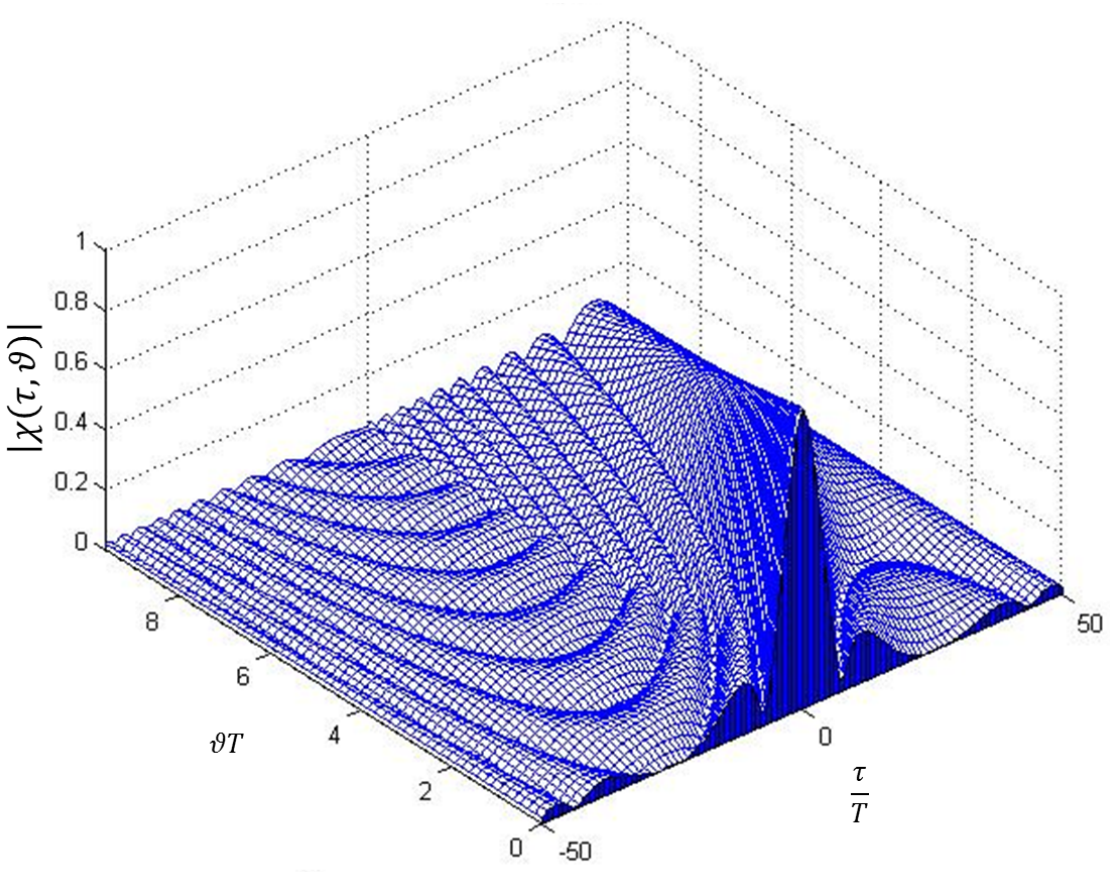

Figure 2.13: Partial ambiguity function of linear-FM pulse (BT =10)

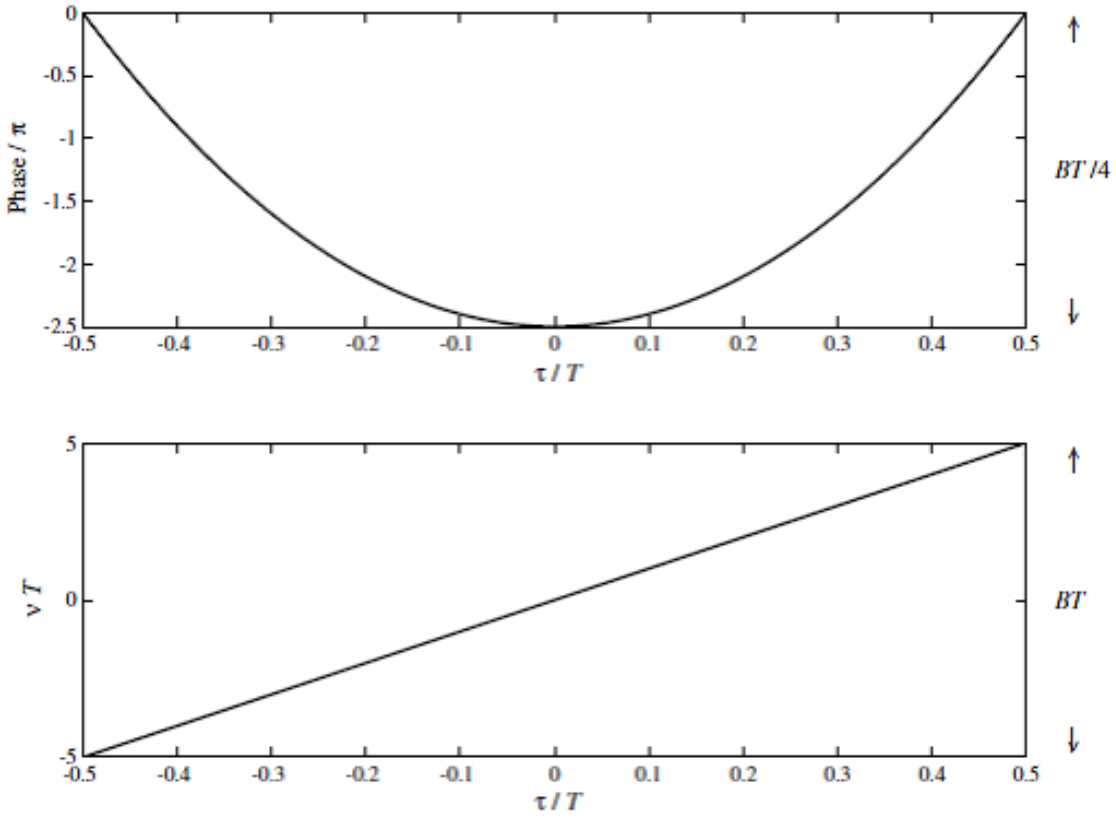

Figure 2.14: Phase and frequency characteristic of the LFM pulse used in Fig. 2.13

occurs at

$$\tau_{1'^{st}\,null} \approx \frac{1}{|k|T} = \frac{1}{B} \tag{2.55}$$

The compression ratio will be defined as $T/\tau_{1'^{st}\,null}BT$, and it is approximately equal to the time-bandwidth product. Returning to Fig. 2.13, since $BT = 10$, the first null should occur at $\tau/T = 0.1$. A plot of $|\chi(\tau, 0)|$ for $BT = 10$ appears in Fig. 2.15.

The issue of spectral efficiency is demonstrated in Fig. 2.16. The horizontal scale is frequency normalized with respect to the pulse width. The vertical scale is the spectral density in decibels. To obtain similar range resolution, the unmodulated pulse width was one-tenth of the LFM pulse width. The absolute horizontal scales are therefore identical in both plots. Comparing the two plots clearly shows more efficient spectrum use in the LFM case. The spectral efficiency of LFM improves as the time-bandwidth product increases, because the spectral density then approaches a rectangular shape. Note that the spectrum plotted in Fig. 2.16 are of the signals' complex envelopes and are

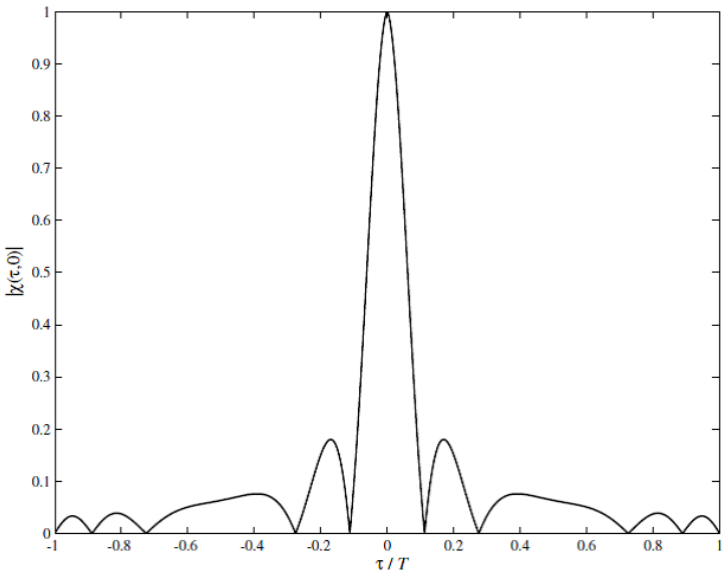

Figure 2.15: Zero-Doppler cut of the AF of LFM pulse with a time-bandwidth product(BT) of 10

therefore centered about zero. Due to symmetry, it suffices to plot positive frequencies only.

The improved delay resolution of LFM does come with a penalty, delay-Doppler coupling. It is expressed by the diagonal ridge seen in the three dimensional plot of the AF (Fig. 2.13). A contour plot (Fig. 2.17) emphasizes the coupling problem. From (2.54) we find that for small Doppler shift ν, the delay location of the peak response is shifted from true delay by

$$\tau_{shift} = \frac{\nu}{k} \tag{2.56}$$

The physical interpretation is that when $k > 0$, a target with positive Doppler appears closer than its true range. In many applications the resulting range error is acceptable. The delay error of the shifted peak response is accompanied by a small decrease in the height of the peak, as evident in Fig. 2.13. It can be shown that near the origin, the peak height decreases according to

$$|\chi(\tau_{peak}, \nu)| = 1 - \left|\frac{\nu}{kT}\right| = 1 - \left|\frac{\nu}{B}\right| \tag{2.57}$$

Since the typical Doppler shift ν is usually much smaller than the signal's frequency

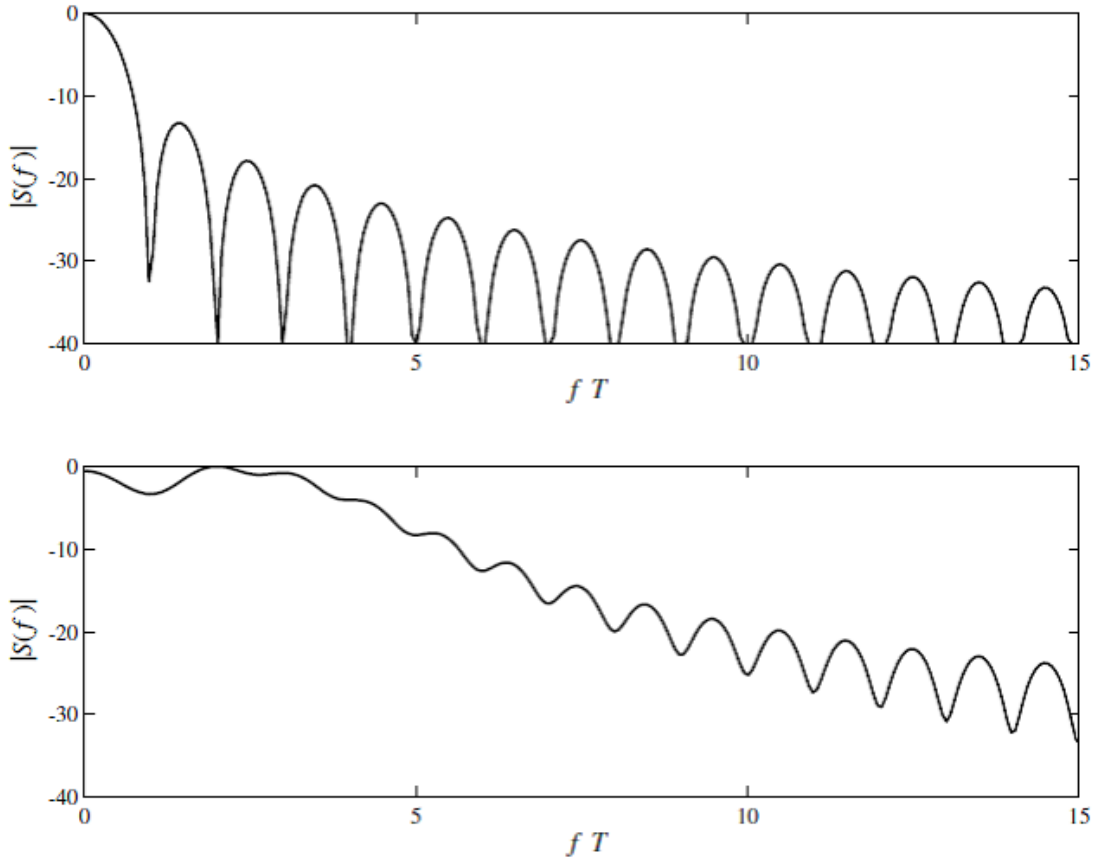

Figure 2.16: Spectral density (in dB) of unmodulated pulse (top) and LFM pulse, $BT = 10$ (bottom)

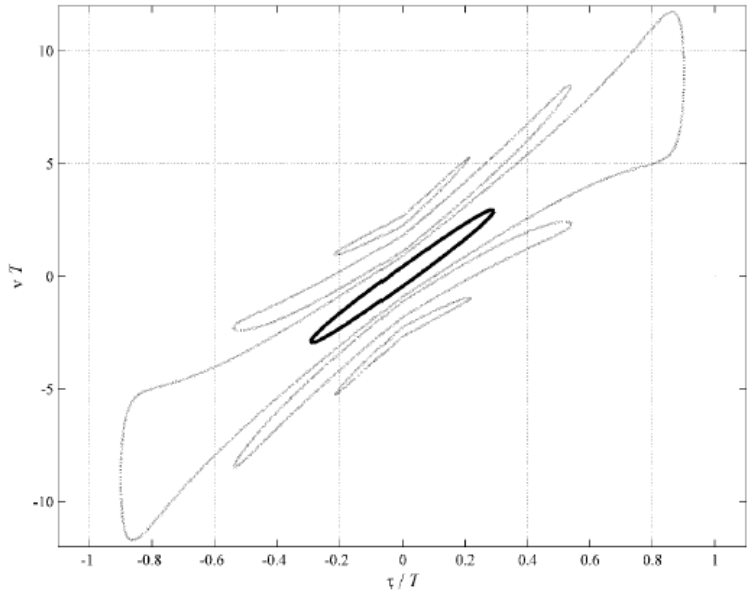

Figure 2.17: Contours 0.1 and 0.707 of the AF of an LFM pulse (BT = 10)

deviation B, the AF peak height decreases very moderately. This behaviour is responsible for the Doppler tolerance property attributed to LFM.

2.4 Desirable Properties of Preamble and Post-amble Waveforms for Packet length based Doppler scale Estimation

The Cramer Rao lower bound for the packet length (in time) estimate is given by (2.58). The detailed derivation of (2.58) is given in the Appendix.

$$var(\hat{T}_{rx}) \geq \frac{2}{\left(\frac{\varepsilon}{N_0/2}\right)} \bar{B^2} \tag{2.58}$$

where $\varepsilon =$ Pulse energy, $B =$ RMS Bandwidth, $var(\hat{T}_{rx}) =$ Estimated received frame length

The Cramer Rao Lower Bound expression for the frame length at the receiver explicitly gives the variance of the estimate as dependant on the SNR and the bandwidth of the signal. The dependence on SNR is very clear since in general, higher the SNR; the more accurate will be the estimate. The factor which is ambiguous is the bandwidth. Does the expression imply that no matter how different the signals be, if their bandwidth is the same, we can always rely on the CRLB value?. The answer is surprisingly negative. It appears that in such parameter estimation problems, more properties of the signal than just the bandwidth plays a major role in deciding the accuracy of estimation. We have compared three candidate signals having the same bandwidth as possible choices for the pulse waveform. They are (1) Linear Frequency Modulated or LFM (Chirp) signals (2) Pseudo random sequence modulated by BPSK (Direct sequence spread spectrum) and (3) Costas signal. Fig. 2.18 compares the power spectrum of the three signals.

The result of estimation of the scaling parameter a by packet length based technique using the three waveforms is illustrated in Fig. 2.19. The SNR used for the simulation is 0 dB.

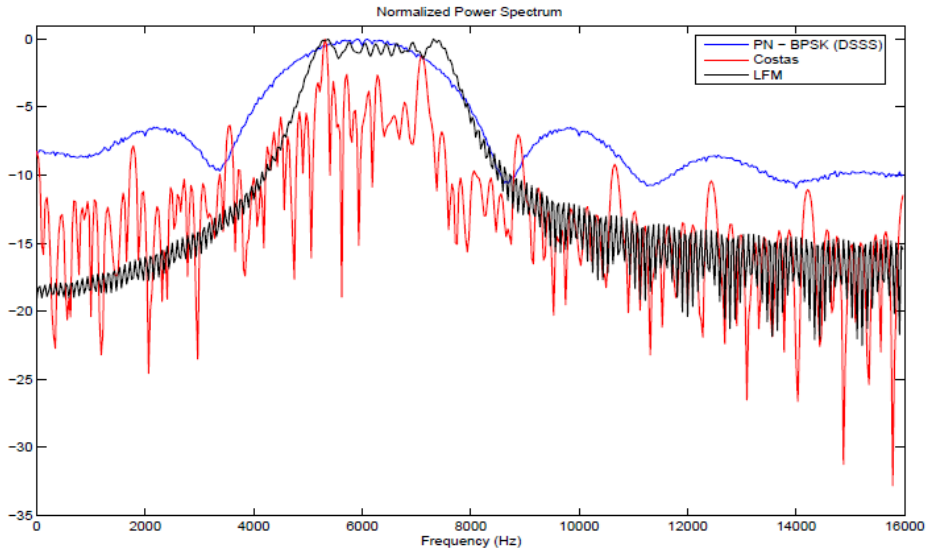

Figure 2.18: Comparison of Power Spectrum

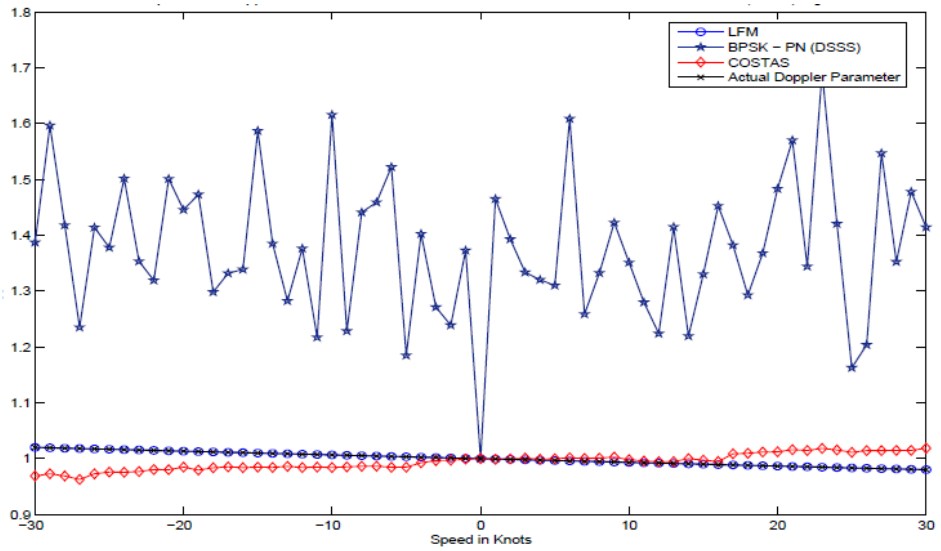

Figure 2.19: Performance comparison of Doppler Parameter Estimation

The results indicate that while the LFM waveform is able to give a correct estimate of the Doppler parameter, the performance of the Costas and the PN-BPSK signals is poor. However, it is interesting to note that all the three signals give a correct estimate at zero knots (stationary case). What is the reason for this discrepancy in performance? The answer to the same can be found by analysing the ambiguity function of these signals. The ambiguity diagrams for the three signals considered in our study are in Fig. 2.20 to Fig. 2.22.

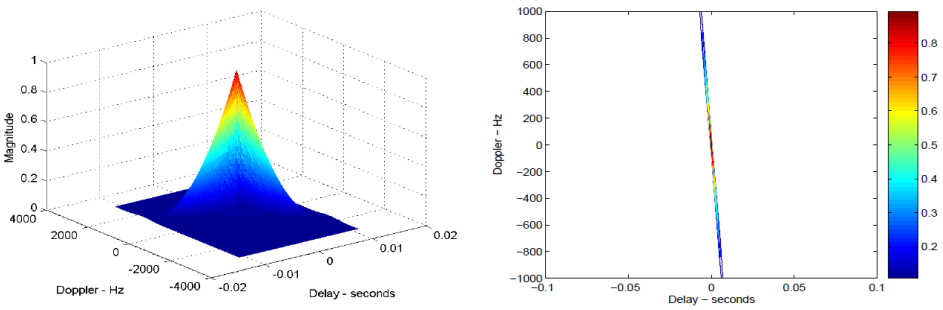

Figure 2.20: Ambiguity Function for LFM Signal

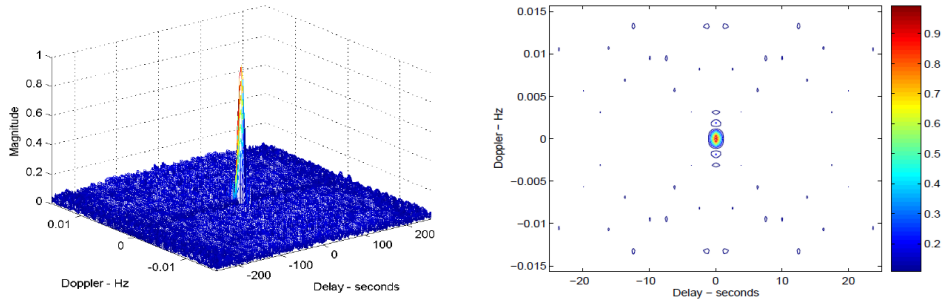

Figure 2.21: Ambiguity Function for PN-BPSK (DSSS) Signal

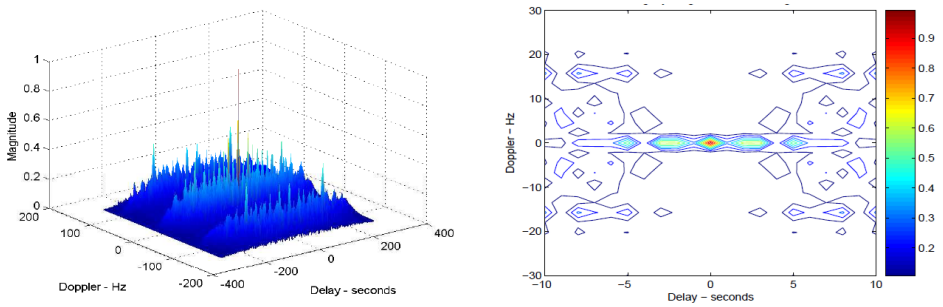

Figure 2.22: Ambiguity Function for Costas Signal

The Doppler parameter estimation by packet length based method measures the difference in the time indices at which the matched filter response becomes maximum during the observation interval. The matched filter is designed based on the transmitted

waveform. For accurate estimation, the matched filter should respond to the received echo (time delayed and Doppler affected) in a similar manner as it would to the original transmitted signal. From the ambiguity diagrams, it is clear that the matched filter for the LFM signal is highly tolerant towards change in the signal due to Doppler spread. The matched filters for PN-BPSK and Costas waveforms do not possess this property. The Table 2.2 compares the delay and Doppler tolerances of the three waveforms. The values given correspond to the points at which the normalized ambiguity function falls to approximately 0.7 times the maximum value.

Table 2.2: Delay and Doppler Tolerance Comparison

Waveform	Bandwidth	Pulse Width	Delay Tolerance	Doppler Tolerance
LFM	3 kHz	10ms	± 1.6 ms	± 250Hz
PN-BPSK(DSSS)	3 kHz	10ms	±0.45s	$\pm 5^{-4}$Hz
Costas	3 kHz	10ms	±0.3s	±0.5 Hz

From the above table, it is evident that in order to estimate the Doppler parameter effectively using the Packet length based method, the pulse signals used should have the following properties.

- **The waveform should have very low delay (range) tolerant**: Required since the estimation method essentially measures scaling in time delay of the received frame.
- **The waveform should be highly Doppler tolerance**: Required since the matched filter designed for the transmitted waveform must be able to effectively detect the Doppler shifted version of the same to identify the time index accurately.

The LFM signal has the unique property, that it can be tuned to have adjustable Delay resolution and Doppler tolerance at the same time. This can be done by decreasing the pulse width (for increasing the range resolution) and by increasing the bandwidth (for increasing the Doppler tolerance) independently. This is manifested as an increased slope in the ambiguity plane. We can safely conclude that the LFM waveform with high slope in the ambiguity plane is an ideal candidate.

Fig. 2.23 illustrates the estimator performance with SNR for the LFM waveforms. The bandwidth of the LFM waveform is 3kHz as earlier. The estimation results for

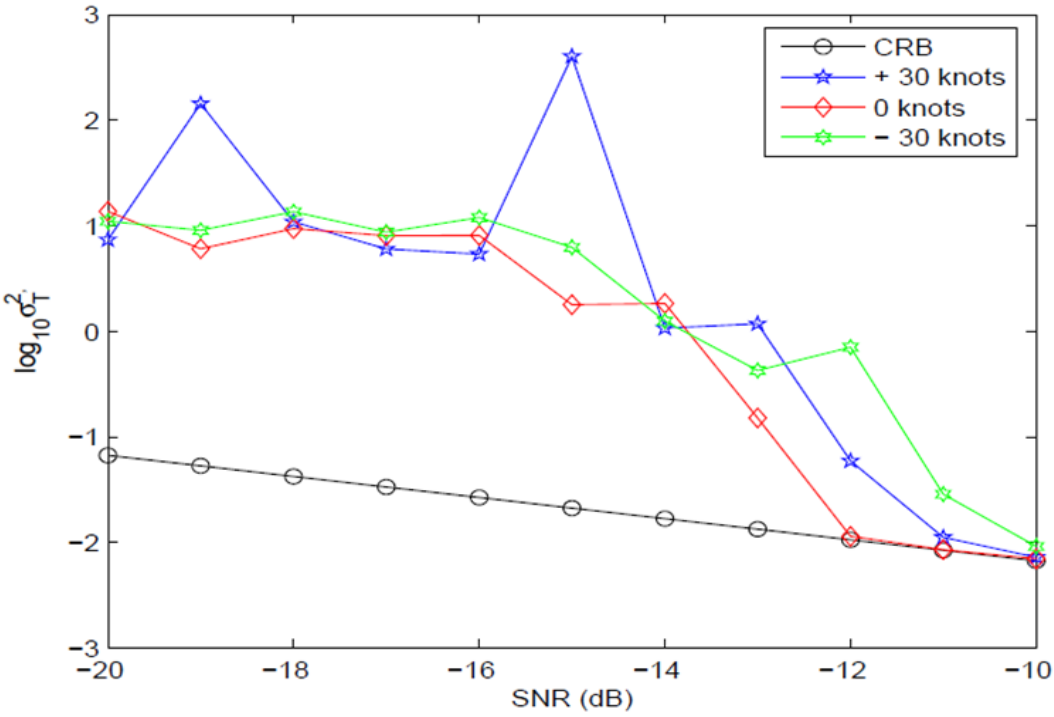

Figure 2.23: Doppler Estimator Performance at Various Speeds for LFM Signal (Bandwidth 3 kHz)

three different target speeds are given. The estimator is seen to approach the CRB performance at an SNR of -10dB for all the different scenarios considered. The estimator is seen to be highly efficient even at low SNR conditions. This result has wide ranging applications in sonar signal processing and underwater wireless communications.

2.5 Velocity Resolution of the Estimator

In the Packet Length estimation, the basic mathematical model is related and developed based on the range (delay) measurement. Hence our study, we are deriving the velocity resolution in terms of the range resolution of the pulse signal which we take as a LFM.

Without loss of generality, let us assume the transmitter is stationary. As the first case, consider the problem of range/delay resolution between two receivers. Let two receivers (both stationary and thus having zero Doppler) be separated in range by ΔR. The fundamental question to be answered is the following : What is the smallest value of ΔR so that the received signal is interpreted as two distinct signals?. Let the transmitted

pulse $s(t)$ be expressed as the real part of the complex signal $\psi(t)$ given as

$$\psi(t) = A(t)e^{j\omega_0 t - \phi(t)} = u(t)e^{j\omega_0 t} = u(t)e^{j2\pi f_0 t} \tag{2.59}$$

where $A(t)$ is the amplitude modulated component, $\phi(t)$ is the phase modulated component and f_0 is the centre frequency. Let $u(t) = A(t)e^{-j\phi(t)}$. The received signal at two the receivers can be written as

$$s_{r1}(t) = \psi(t - \tau_0) \tag{2.60a}$$

$$s_{r2}(t) = \psi(t - \tau_0 - \tau) \tag{2.60b}$$

where τ is the delay between between the two receivers. Without any loss of generality, set $\tau_0 = 0$. The two receivers can be distinguished depending on how small or large the delay τ is. To measure the difference in range between the two targets, consider the integral square error between $\psi(t)$ and $\psi(t - \tau)$ as

$$\begin{aligned}\varepsilon_R^2 &= \int_{-\infty}^{\infty} \{\psi(t) - \psi(t-\tau)\}^2 \, dt \\ &= \int_{-\infty}^{\infty} |\psi(t)|^2 dt - \int_{-\infty}^{\infty} |\psi(t-\tau)|^2 dt - \int_{-\infty}^{\infty} \{\psi(t)\psi^*(t-\tau) + \psi^*(t)\psi(t-\tau)\} \, dt\end{aligned} \tag{2.61}$$

Using (2.59), it is possible to express the above as

$$\varepsilon_R^2 = 2\int_{-\infty}^{\infty} |u(t)|^2 dt - 2\Re\left\{e^{-j\omega_0 t} \int_{-\infty}^{\infty} u^*(t)u(t-\tau)dt\right\} \tag{2.62}$$

The first term represents the signal energy and can be assumed to be a constant. The second term is a function of τ which is called the range ambiguity function defined as

$$\chi_R(\tau) = \int_{-\infty}^{\infty} u^*(t)u(t-\tau)dt \tag{2.63}$$

The maximum of $\chi_R(\tau)$ is at $\tau = 0$. The resolvability in range is measured by the squared magnitude of $|\chi_R()|^2$. If $|\chi_R(\tau)| = \chi_R(0)$ for some value of τ, then the two targets are indistinguishable. The most desired shape of $\chi_R(\tau)$ for a good range

resolution is a sharp peak centred at $\tau = 0$. The time delay resolution is given by

$$\Delta\tau = \frac{\int_{-\infty}^{\infty} |\chi_R(\tau)|^2 d\tau}{|\chi_R(0)|^2} \tag{2.64}$$

Using Parseval's theorem

$$\Delta\tau = 2\pi \frac{\int_{-\infty}^{\infty} |U(\omega)|^4 d\omega}{\left[\int_{-\infty}^{\infty} |U(\omega)|^2 d\omega\right]^2} = \frac{1}{B} \tag{2.65}$$

where B is the bandwidth of the signal. The minimum range resolution corresponding to $\Delta\tau$ is

$$\Delta R = c_s \Delta\tau = c_s/B \tag{2.66}$$

In our simulations, we have used a LFM signal with a bandwidth of 3 kHz. This gives us a range resolution of 0.5m assuming the velocity of sound as 1500m/s. To find the velocity resolution for the Packet length based method, this value is of fundamental importance. The initial Packet length is T_{tx} seconds. In order to distinguish the effect of Doppler, the receiver has to move at least the distance ΔR in the interval equalling to the T_{tx}. This is necessary in order to bring in the effect of differential range measurement as in (C.19). In our study, the T_{tx} is set as 6s. This imply that the target has to move at least 0.5m in the interval T_{tx} to be detected as a moving one. The minimum velocity of the target should be $0.5/6 = 0.082m/s \approx 8cm/s$. The importance of the Packet Length T_{tx} will be evident from now on. The velocity resolution will depend on how much distance that the receiver moves in the packet length duration T_{tx}. Mathematically we can write the expression for the velocity resolution as

$$\Delta v = \frac{\Delta R}{T} = \frac{c_s}{B} . \frac{1}{T_{tx}} \tag{2.67}$$

Note that this resolution is dependent on the signal bandwidth (B) and the packet length (T_{tx}). Thus depending on the requirements, these two parameters can be adapted to give a desired resolution. The fundamental requirement is that the target should maintain a constant velocity during T_{tx}.

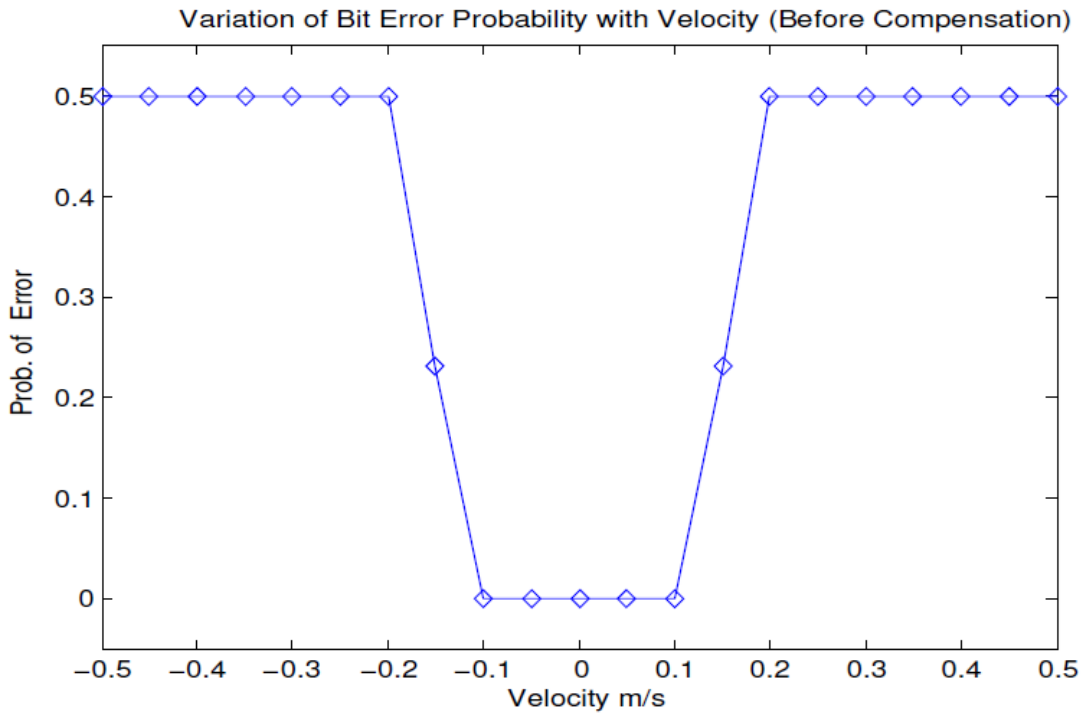

Figure 2.24: Intolerance of OFDM due to Doppler : Error Probability

Fig. 2.24 illustrates the intolerance of OFDM to Doppler. It is seen that a relative velocity above 10 cm/s leads to 100% error (Prob. of Error = 0.5) in the demodulated data. The only alternative is to incorporate a Doppler compensation technique which can cover a wider range of relative velocities. The resolution of the Doppler estimate obtained is dependent on the bandwidth B of the LFM signal and the packet length T_{tx} as given in (2.67)

We chose a packet length (T_{tx}) of 25s for OFDM data. The LFM signals used as frame sync have bandwidth of 3kHz. The Doppler resolution for the frame format can be found using (2.67) to be 2cm/s. From Figure 5.1, the system is able to tolerate a relative velocity estimation error upto 10 cm/s.

Fig. 2.25 illustrates the effect of Doppler compensation (re-sampling factor estimation) in the bit error rate. There is seen to be a remarkable improvement from the case where the system operated without any Doppler compensation. Without the compensation technique, system could not even tolerate relative velocities of the order 15 cm/s whereas with the described Doppler compensation technique, relative velocities of the order of 2 m/s (improvement of the order of 20) can easily be tolerated. We have seen that the packet length based estimation scheme is able to correctly estimate the Doppler

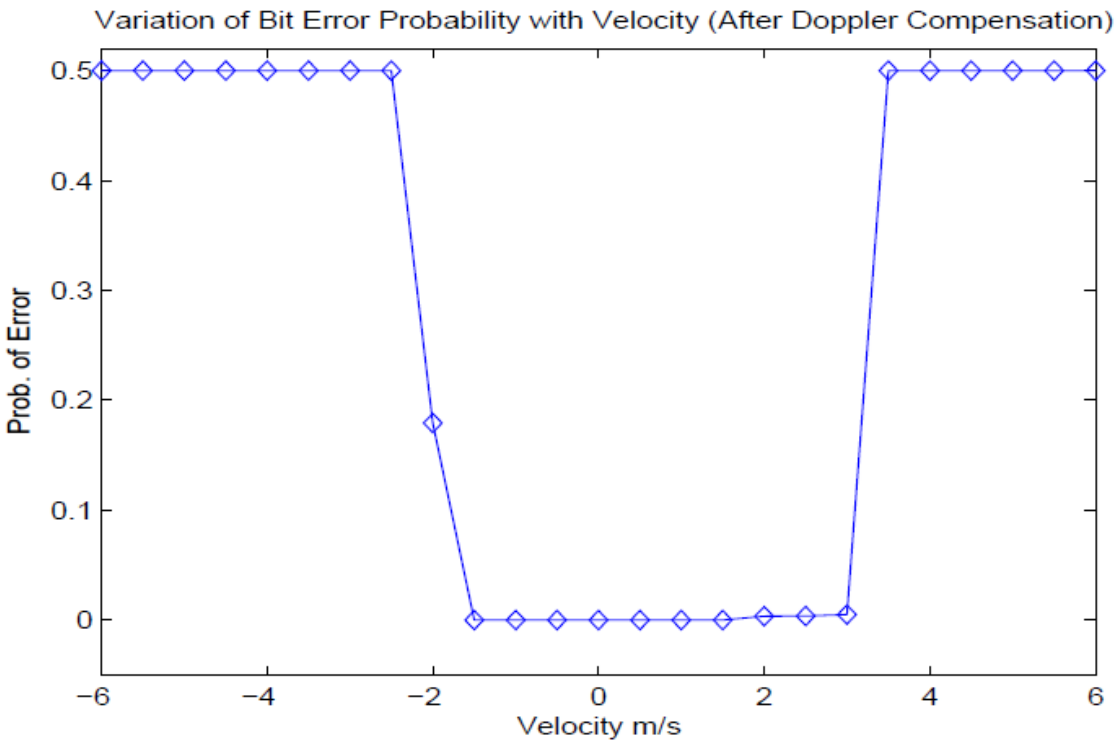

Figure 2.25: Estimation and Compensation of Doppler Shift with Re-sampling

even at higher relative velocities.

From Fig. 2.25, it is seen that the OFDM system can perform reliably only up to a relative velocity of 2m/s even with Doppler compensation. At higher relative velocities, the re-sampling of the time scaled signal is not able to recover the OFDM modulated signal even when the re-sampling factor is estimated correctly. In our system, the highest carrier frequency used is 9 kHz. The sampling frequency is fixed at 32 kHz. This implies that the number of samples per cycle for the largest carrier is approximately 3. This means even a single sample shift can result in a phase change of 120 degrees. Since the information is encoded in phase by the DQPSK modulation, a change of ± 45 degrees will lead to the error in the demodulation.

2.6 Desirable Variations of FM: LFM, QFM, Log FM, HFM

When there is a large relative velocity, the Doppler Effect is not negligible. In that case, pulse compression by means of a linear frequency modulation suffers from sig-

nificant signal loss in performance due to the mismatch between the received signal and the matched filter caused by the Doppler distortion. This problem can be avoided by using a hyperbolic frequency-modulated waveform, which has the inherent Doppler-invariant property. It is shown (J. Yang and Sarkar, 2006) that the hyperbolic frequency-modulated waveform is Doppler-invariant under the assumption that the target velocity is constant, while for a linear frequency-modulated waveform it is not. Other well-known variations of FM: QFM and Log FM are also numerically compared with LFM and HFM to get a complete picture.

Linear FM

The transmitted LFM (Chirp) waveforms in the pass band can be expressed as

$$x(t) = A(t)cos\left[2\pi\left(f_0 t + \frac{1}{2}kt^2\right)\right] \tag{2.68}$$

where $A(t)$ is the modulating signal or the envelope function, f_0 is the starting carrier frequency, and k is the frequency sweep rate. If the envelope $A(t)$ varies slowly in time when compared with the temporal change of the chirp carrier, the instantaneous frequency is the derivative of the phase term inside the cosine function, that is,

$$f(t) = \frac{d\left(f_0 t + \frac{1}{2}kt^2\right)}{dt} = f_0 + kt \tag{2.69}$$

Eqn (2.69) shows that the instantaneous frequency is a linear function of time, so it is called a linear frequency modulation. Hence the chirp signal is characterized by its start frequency (f_0), stop frequency (f_1), and time duration (T) as:

$$k = \frac{f_1 - f_0}{T} = \frac{B}{T} \tag{2.70}$$

If there is a relative movement, the received signal is Doppler distorted. This Doppler-distorted signal can be viewed as a function of two variables: a time delay caused by the distance and a Doppler scale caused by the relative velocity between the transmitter and the target. Assuming that both transmitted and returned signals have the same energy, then the returned signal can be expressed as (E.J. Kelly and Wishner,

1965)

$$r(t) = \sqrt{s}x[s(t-\tau)] \tag{2.71}$$

where $x(t)$ is the transmitted waveform; τ is the propagation time delay and s is the Doppler factor, respectively given by

$$\tau = \frac{D}{c} \tag{2.72}$$

$$s = \frac{c-v}{c+v} \tag{2.73}$$

where D is the distance between the transmitter and the receiver, c is the velocity of the signal propagation, and v is the relative velocity between the source and the target. Substituting (2.68) into (2.71), we obtain

$$r(t) = \sqrt{s}A[s(t-\tau)]cos\left[2\pi\left(f_0 s(t-\tau)+] + \frac{1}{2}k(s(t-\tau))^2\right)\right] \tag{2.74}$$

Similar to (2.69), the instantaneous frequency of the reflected signal is

$$f_d(t) = \frac{d\left(f_0 s(t-\tau) + \frac{1}{2}k(s(t-\tau))^2\right)}{dt} = sf_0 + s^2 k(t-\tau) \tag{2.75}$$

For a Doppler-invariant waveform, the following equation should be satisfied:

$$f(t) = f_d(t-t_0) \tag{2.76}$$

where t_0 is a constant time shift. Substituting (2.69) and (2.75) into (2.76), we can solve for t_0 as follows:

$$\begin{aligned} & f_0 + kt = sf_0 + s^2 k(t - t_0 - \tau) \\ \implies\ & t_0 = \frac{kt(s^2-1) + f_0(s-1)}{ks^2} - \tau \end{aligned} \tag{2.77}$$

The above equation indicates that for the linear frequency modulated waveform, t_0 is a function of time but not a constant; therefore, (2.11) is not satisfied. From (2.75), we can see that not only is the starting frequency changed, but also the rate of frequency

modulation rate is also changed. Therefore, when a single channel receiver is used, the received signal cannot stay matched to the matched filter, the amplitude of the peak value at the output of the matched filter will be significantly reduced, and the width of the compressed pulse will increase.

In all the following simulations, the FM duration (=0.1563sec) and band (=5-10kHz) is taken as same. The spectrogram and matched filter response (Compressed pulse) for different relative velocities are shown.

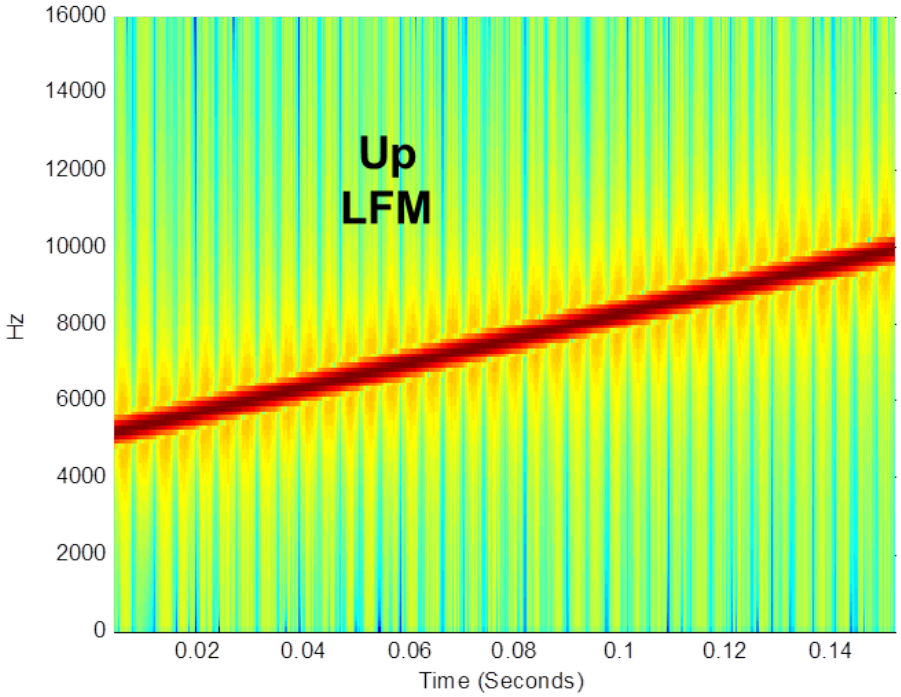

Figure 2.26: Spectrogram of an LFM with duration 0.1563sec and band 5-10kHz

2.6.1 Quadratic FM (QFM)

For Quadratic FM the instantaneous frequency is varied as a quadratic function of time, i.e

$$\begin{aligned} f(t) &= f_0 + kt^2 \\ \implies k &= \frac{f_1 - f_0}{t^2} \end{aligned} \tag{2.78}$$

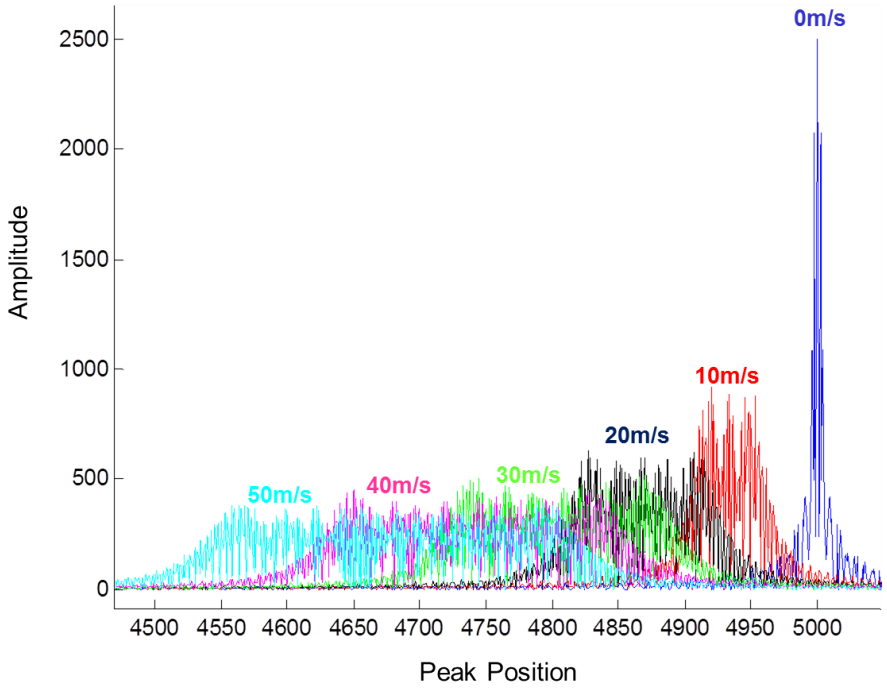

Figure 2.27: Compressed pulse for the LFM with different relative velocities

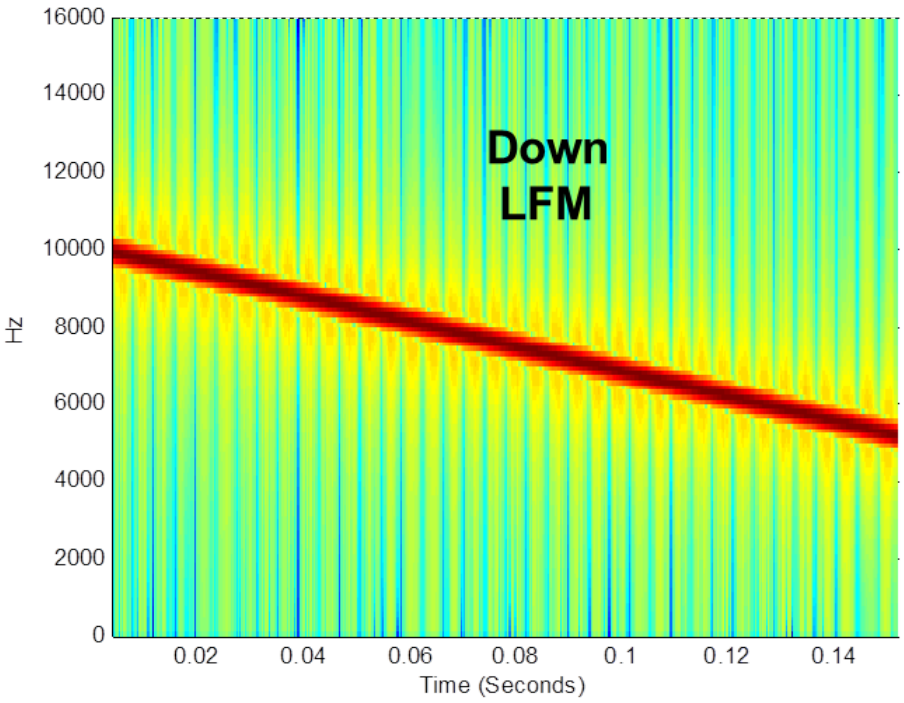

Figure 2.28: Spectrogram of an LFM with duration 0.1563sec and band 10-5kHz

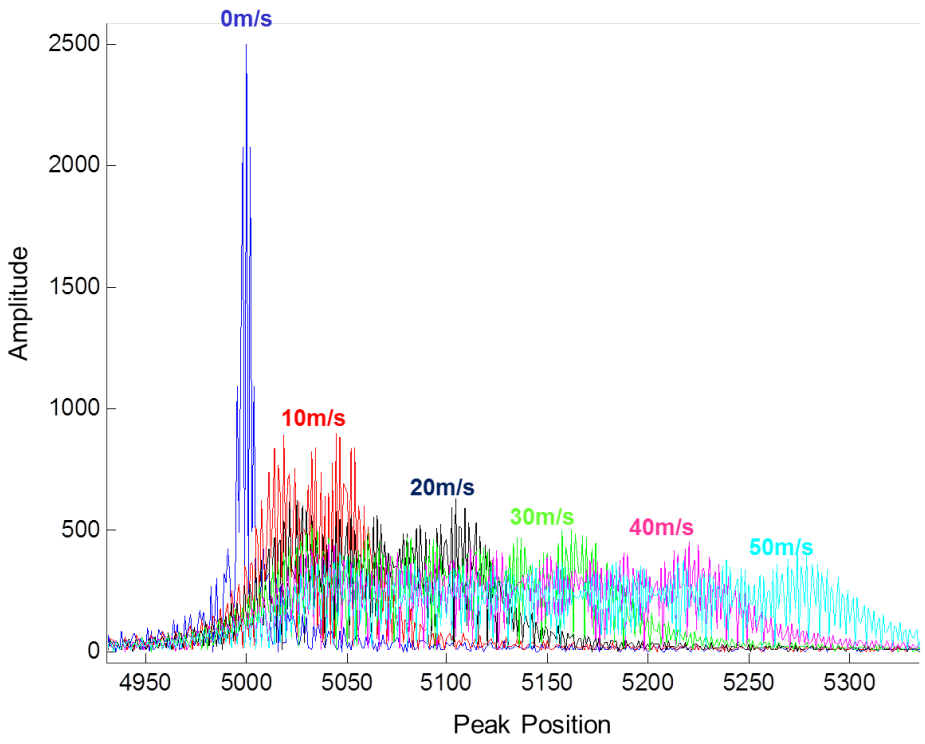

Figure 2.29: Compressed pulse for the Down-LFM with different relative velocities

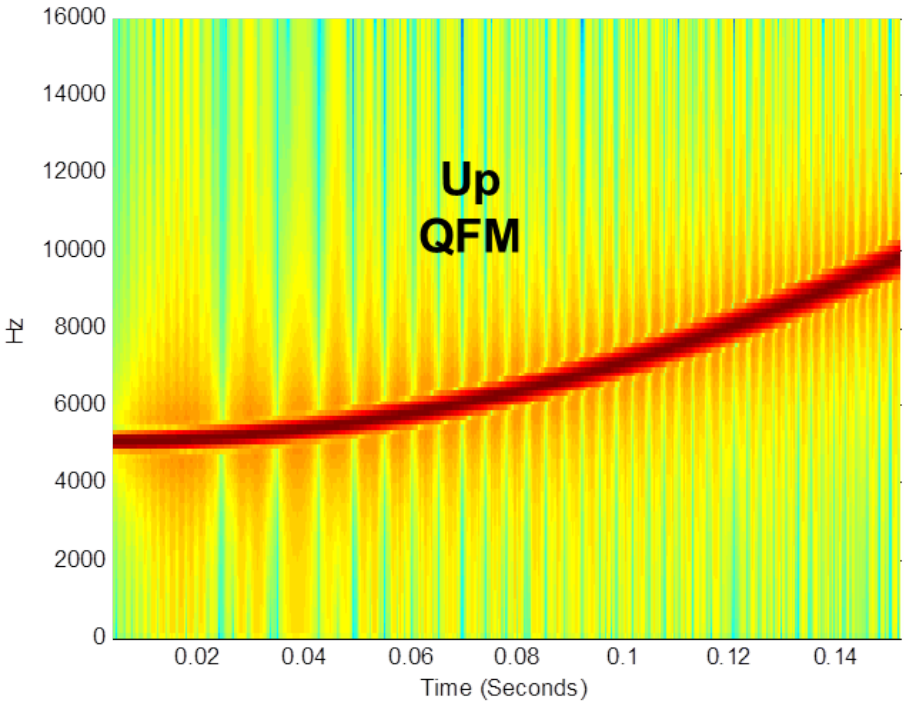

Figure 2.30: Spectrogram of a QFM with duration 0.1563sec and band 5-10kHz

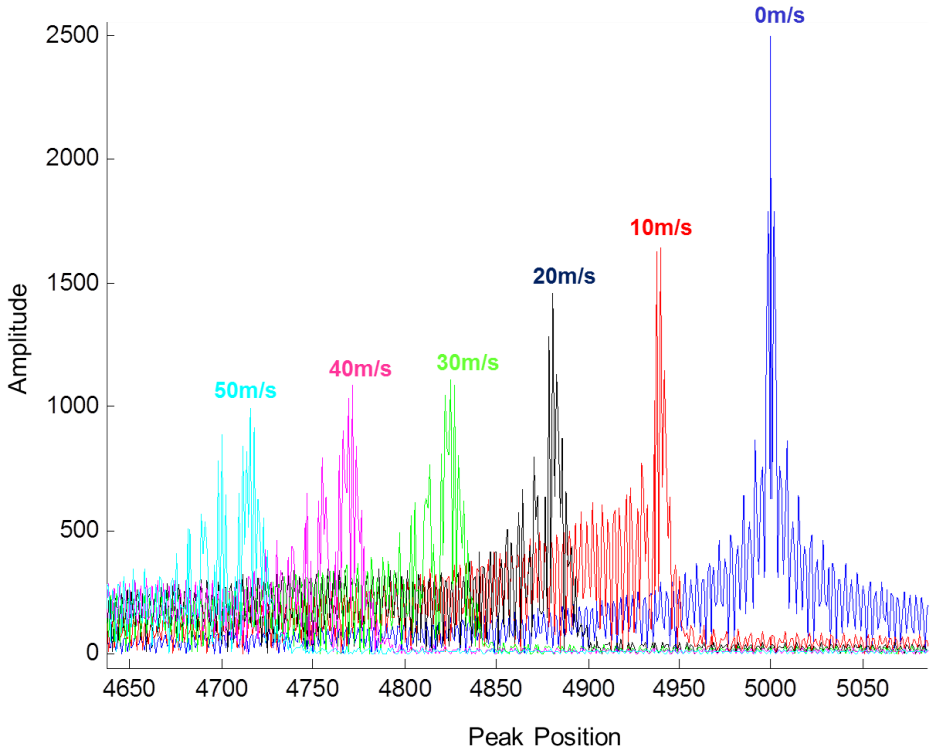

Figure 2.31: Compressed pulse for the QFM with different relative velocities

2.6.2 Logarithmic FM (Log FM)

For Logarithmic FM the instantaneous frequency is varied as a logarithmic function of time, i.e

$$\begin{aligned} f(t) &= f_0 k^t \\ \implies k &= \left(\frac{f_1}{f_0}\right)^{\frac{1}{t_1}} \end{aligned} \tag{2.79}$$

2.6.3 Hyperbolic FM (HFM)

Similar to (2.68), the hyperbolic frequency modulated pulse can be written as

$$x(t) = A(t)cos\left[\frac{2\pi}{k}log(1 + kf_0t)\right] \tag{2.80}$$

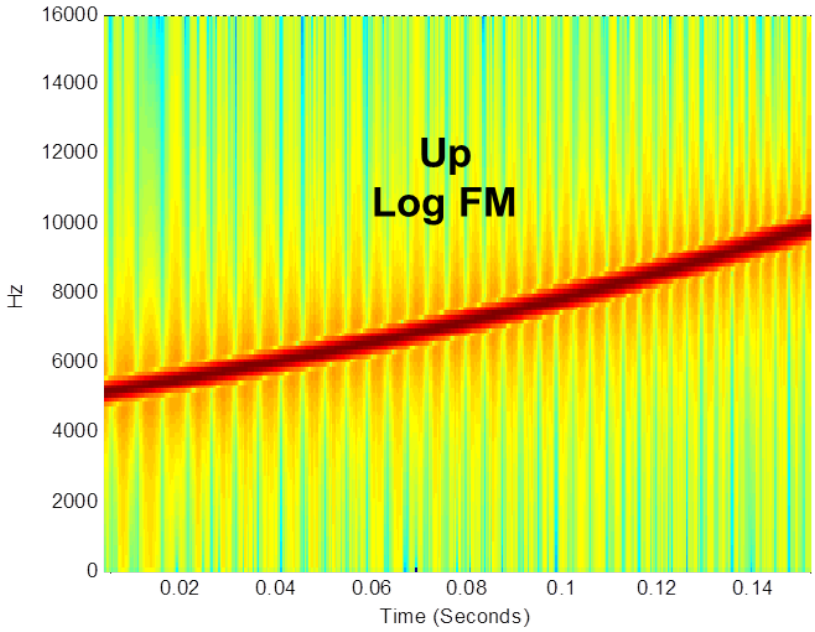

FM.png

Figure 2.32: Spectrogram of an Log FM with duration 0.1563sec and band 5-10kHz

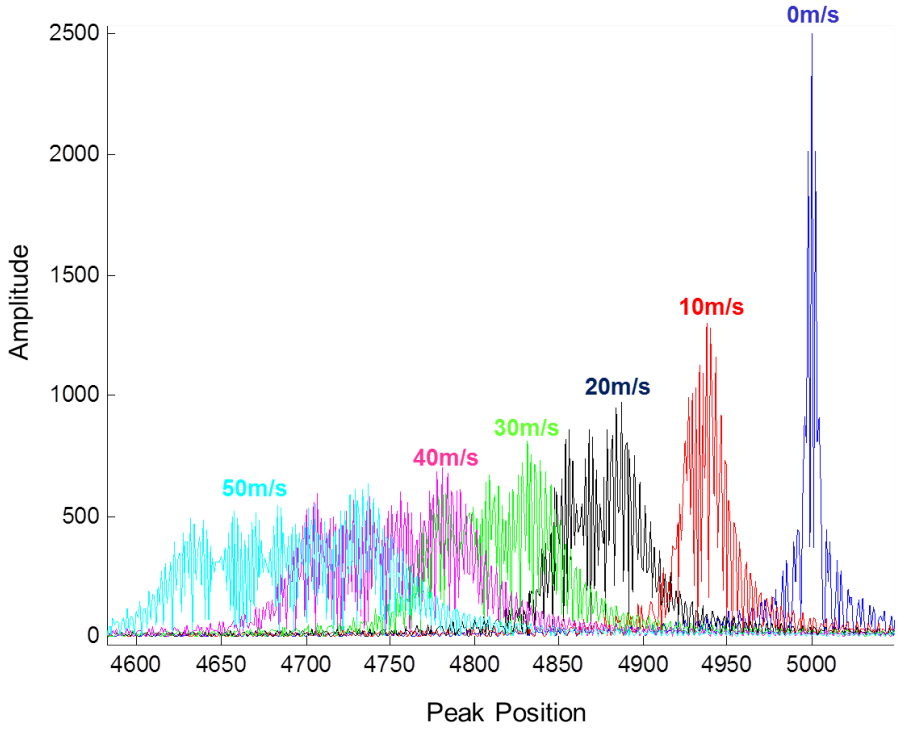

Figure 2.33: Compressed pulse for the Log FM with different relative velocities

where k is a constant factor and f_0 is the starting carrier frequency. The instantaneous frequency is the derivative of the phase term inside the cosine function:

$$f(t) = \frac{d\left[\frac{1}{k}log(1+kf_0t)\right]}{dt} = \frac{1}{1/f_0 + kt} \tag{2.81}$$

which is a hyperbolic function of time, so it is called hyperbolic frequency modulation. Substituting (2.80) into (2.69), the received signal is given by

$$r(t) = \sqrt{s}A[s(t-\tau)]cos\left[\frac{2\pi}{k}(log(1+kf_0s(t-\tau)))\right] \tag{2.82}$$

The instantaneous frequency of the received signal is

$$f_d(t) = \frac{d\left[\frac{1}{k}(log(1+kf_0s(t-\tau)))\right]}{dt} = \frac{1}{1/sf_0 + k(t-\tau)} \tag{2.83}$$

Again, substituting (2.81) and (2.83) into (2.11), we obtain

$$\begin{aligned} \frac{1}{1/f_0 + kt} &= \frac{1}{1/sf_0 + k(t - t_0 = \tau)} \\ \implies t_0 &= \frac{1-s}{ksf_0} - \tau \end{aligned} \tag{2.84}$$

Here, t_0 is a constant if we are assuming that the relative velocity between the transmitter and the receiver is a constant. (2.84) indicates that for a hyperbolic frequency modulated waveform, we can find a constant t_0 to satisfy (2.11), which means that the hyperbolic frequency modulated waveform is Doppler invariant.

2.6.4 Comparison of Scaling Factor Estimation Performance

The packet structure used for the scaling factor estimation is shown in the Fig. 2.36 The performance comparison of up-LFM and Down-LFM in the estimation of Doppler scale factor is shown in Fig. 2.37.

The performance comparison of up-LFM and up-QFM in the estimation of Doppler scale factor is shown in Fig. 2.38. The performance comparison of up-LFM and up-

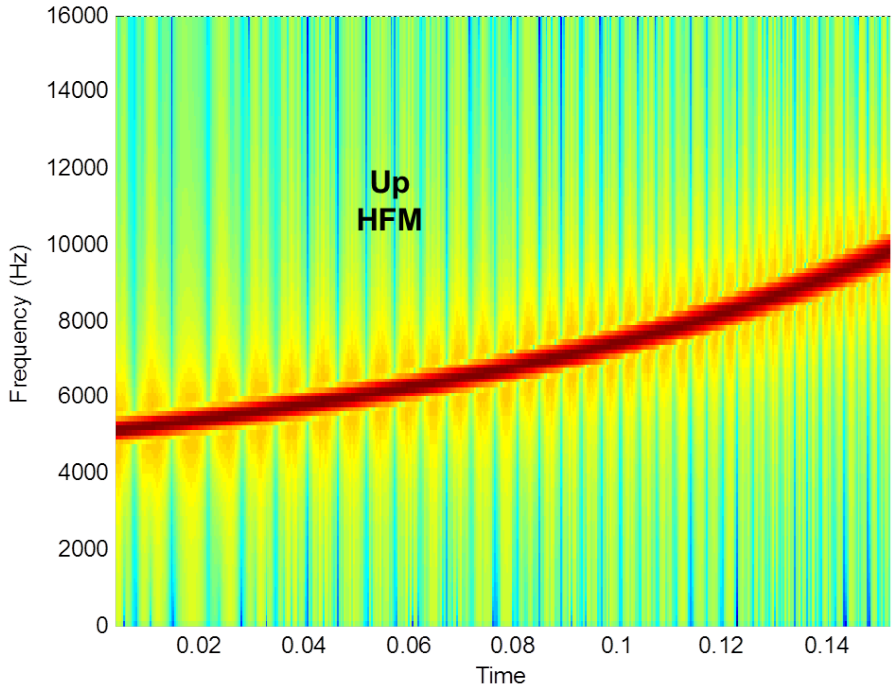

Figure 2.34: Spectrogram of an HFM with duration 0.1563sec and band 5-10kHz

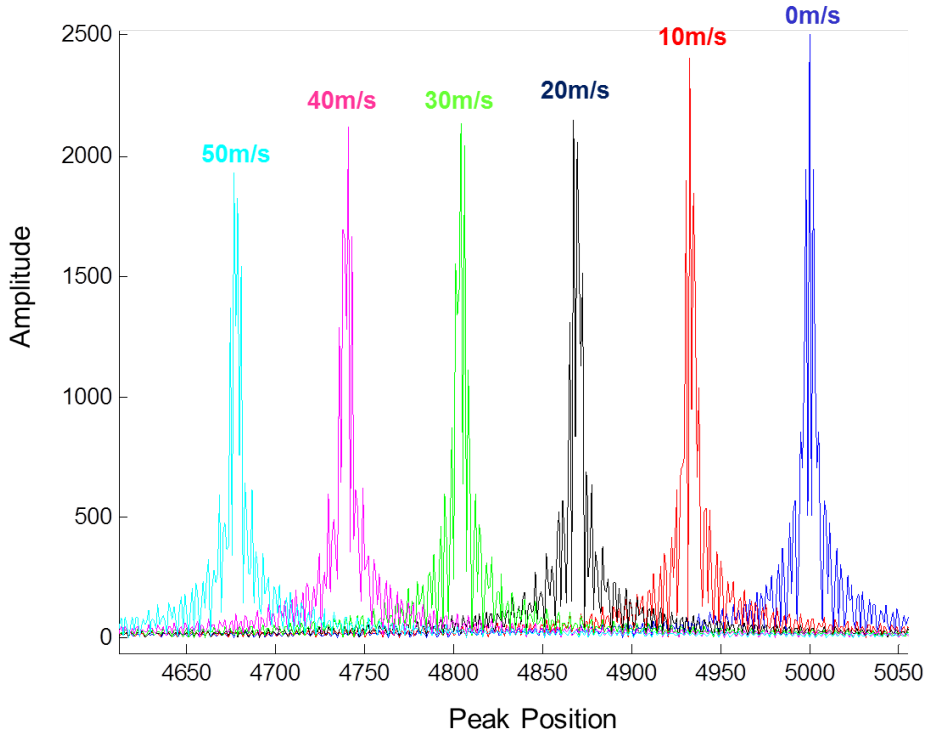

Figure 2.35: Compressed pulse for the HFM with different relative velocities

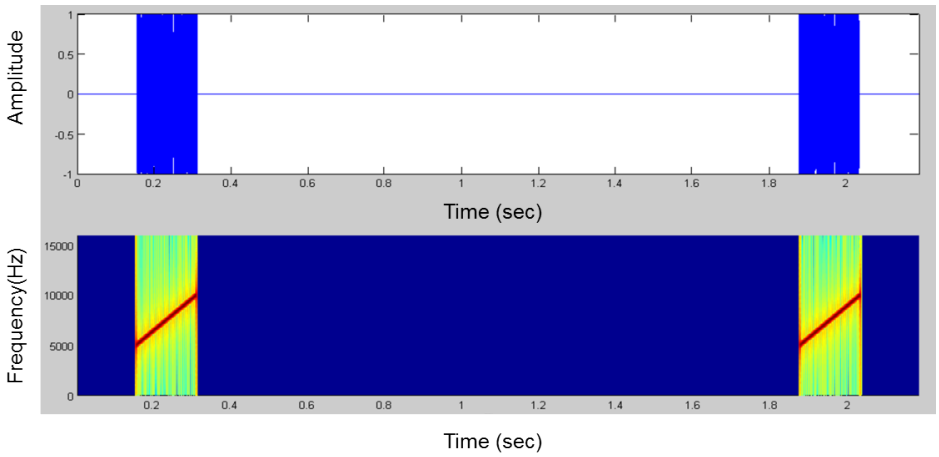

Figure 2.36: Time series and Spectrogram of the packet used for the scaling factor estimation

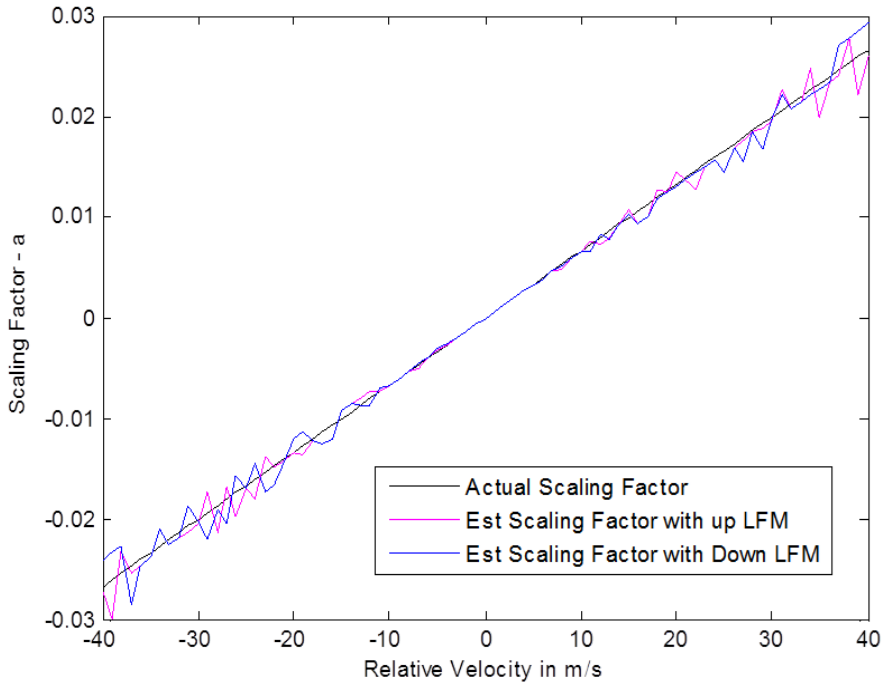

Figure 2.37: Comparison of up-LFM and Down-LFM in the estimation of scaling factor.

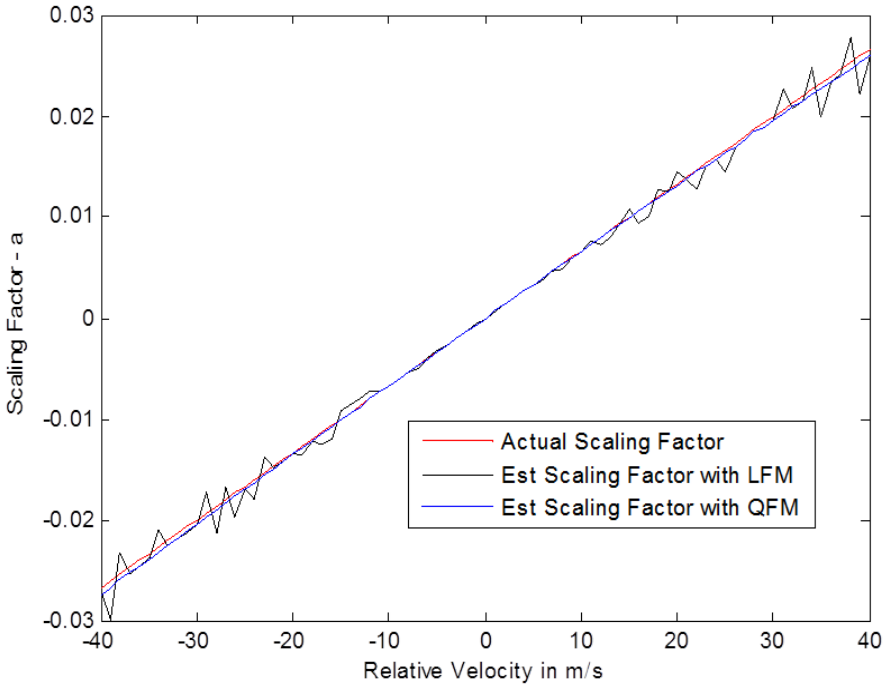

Figure 2.38: Comparison of LFM and QFM in the estimation of scaling factor

HFM in the estimation of Doppler scale factor is shown in Fig. 2.39. The performance comparison of up-LFM, up-QFM, up-HFM, up Log FM in the estimation of Doppler scale factor is shown in Fig. 2.40.

HFM clearly out performs LFM in the estimation of scaling factor a when the relative velocity is greater than 10m/s. Even though the estimation of the scaling factor is accurate over a wider range, we have seen that as per our present OFDM system spec, the Doppler compensation by re-sampling is effective only up to $\pm 3m/s$. Quadratic FM and Log FM also gives performance comparable to HFM. Performance of up and down FM are similar.

2.7 Packet length based Doppler scale Estimation: Limitations of the Assumptions

As mentioned earlier the assumptions involved are:

- A1: All paths have the same doppler rate a
- A2: The path gains A_p and the Doppler rate a are constant over the packet dura-

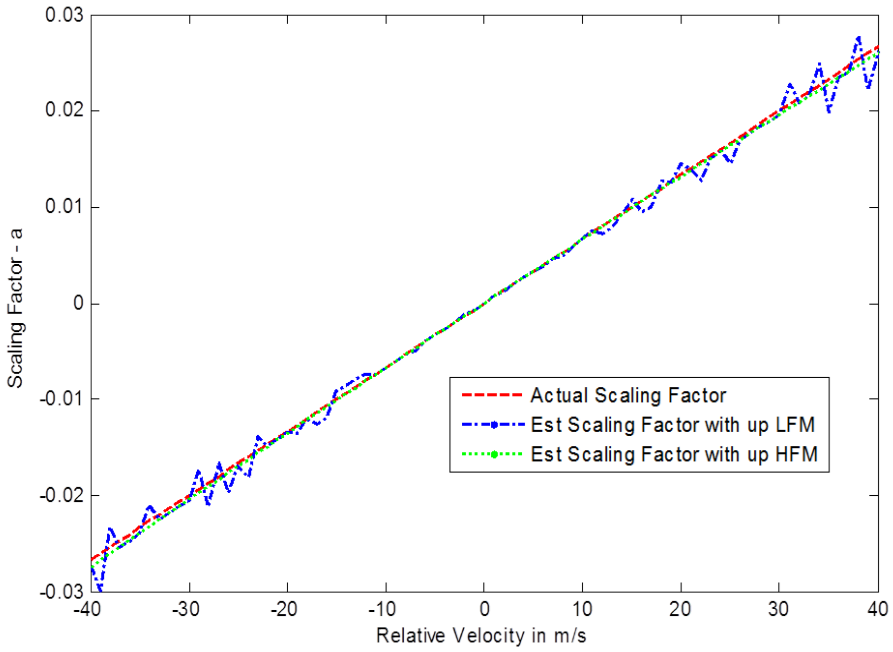

Figure 2.39: Comparison of LFM and HFM in the estimation of scaling factor

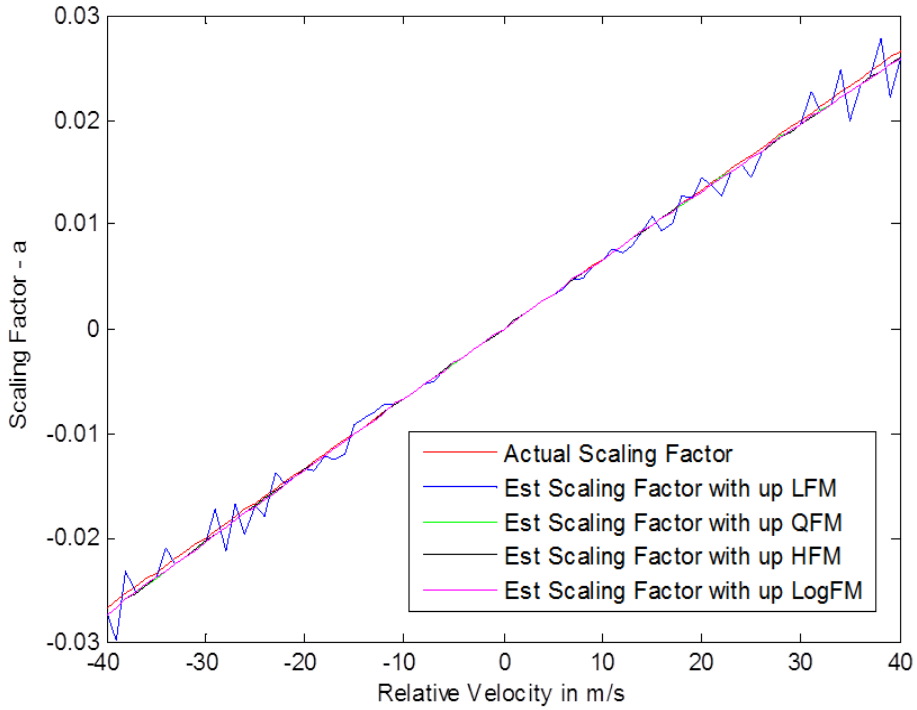

Figure 2.40: Comparison of up-LFM, HFM, QFM, Log FM in the estimation of scaling factor

tion T_{packet}.

This leads to following limitation:

- Valid when dominant Doppler scale is caused by the direct transmitter/receiver motion, NOT by the movement of sea surface or surroundings
- No acceleration, Relative velocity is assumed to be constant over frame duration. Frame size should be reduced to provide faster rate of Doppler correction
- Need to buffer the whole frame before data demodulation, which limits on-line real-time receiver
- It is assumed that the strongest path during the preamble and the post-amble is the same physical path, which is increasingly violated as the packet duration increases
- Time-scale resolution and hence the estimation accuracy may be inadequate for packets with very short durations
- For small delay spreads, it is observed that the error increases as each path does not necessarily produce a peak when the FM sequence is correlated with the received packet

CHAPTER 3

Performance and Design of Farrow Filter used for Arbitrary Re-sampling

3.1 Introduction

We have seen that Doppler compensation by inverse time scaling using the estimated Doppler time scale value is the key pre-processing required for underwater communication systems. Inverse time scaling can be implemented using arbitrary re-sampling in the discrete domain. The re-sampling factor depends on the relative velocity during the packet transmission interval; hence this can take any fractional number (rational or irrational). This chapter presents the design and implementation details of the re-sampler by an arbitrary factor.

3.2 Sample Rate conversion by an Arbitrary Factor:

Arbitrary re-sampling filters are designed and implemented as polyphase P-path filters. Each path provides a delay equal to an integer multiple of $1/P$ of the input sample interval for an up-sampler and of $1/P$ of the output sample interval for a down-sampler. Fig. 3.1 shows the functional structure of a 1-to-P up-sampling filter as P commutated stages.

Down sampling can be implemented concurrently with the up sampling by stepping through the commutator output ports in increments of Q to realize a rational ratio sample rate change of P/Q. In practice, the filter is implemented as a single stage with the commutation process relegated to pointers in coefficient (memory) space. When used for arbitrary re-sampling, the number of stages (P) in the filter is selected to be sufficiently large so that phase jitter artefacts due to selecting the nearest neighbour (to the desired interpolation point) is sufficiently small. This time jitter is shown in Fig. 3.2

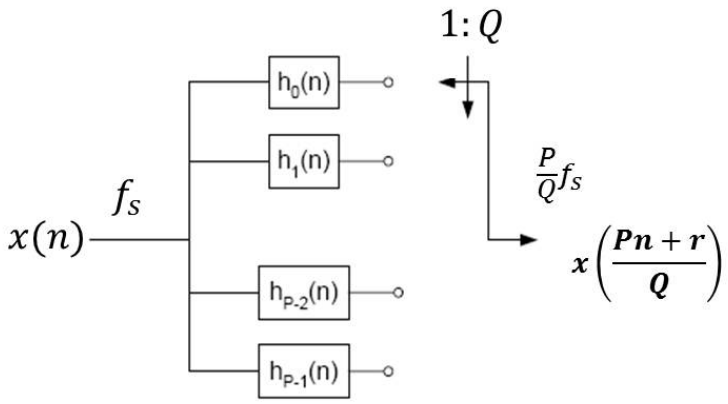

Figure 3.1: A Polyphase Up-Sampling Filter

where the desired output sample point is located between sample points k and $k+1$. The output is selected from the stage closest to the desired time position.

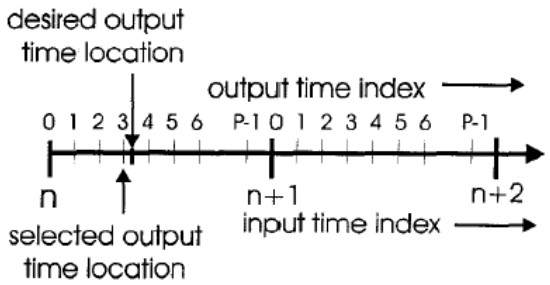

Figure 3.2: Input and Output Sample Location For P-Stage Re-sampling Filter

The nearest neighbour selection rule is equivalent to sampling an interpolating rectangle centred about each output sample. These rectangles, of width equal to the inter-sample spacing, can be visualized as the output of a zero-order hold (ZOH) applied to the output data. The ZOH has the effect of applying a $sin(Px)/Px$ to the periodic spectrum of the interpolated output sequence with the first zero located at the centre of the first spectral replicate of the 1-to-P up sampled spectrum. The $sin(Px)/(Px)$ zero crosses the replicate with a slope of $-l/P$, which while suppressing the replicate, leaves a residue of peak amplitude $1/(2P)$ (Harris, 1984) as shown in Fig. 3.3.

In a similar fashion to the nearest neighbour rule, Linear Interpolation between neighbours is equivalent to a triangle interpolation which applies a $[sin(Px)/(Px)]^2$ to the up-sampled periodic spectrum. The spectral residue levels due to linear interpolation is bounded by $2/(2P)^2$

The spectral residues due to zero and first order interpolation, located in the first and

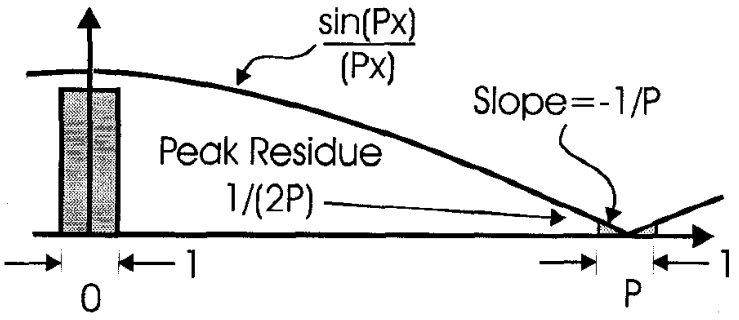

Figure 3.3: Spectral Residue from Interpolation with Nearest Neighbour Sampling

higher Nyquist zones, alias back into band when the 1-to-P up-sampled data is down-sampled Q-to-1 by the output commutator. Their number and final location is controlled by the specific re-sampling process. As a specific example, to hold spectral artefacts 50 dB below peak spectral levels, we require a 158 stage re-sampler when using the nearest neighbour rule and a 13 stage re-sampler when using a linear slope between neighbours. In both cases the in-band distortion due to the main lobe of $sin(Px)/(Px)$ or $[sin(Px)/(Px)]^2$ would be corrected by pre or post process equalization.

3.3 Compact Representation of Filter

We have a number of traditional methods to handle the coefficient sets required for the arbitrary re-sampling poly phase filter stages. In one option, we pre compute the weights for all expected re-sampling ratios and download the appropriate set upon selection of the re-sampling ratio. Another option is to extract the desired filter coefficients from a large array containing samples of a highly oversampled version of the desired low pass filter. In the limit, the prototype array would contain a continuous representation of the filter impulse response which we would then sample at the appropriate locations. In fact, a sufficiently highly oversampled prototype filter could supply the polyphase weights using nearest neighbour or linear interpolation of the table (Harris, 1984). Note, in this option, it is the table and not the signal that is interpolated. The spectral artefacts caused by sampling the prototype filter are the same levels as those obtained when we re-sampled the time series, namely $1/(2M)$ and $2/(2M)^2$ where M is the oversample ratio of the prototype filter.

The coefficient mapping of the polyphase filter stages is given by the Table 3.1

Table 3.1: The coefficient mapping of the polyphase filter stages

Stages \ Poly-phase coefficients ⟶					
	$h_0(n)$	$h_P(n)$			
	$h_1(n)$				
	.				
	$h_r(n)$				
	$h_{r+1}(n)$				
	.				
	$h_{P-1}(n)$				$h_{N-1}(n)$

FILTER LENGTH: An estimate of the length N/P of the polyphase stage filter can be found from (3.1) which defines the length N of the prototype filter. Here P is the up-sample ratio, f_s and Δf are the filter's input sample rate and transition bandwidth respectively while $K(\delta 1, \delta 2)$ is a proportionality factor related to the in-band and out-of-band ripple

$$N \cong P\frac{f_s}{\Delta f}K(\delta 1, \delta 2) \tag{3.1}$$

For in-band ripple levels appropriate to selected out-of-band levels, this constant $K(\delta 1, \delta 2)$ can be approximated by $ATTN(dB)/22$, where $ATTN(dB)$ is the filter's minimum stop band attenuation. The important concept here is that N/P, the polyphase filter length, is a constant dependent only on the filter's quality factors. Here quality is interpreted by the percentage of the sample rate allocated to the filter's transition bandwidth, and the depth of the filter's out-of-band side lobes.

3.4 Farrow Filter

The Farrow filter (C.W. Farrow, 1988) structure enables arbitrary re-sampling of time series by employing low order piecewise polynomials to approximate the segments of the impulse response of a prototype low-pass filter from which samples of arbitrary interpolator can be computed. Alternatively, the coefficients of the approximating polynomials can be applied directly to the input data to form, a data-dependent, polynomial

series expansion of the input data which can, in turn, be evaluated at the desired sample points.

Denoting the output sample by y, Row r would compute sample at time index $y(n+r/P)$ and row $r+1$ would compute a sample at time index $y(n+(r+1)/P)$. Need to calculate the output at the time index $r+\Delta$ between the polyphase stages r and $r+1$. For an arbitrary point Δ between stages r and $r+1$, a non-existing filter is needed to compute at sample $y(n+(r+\Delta)/P)$. How? Linear interpolation of filter outputs between the nearest neighbours is the same as the result of filtering the input with an equivalent filter obtained as by the interpolation of filter coefficients. Assuming $N/P = 4$

$$
\begin{aligned}
& y\left(n+\frac{r+\Delta}{P}\right) = y(n+r).(1-\Delta) + y(n+r+1)\Delta \\
\implies & y\left(n+\frac{r+\Delta}{P}\right) = (1-\Delta)\sum_{k=0}^{4} x(n-k)h_r(k) + \Delta\sum_{k=0}^{4} x(n-k)h_{r+1}(k) \\
\implies & y\left(n+\frac{r+\Delta}{P}\right) = \sum_{k=0}^{4} x(n-k)\left[(1-\Delta)h_r(k) + \Delta h_{r+1}(k)\right] \\
\implies & y\left(n+\frac{r+\Delta}{P}\right) = \sum_{k=0}^{4} x(n-k)h_{r+\Delta}(k)
\end{aligned}
\tag{3.2}
$$

This is simple yet useful result.

Referring to Fig. 3.4, the coefficient vector of each column in the polyphase structure can be considered as a P-sample approximation to a smooth continuous time function. Each column m can be approximated by a l^{th} order polynomial $P_m(x)$ where

$$P_m(x) = \sum_{l} b(l,m)x^l \tag{3.3}$$

The coefficients of the interpolation filter for the offset Δ is computed by evaluating the approximating polynomial $P_m(x)|_{x=\Delta}, \forall m$.

$$h_{r+\Delta}(m) = P_m(\Delta)|_{0\leq m\leq N-1} \tag{3.4}$$

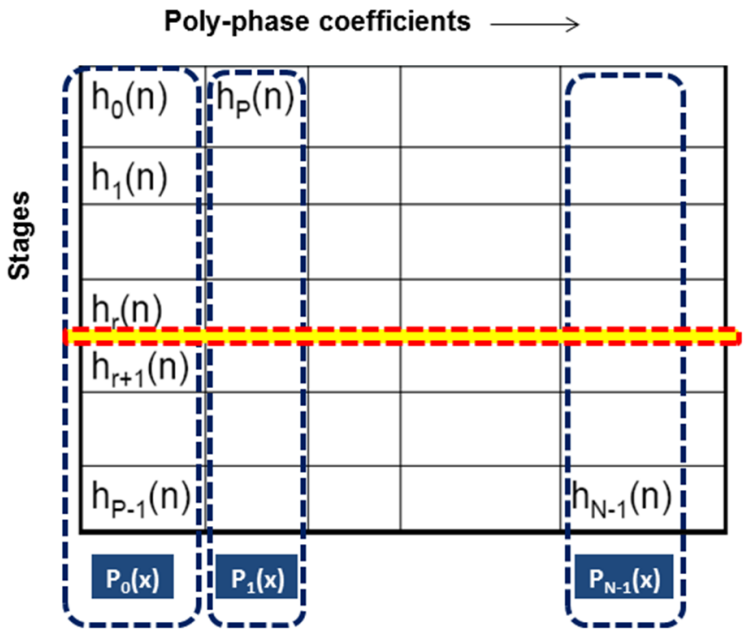

Figure 3.4: Two Dimensional Mapping of polyphase Filter Coefficient Set.

Is this not a complicated and computationally intensive procedure? No! Because we have the freedom to select the approximation polynomial $P_m()$ which decides the complexity and computational requirements. For practical purposes a cubic approximation is sufficient and stable numerical techniques can be applied.

Consider a cubic approximation ($l = 4$), the mathematical relations evolve as follows: Let the input time series be $x[n]$, the output time series be $y[n]$. The interpolated sample $y[n + \Delta]$ can be expressed as Time sample interpolation:

$$y[n + \Delta] = \sum_{m=0}^{4} h_{r+\Delta} \tag{3.5}$$

Polynomial Approximation:

$$\begin{aligned} y[n + \Delta] &= \sum_{m=0}^{4} \left\{ \sum_{l=0}^{4} b(l, m)\Delta^l \right\} x(n - m) \\ &= \sum_{l=0}^{4} \Delta^l \left\{ \sum_{m=0}^{4} b(l, m)x(n - m) \right\} \\ &= \sum_{l=0}^{4} c(n, l)\Delta^l \end{aligned} \tag{3.6}$$

where

$$c(n,l) = \sum_{m=0}^{4} b(l,m)x(n-m) \tag{3.7}$$

Computation of $c(n,l)$ is independent of Δ. For a given re-sampling factor the Δ is not a constant, but it is a function of output sample index as shown in the following section

3.5 Design of Farrow Filter

The following steps leading to the design of Farrow interpolator structures for the piece-wise cubic interpolators closely follow (Rice, 2008).

T-spaced samples of the band limited continuous time signals $x(t)$ are available and denoted by $\cdots, x\left((n-1)T\right), x\left((n)T\right), x\left((n+1)T\right), x\left((n+2)T\right), \cdots$

The commonly used terms to describe interpolation are illustrated by the diagram in Fig. 3.5

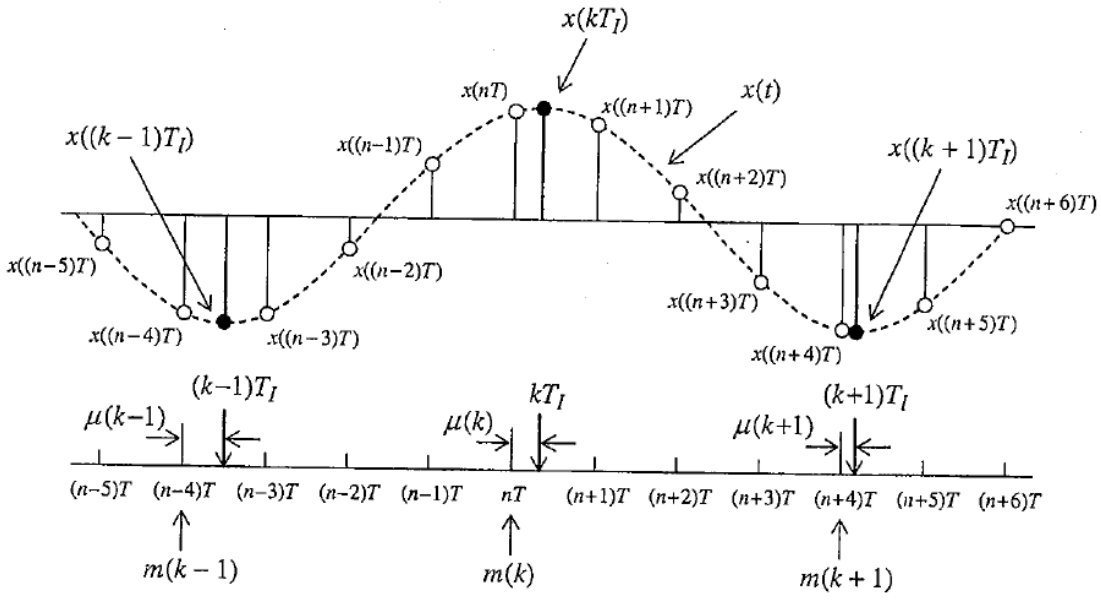

Figure 3.5: Illustration of the relationships between the interpolation interval T_I, the sample time T, the base point indexes, and fractional intervals.

The desired sample is a sample of $x(t)|_{t=kT_I}$ and is called the k^{th} interpolant. The process used to compute $x(kT_I)$ from the available samples is called interpolation. When the k^{th} interpolant is between samples $x(nT)$ and $x(n+1)T$, the sample in-

dex n is called the k^{th} base-point index and is denoted $m(k)T$. The time instant kT_I is some fraction of a sample time greater than $m(k)T$. This fraction is called the k^{th} fractional interval and is denoted $\mu(k)$. The k^{th} fractional interval satisfies $0 < \mu(k) < 1$ and is defined by $\mu(k)T = kT_I - m(k)T$. The fundamental equation for interpolation may be derived by considering a fictitious system involving continuous-time processing illustrated in Fig. 3.6.

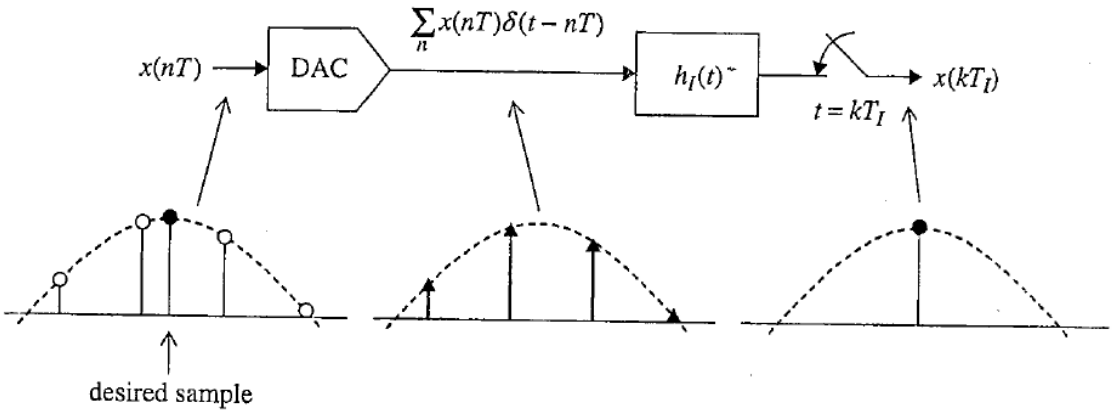

Figure 3.6: Fictitious system using continuous-time processing for performing interpolation.

The samples $x(nT)(n = 0, 1, \cdots)$ are converted to a weighted impulse train

$$x_a(t) = \sum_n x(nT)\delta(t - nT) \tag{3.8}$$

by the digital-to-analog converter (DAC). The impulse train is filtered by an interpolating filter with impulse response $h_I(t)$ to produce the continuous-time output $x(t)$. The continuous-time signal $x(t)$ may be expressed as

$$x(t) = \sum_n x(nT)h_I(t - nT) \tag{3.9}$$

To produce the desired interpolants, $x(t)$ is re-sampled at intervals $kT_I(k = 0, 1, \cdots)$. The k^{th} interpolant is (3.9) evaluated at $t = kT_I$ and may be expressed as

$$x(kT_I) = \sum_n x(nT)h_I(kT_i - nT) \tag{3.10}$$

The variable n indexes the signal samples. The convolution sum (3.10) may be re-

expressed using a filter index i. Using $m(k) = \lfloor kT_I/T \rfloor$ and $\mu(k) = kT_I/T - m(k)$, the filter index is $i = m(k) - n$. Using the filter index, equation (3.10) may be expressed as

$$x(kT_I) = \sum_i x((m(k) - i)T)h_I((i + \mu(k))T) \tag{3.11}$$

Equation (3.11) will serve as the fundamental equation for interpolation and shows that the desired interpolant can be obtained by computing a weighted sum of the available samples. The optimum interpolation filter is an ideal low-pass filter whose impulse response is

$$h_I(t) = \frac{sin(\pi t/T)}{\pi t/T} \tag{3.12}$$

Given a fractional interval μ the ideal impulse response is sampled at $t = iT - \mu T$ to produce the filter coefficients required by (3.11).

3.5.1 Piecewise Polynomial Interpolation

The underlying continuous-time waveform $x(t)$ is approximated by a polynomial in t of the form

$$x(t) \approx c_p t^p + c_{p-1} t^{p-1} + \cdots c_1 t + c_0 \tag{3.13}$$

The polynomial coefficients are determined by the $(p+1)$ sample values surrounding the base point index. Once the coefficient values are known, the interpolant at $t = kT_I = (m(k) + \mu(k))T$ is obtained using

$$x(kT_I) \approx c_p (kT_I)^p + c_{p-1} (kT_I)^{p-1} + \cdots c_1 (kT_I) + c_0 \tag{3.14}$$

Three special cases, p = 1, 2, and 3 are of interest and are illustrated in Fig. 3.7. When p= 1, the first degree polynomial

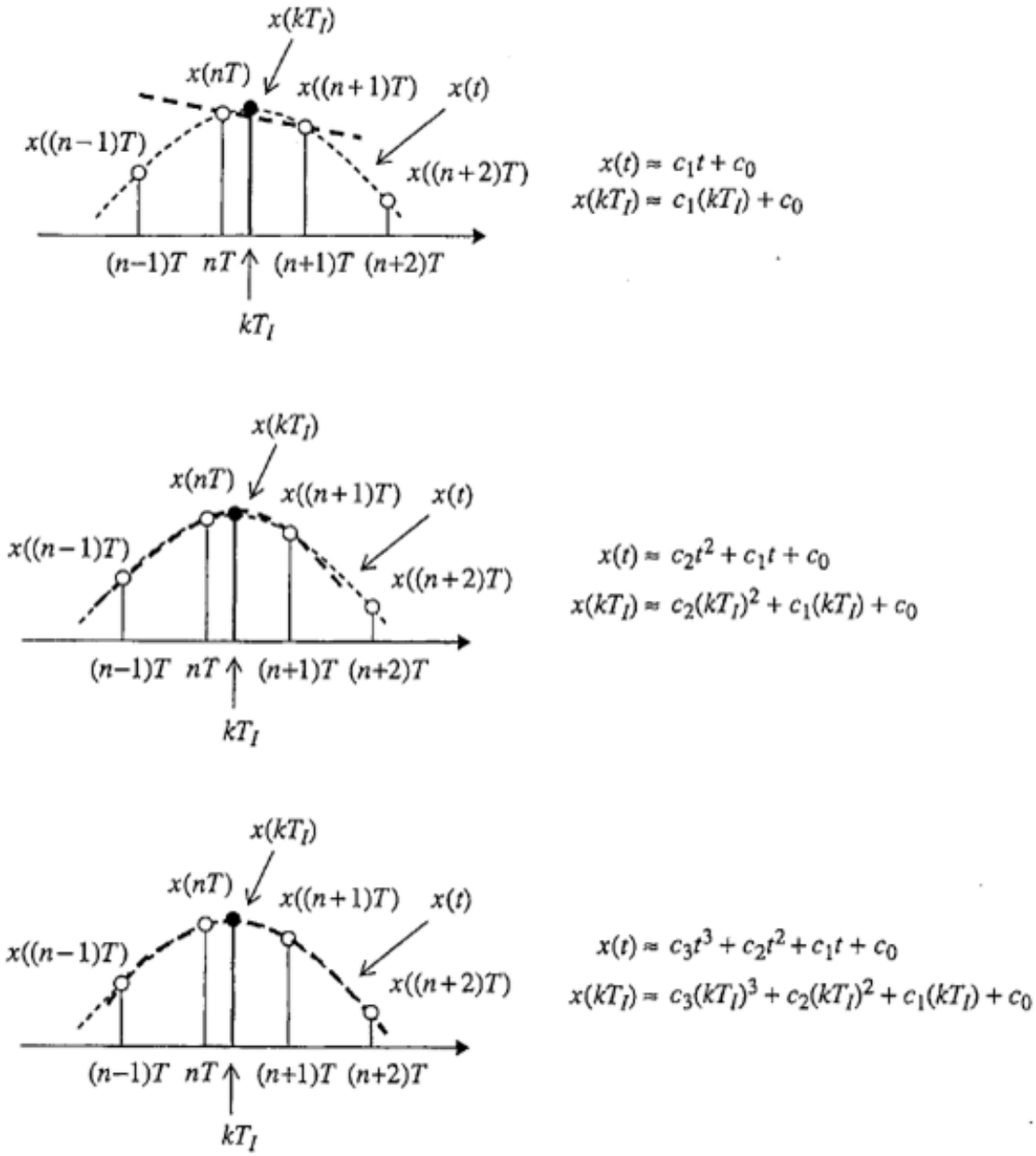

Figure 3.7: Three special cases of polynomial interpolation: (top) linear interpolation, (middle) quadratic interpolation and (bottom) cubic interpolation

$$x(t) \approx c_1 t + c_0 \tag{3.15}$$

is used to approximate the underlying continuous-time waveform. The desired interpolants are computed from

$$x((m(k) + \mu(k))T = c_1((m(k) + \mu(k))T) + c_0 \tag{3.16}$$

The coefficients c_1 and c_0 are determined by the available samples and satisfy the equation

$$\begin{bmatrix} x(m(k)T) \\ x((m(k)+1)T) \end{bmatrix} = \begin{bmatrix} m(k)T & 1 \\ (m(k)+1)T & 1 \end{bmatrix} \begin{bmatrix} c_1 \\ c_0 \end{bmatrix} \tag{3.17}$$

Solving the above for c_1 and c_0 and substituting into (3.16) produces

$$x((m(k) + \mu(k))T) = \mu(k)x((m(k)+1)T) + (1 - \mu(k))x(m(k)T) \tag{3.18}$$

which is the familiar linear interpolator. Four observations are important:

- **The first is that the interpolant is a linear combination of the available samples**. As a consequence, the interpolant can be thought of as the output of a filter with coefficients suggested by (3.18):

$$x((m(k) + \mu(k))T) = \sum_{i=-1}^{0} h_1(i)x((m(k) - i)T) \tag{3.19}$$

  where

$$\begin{aligned} h_1(-1) &= \mu(k) \\ h_1(0) &= 1 - \mu(k) \end{aligned} \tag{3.20}$$

- **The second important observation is that the equivalent filter coefficients are a function only of the fractional interval and not a function of the base-point index**. The base-point index defines which set of samples should be used to compute the interpolant.

- **The third observation is that the interpolating filter is linear phase FIR filter**, which is an extremely important property for digital communications. To see that this filter is linear phase, note that the coefficients are symmetric about the center point of the filter that is defined by $\mu(k) = 1/2$. In other words, $h((m+1/2)T) =$

$h((-m+1/2)T)$ for $m = 0, 1, 2, \cdots$.This is a result of using an even number of samples to compute an interpolant that is between the middle two.

- **The final observation is that the sum of the coefficients is unity and is therefore independent of $\mu(k)$.**

As a consequence, the interpolating filter does not alter the amplitude of the underlying continuous-time waveform in the process of producing the interpolant. The second observation is an attractive feature because any finite precision computing device would eventually overflow as $m(k)$ increased. The third property requires the use of an even number of samples by the interpolator. An even number of samples is needed to define an odd-degree approximating polynomial. For this reason, odd-degree approximating polynomials are popular. The next highest odd-degree polynomial is p = 3. In this case

$$x(t) \approx c_3 t^3 + c_2 t^2 + c_1 t + c_0 \tag{3.21}$$

is used to approximate the underlying continuous-time waveform. The desired interpolants are computed from

$$x((m(k)+\mu(k))T) \approx c_3(m(k)+\mu(k)^3+c_2(m(k)+\mu(k)^2+c_1(m(k)+\mu(k)+c_0 \tag{3.22}$$

The coefficients c_3, c_2, c_1, and c_0 are defined by

$$\begin{bmatrix} x((m(k)-1)T) \\ x(m(k)T) \\ x((m(k)+1)T) \\ x((m(k)+2)T) \end{bmatrix} = \begin{bmatrix} ((m(k)-1)T)^3 & ((m(k)-1)T)^2 & (m(k)-1)T & 1 \\ (m(k)T)^3 & (m(k)T)^2 & m(k)T & 1 \\ ((m(k)+1)T)^3 & ((m(k)+1)T)^2 & (m(k)+1)T & 1 \\ ((m(k)+2)T)^3 & ((m(k)+2)T)^2 & (m(k)+2)T & 1 \end{bmatrix} \begin{bmatrix} c_3 \\ c_2 \\ c_1 \\ c_0 \end{bmatrix} \tag{3.23}$$

Solving the above for c_3, c_2, c_1, and c_0 and substituting into (3.22) produces

$$\begin{aligned} x((m(k)+\mu(k))T) = &\left(\frac{\mu(k)^3}{6} - \frac{\mu(k)}{6}\right) x((m(k)+2)T) \\ &- \left(\frac{\mu(k)^3}{2} - \frac{\mu(k)^2}{2} - \mu(k)\right) x((m(k)+1)T) \\ &+ \left(\frac{\mu(k)^3}{2} - \mu(k)^2 - \frac{\mu(k)}{2} + 1\right) x(m(k)T) \\ &- \left(\frac{\mu(k)^3}{6} - \frac{\mu(k)^2}{2} - \frac{\mu(k)}{3}\right) x((m(k)-1)T) \end{aligned} \tag{3.24}$$

which is called a cubic interpolator. When interpreted as a filter, the cubic interpolator output is of the form

$$x((m(k)+\mu(k))T) = \sum_{i=-2}^{1} h_3(i) x((m(k)-i)T) \tag{3.25}$$

where the filter coefficients are

$$\begin{aligned} h_3(-2) &= \frac{\mu(k)^3}{6} - \frac{\mu(k)}{6} \\ h_3(-1) &= -\frac{\mu(k)^3}{2} + \frac{\mu(k)^2}{2} + \mu(k) \\ h_3(0) &= \frac{\mu(k)^3}{2} - \mu(k)^2 - \frac{\mu(k)}{2} + 1 \\ h_3(1) &= -\frac{\mu(k)^3}{6} + \frac{\mu(k)^2}{2} - \frac{\mu(k)}{3} \end{aligned} \tag{3.26}$$

Using piecewise polynomial interpolator to produce the desired interpolant result in a computation of the form

$$x((m(k)+\mu(k))T) = \sum_{i=-I_1}^{I_2} h_p(i;\mu(k)) x((m(k)-i)T) \tag{3.27}$$

Comparing (3.27) with the fundamental interpolation equation (3.27) shows that the filter coefficients $h_p(i;\mu(k))$ play the role of approximating the samples of the ideal interpolation filter $h_I((i-\mu(k))T)$. Plots of $h_1(i;\mu(k)), h_2(i;\mu(k))$, and $h_3(i;\mu(k))$, are shown in Fig. 3.8. Observe that as p increases, $h_p(i;\mu(k))$, approximates (3.12) with greater and greater accuracy. In fact, in the limit $p \to \infty, h_p(i;(k))$, approaches

(3.12).

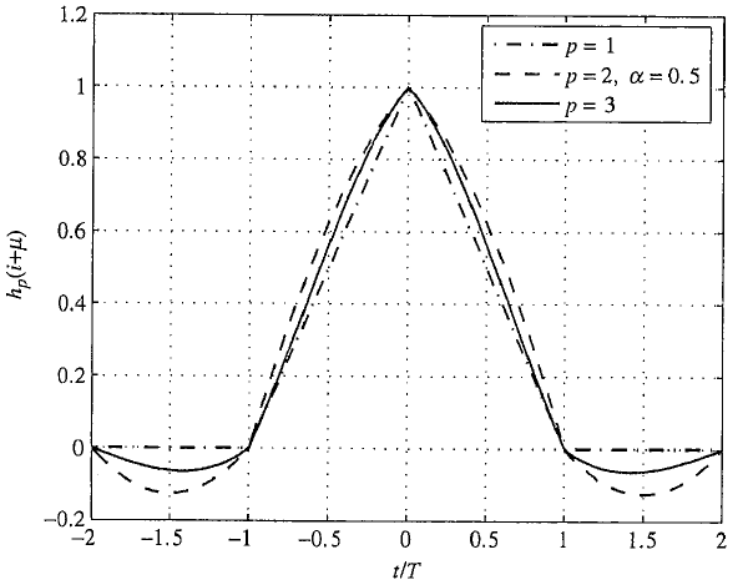

Figure 3.8: Plot of the filter impulse responses resulting from piecewise polynomial interpolation

Since the filter coefficients suggested by the filter structure defined by (3.20), and (3.26), are a function of the variable $\mu(k)$, a hardware implementation requires two-input multipliers with two variable quantities. The complexity can be reduced by formulating the problem in terms of two-input multipliers where one of the inputs is fixed. To do this, observe that each filter coefficient $h_p(i;\mu(k))$ in (3.27) may be written as a polynomial in $\mu(k)$, Let

$$h_p(i;\mu(k)) = \sum_{l=0}^{p} b_l(i)\mu(k)^l \tag{3.28}$$

represent the polynomial. Substituting (3.28) into (3.27) and rearranging produces

$$x((m(k)+\mu(k))T) = \sum_{l=0}^{p} \mu(k)^l \underbrace{\sum_{i=I_1}^{I_2} b_l(i)x((m(k)-i)T)}_{v(l)} \tag{3.29}$$

The inner sum looks like a filter equation where the input data samples $x((m(k)i)T)$ pass through a filter with impulse response $b_l(i)$. The $b_l(i)$ are independent of $\mu(k)$. Thus, this filter has fixed coefficients and an efficient implementation. Computing

(3.29) by nested evaluation produces an expression of the form

$$x((m(k)+\mu(k))T = \{[v(3)\mu(k)+v(2)]\,\mu(k)+v(1)\}\,\mu(k)+v(0) \tag{3.30}$$

for cubic interpolation. This is called Horner's rule(Rice, 2008). Mapping these expressions to hardware results in an efficient filter structure called the Farrow structure illustrated in Fig. 3.9. The Farrow coefficients for the Farrow structure are listed in Table 3.2

Table 3.2: Farrow coefficients $b_l(i)$ for the cubic interpolator(Rice, 2008)

i	$b_3(i)$	$b_2(i)$	$b_1(i)$	$b_0(i)$
-2	$\frac{1}{6}$	0	$-\frac{1}{6}$	0
-1	$-\frac{1}{2}$	$\frac{1}{2}$	1	0
0	$\frac{1}{2}$	-1	$-\frac{1}{2}$	1
1	$-\frac{1}{6}$	$\frac{1}{2}$	$-\frac{1}{3}$	0

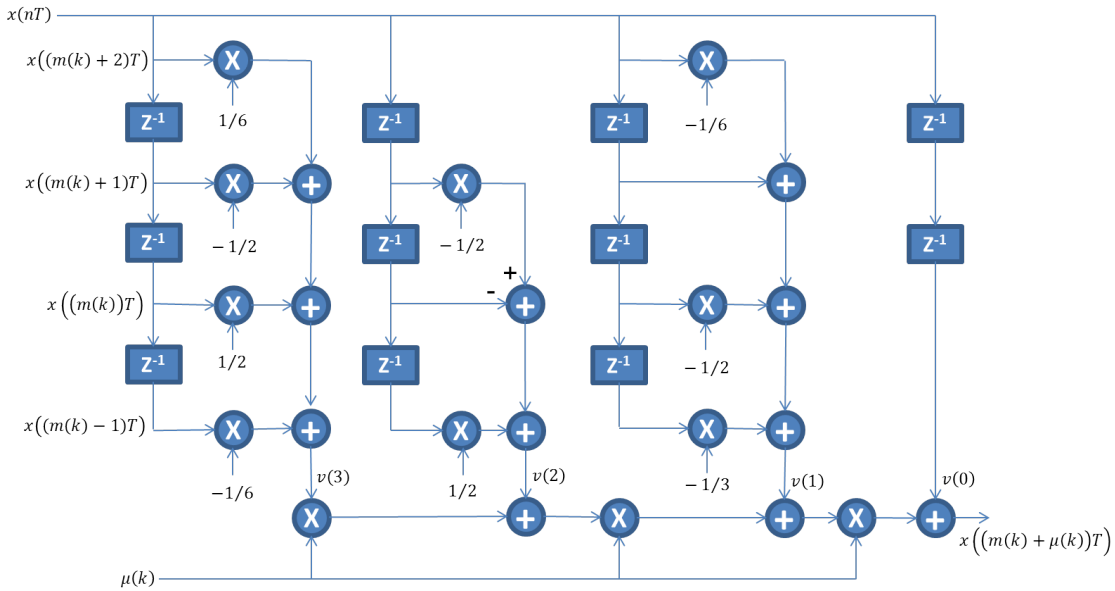

Figure 3.9: Farrow interpolator structures for the piecewise cubic interpolators(Rice, 2008)

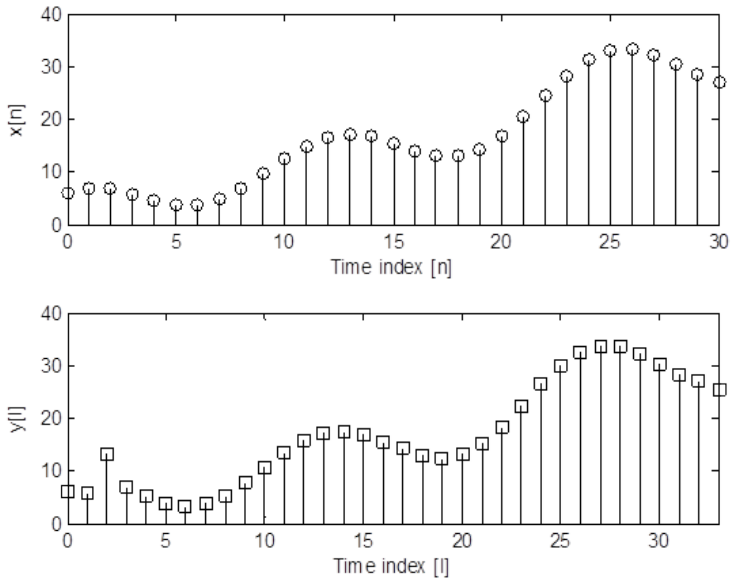

Figure 3.10: Matlab Example:Sampling-rate alteration by the fractional factor $R = 16/15$

CHAPTER 4

Conventional Synchronization Techniques Applicable to Narrowband OFDM Systems

The advantage of OFDM can be useful only when the orthogonality of the sub-carriers is maintained. If orthogonality is not sufficiently maintained by some means, OFDM performance may be degraded due to inter-symbol interference (ISI) and inter-channel interference (ICI). In this chapter, we will analyse the effects of symbol timing offset (STO) and carrier frequency offset (CFO), and then discuss the synchronization techniques to handle the potential STO and CFO problems in OFDM systems. Let ϵ and δ denote the normalized CFO and STO, respectively. The l^{th} OFDM symbol of received baseband signal under the presence of CFO (ϵ) and STO (δ) can be expressed as

$$\begin{aligned} y_l[n] =& IDFT\left\{Y_l[k]\right\} = IDFT\left\{H_l[k]X_l[k] + Z_l[k]\right\} \\ =& \frac{1}{N}\sum_{k=0}^{N-1} H_l[k]X_l[k]e^{j2\pi(k+\epsilon)(n+\delta)/N} + z_l[n] \end{aligned} \tag{4.1}$$

where $z_l[n] = IDFTZ_l[k]$.

4.1 Effect of Symbol Timing Offset

IFFT and FFT are the fundamental functions required for the modulation and demodulation at the transmitter and receiver of OFDM systems, respectively. In order to take the N-point FFT in the receiver, we need the exact samples of the transmitted signal for the OFDM symbol duration. In other words, a symbol-timing synchronization must be performed to detect the starting point of each OFDM symbol (with the CP removed), which facilitates obtaining the exact samples. Table 4.1 shows how the STO of δ samples affects the received symbols in the time and frequency domain where the effects of channel and noise are neglected for simplicity of exposition. Note that the STO of δ in

the time domain incurs the phase offset of $2\pi k\delta/N$ in the frequency domain, which is proportional to the sub-carrier index k as well as the STO δ.

Table 4.1: The effect of symbol timing offset (STO).

	Received signal	STO (δ)
Time domain	$y[n]$	$x[n+\delta]$
Frequency domain	$Y[k]$	$e^{j2\pi k\delta/N}X[k]$

Depending on the location of the estimated starting point of OFDM symbol, the effect of STO might be different. Fig. 4.1 shows four different cases of timing offset, in which the estimated starting point is exact, a little earlier, too early, or a little later than the exact timing instance. Here, we assume that the multi-path delay spread incurs the lagged channel response of τ_{max}. In the current analysis, the effects of the noise and channel are ignored.

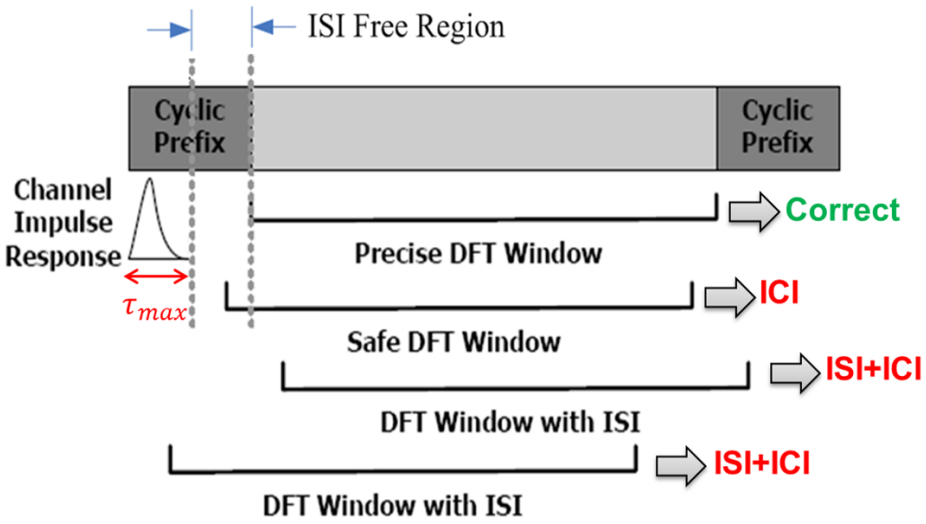

Figure 4.1: Four different cases of OFDM symbol starting point subject to STO

In the case of safe DFT window a single tap frequency domain equalizer can solve the problem as there is no ISI. But in our case since we are not using any channel estimation and compensation methods, even this will create a problem if the resulting phase shift between adjacent OFDM symbols is more than $\pm 45^0$ as we are using Differential QPSK modulation.

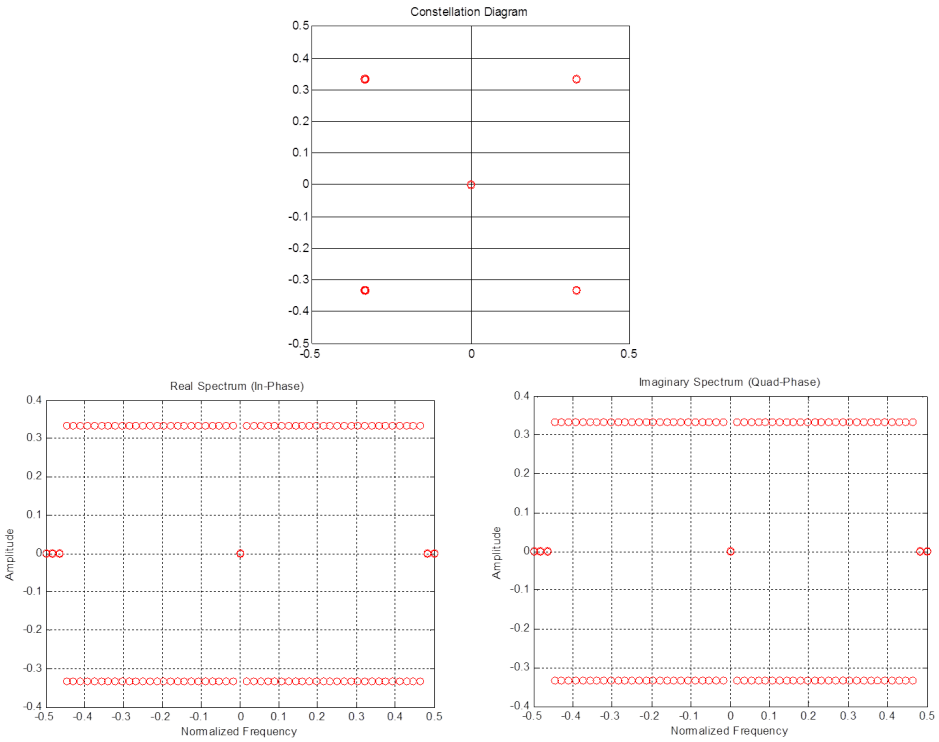

Figure 4.2: Constellation, Real and Imaginary Spectrum for STO=0

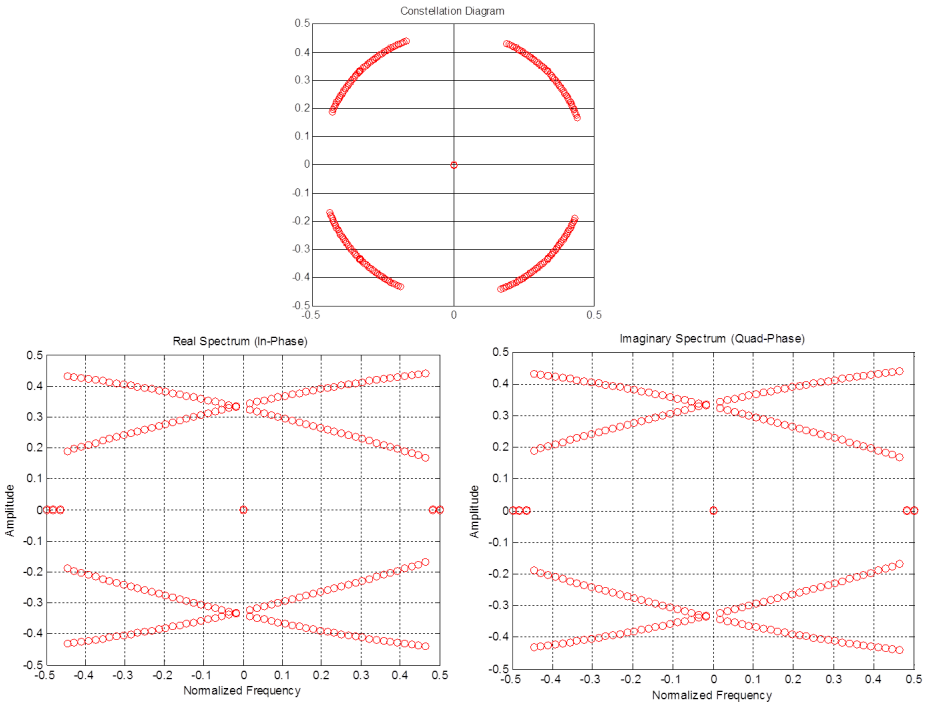

Figure 4.3: Constellation, Real and Imaginary Spectrum for STO=30%

4.2 Effect of Non-Uniform Doppler / Sampling skew

We have seen in the last chapter that the effect of Doppler in wideband OFDM is that each sub-carrier experiences a Doppler shift $e^{j2\pi a f_k t}$, which depends on the frequency of the sub-carrier. This is illustrated in Fig. 4.4 through Fig. 4.6 using a sparse OFDM symbol.

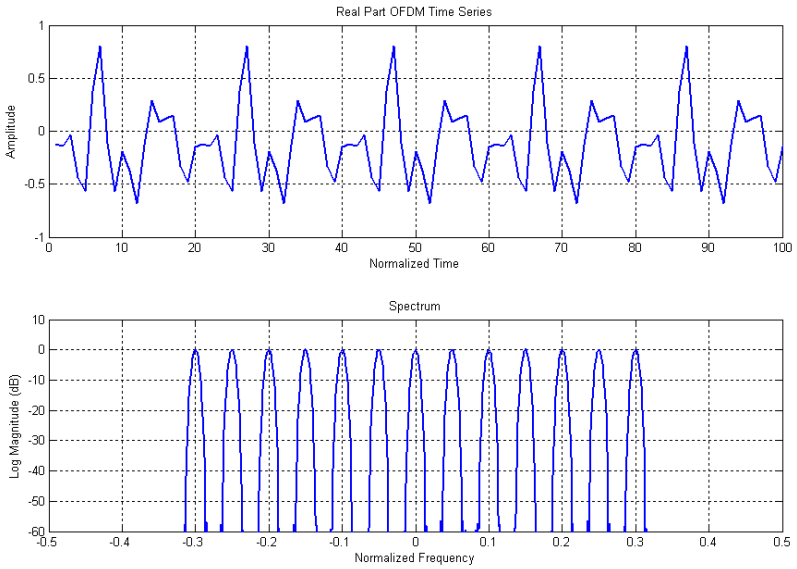

Figure 4.4: Time and Spectra of Sparse OFDM Symbol

For a wideband OFDM system the effect of Doppler and sampling skew are the same. It essentially causes scaling in time domain or non-uniform shift and spread in frequency domain. In the last chapter, we have shown mathematically that resampling converts non-uniform Doppler shift to uniform Doppler shift, and hence a wideband problem to narrowband problem. Once this is achieved we can use standard CFO compensation techniques applicable to conventional narrowband RF systems.

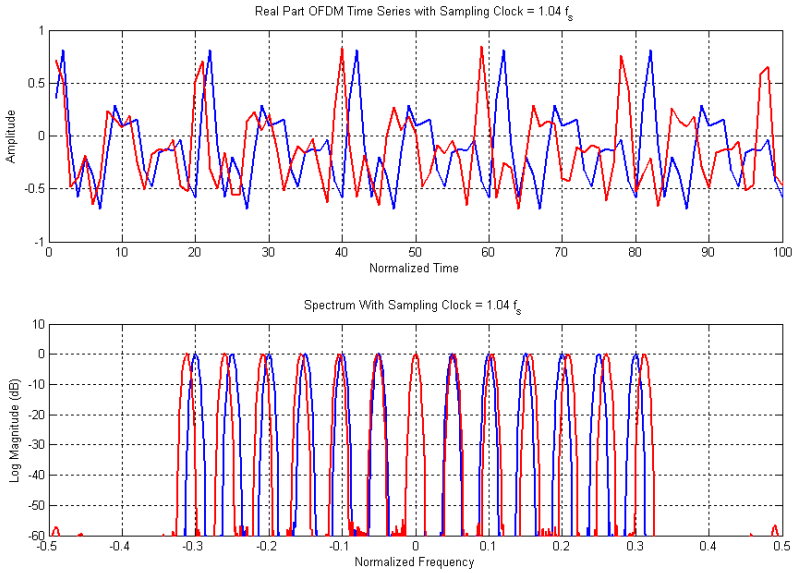

Figure 4.5: Time and Spectra with Doppler Time Scale /Sampling skew $= 1.04 f_s$

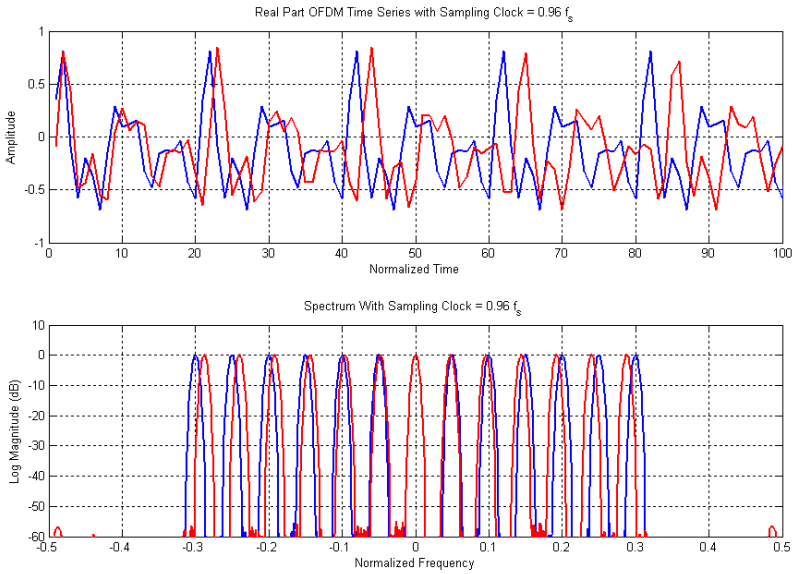

Figure 4.6: Time and Spectra with Doppler Time Scale /Sampling skew $= 0.96 f_s$

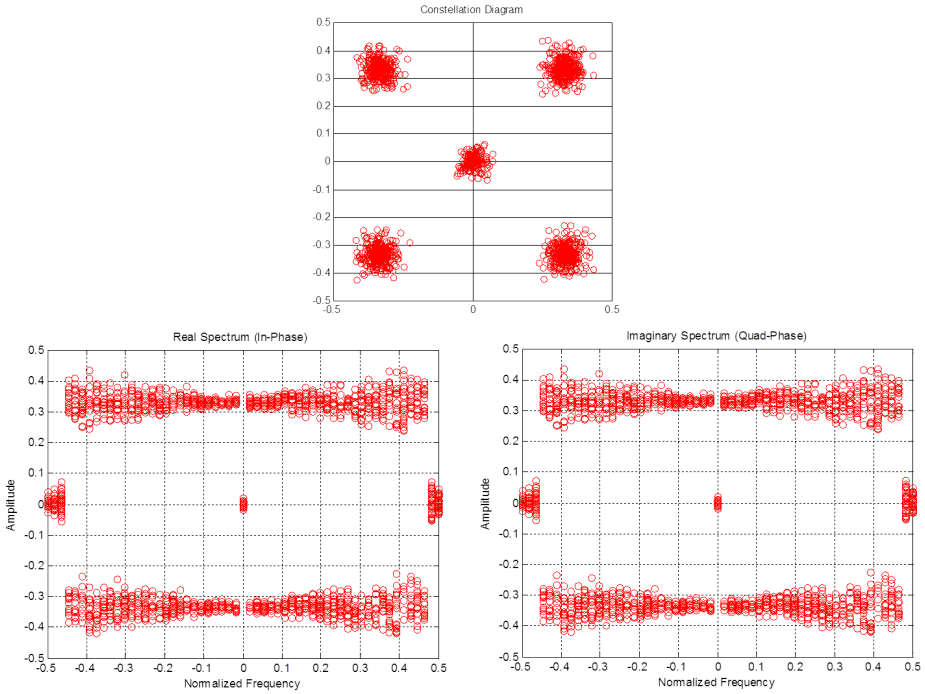

Figure 4.7: Constellation, Real and Imaginary Spectrum for Doppler Time Scale /Sampling skew of 5% of Sampling Time Period per Symbol

4.3 Effect of Uniform Doppler / Carrier Frequency Offset

Let us define the normalized CFO, ϵ, as a ratio of the CFO to sub-carrier spacing Δf, shown as

$$\epsilon = \frac{f_{offset}}{\Delta f} \tag{4.2}$$

Let ϵ_i and ϵ_f denote the integer part and fractional part of ϵ, respectively, and therefore, $\epsilon = \epsilon_i + \epsilon_f$, where $\epsilon_i = \lfloor \epsilon \rceil$. For the time-domain signal $x[n]$, a CFO of ϵ causes a phase offset of $2\pi n\epsilon$, that is, proportional to the CFO ϵ and time index n. Note that it is equivalent to a frequency shift of $-\epsilon$ on the frequency-domain signal $X[k]$. For the transmitted signal $x[n]$, the effect of CFO ϵ on the received signal $y[n]$ is summarized in Table 4.2.

Fig. 4.8 shows that the frequency shift of $\epsilon = \epsilon_i + \epsilon_f$ in the frequency-domain signal $X[k]$ subjects to the CFO of ϵ and leads to an inter-carrier interference (ICI), which means a sub-carrier frequency component is affected by other sub-carrier frequency

Table 4.2: The effect of CFO on the received signal.

	Received signal	Effect of CFO ε on the received signal
Time-domain signal	$y[n]$	$e^{j2\pi n\varepsilon/N}x[n]$
Frequency-domain signal	$Y[k]$	$X[k-\varepsilon]$

components.

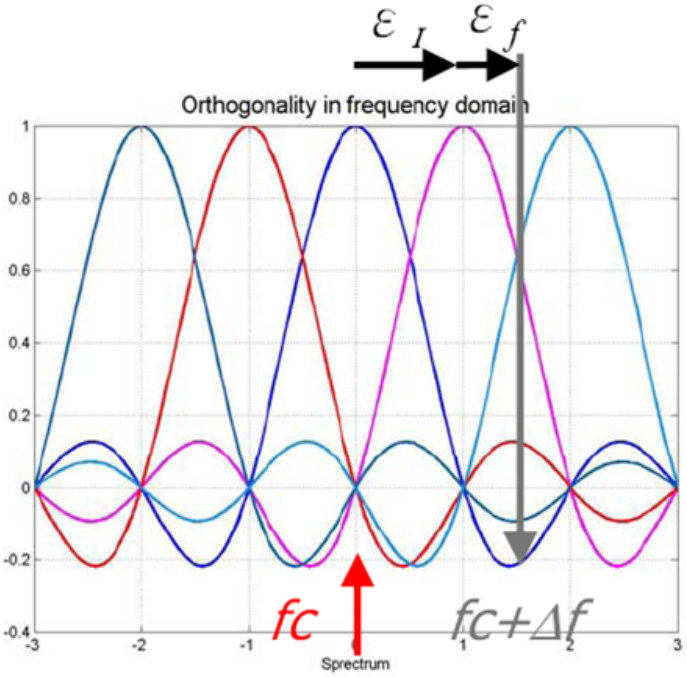

Figure 4.8: Inter-carrier interference (ICI) subject to CFO.

From (4.1), the time-domain received signal can be written as

$$y_l[n] = \frac{1}{N}\sum_{k=0}^{N-1} H[k]X_l[k]e^{j2\pi(k+\epsilon)n/N} + z_l[n] \tag{4.3}$$

The effect of CFO =0.1bin width in time domain and frequency domain for a sparse OFDM is shown in the Fig. 4.9

The Constellation, Real and Imaginary Spectrum for CFO = 0.1Bin is shown in the Fig. 4.10

The impact of frequency offset resulting in Inter Carrier Interference (ICI) while receiving an OFDM modulated symbol is shown in the Fig. 4.11.

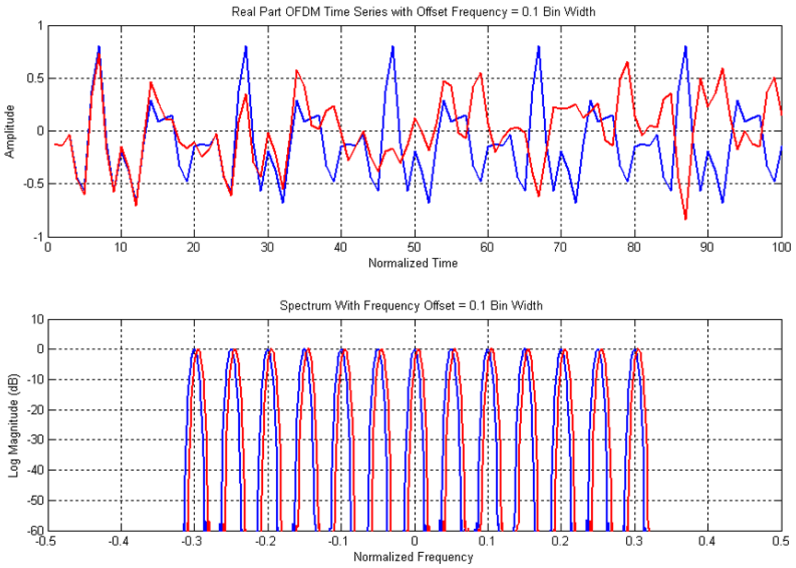

Figure 4.9: Time and Spectra With CFO = 0.1 Bin

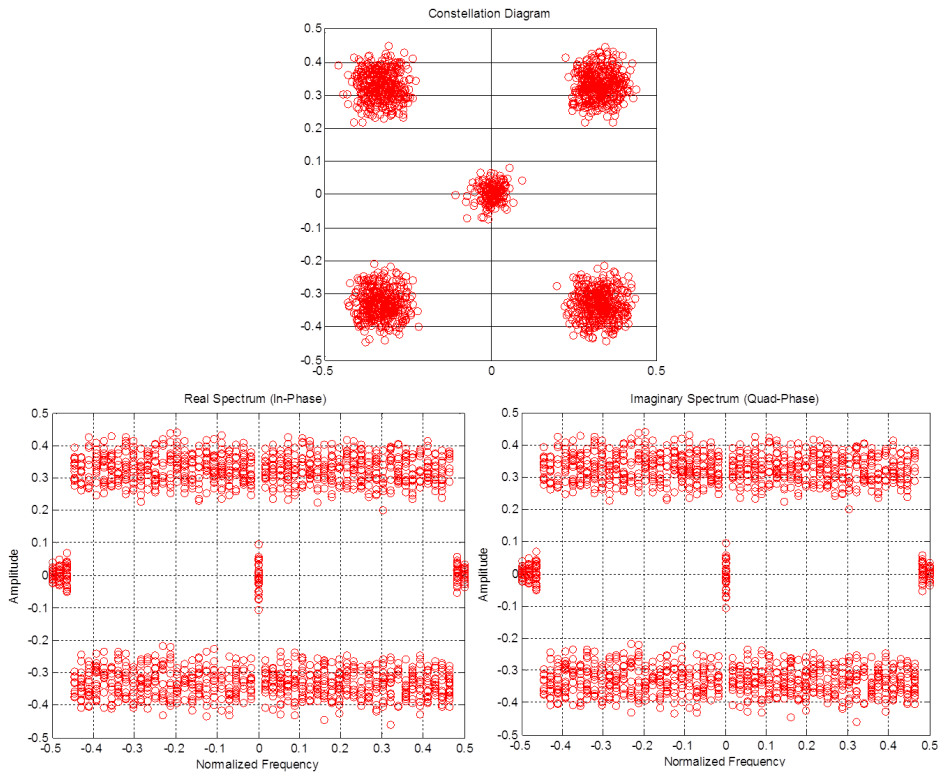

Figure 4.10: Constellation, Real and Imaginary Spectrum for CFO = 0.1Bin

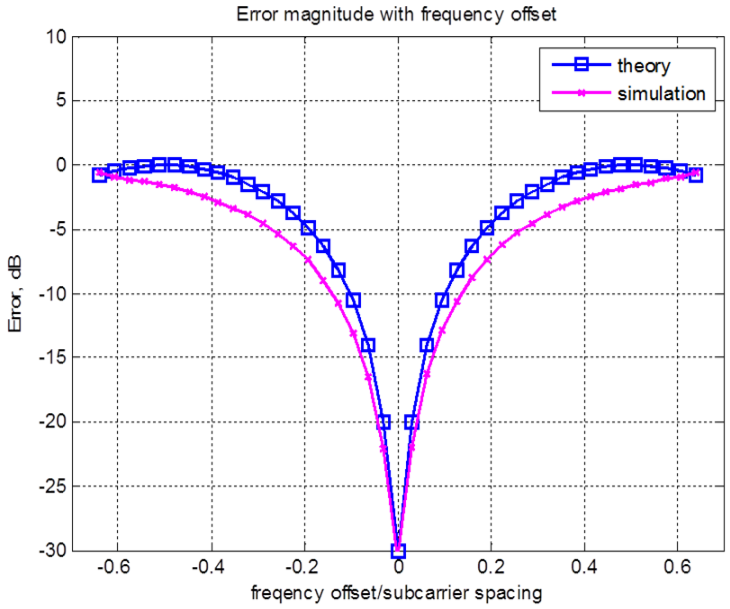

Figure 4.11: Error Magnitude vs. frequency offset for OFDM

Impact CFO on BER in AWGN and Rayleigh fading channel are shown in Fig. 4.12 and Fig. 4.13

4.4 Estimation Techniques for CFO

The frequency synchronization algorithms in OFDM systems can preliminary can be classified as follows:

- Processing domain: time or frequency
- Observation space: considering cyclic prefix or not
- Level of data-assistance: preamble-aided or pilot-aided

For WLAN applications, pilot, preamble and cyclic prefix are used. The preamble and pilot allow the receiver to use efficient maximum likelihood algorithms to estimate and correct the frequency offset.

4.4.1 Time-Domain Estimation Techniques for CFO

Frequency Offset in the time domain can be estimated by measuring phase slope i.e., Change in Phase of a complex periodic time signal in a specified time interval as shown

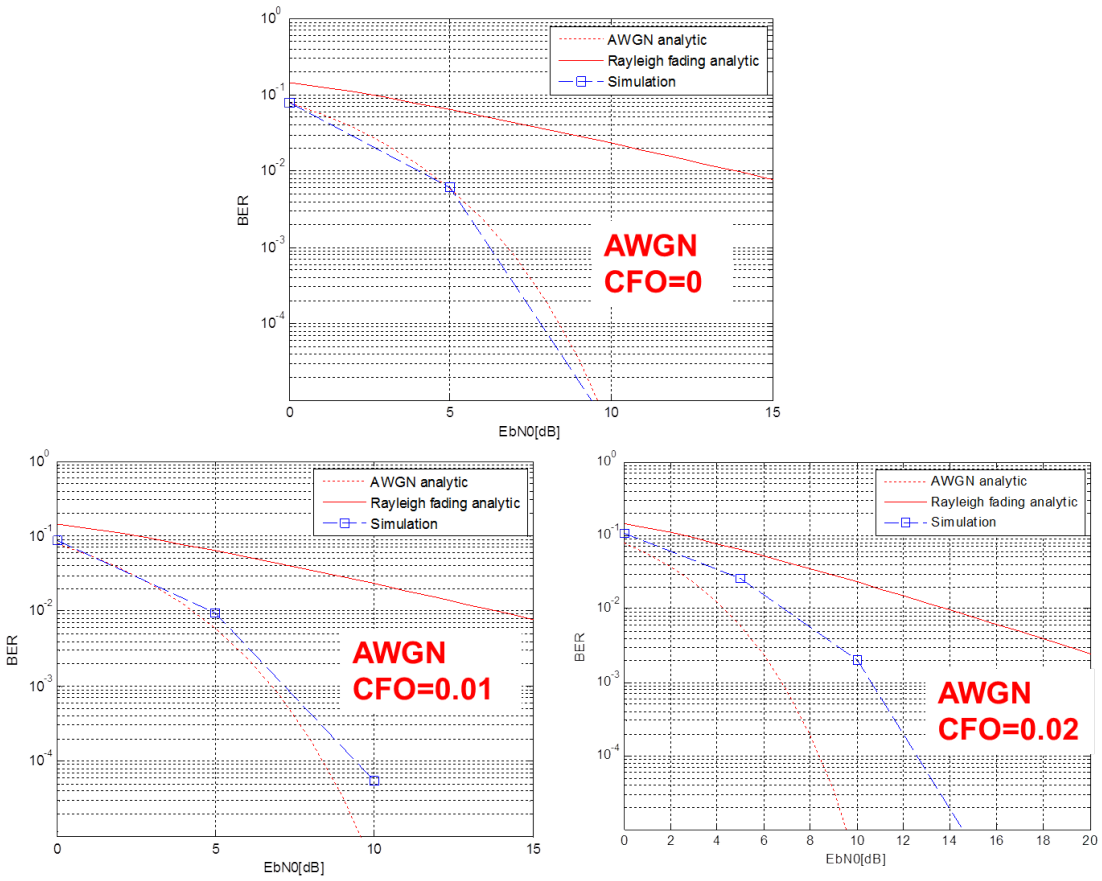

Figure 4.12: Impact CFO on BER in AWGN channel

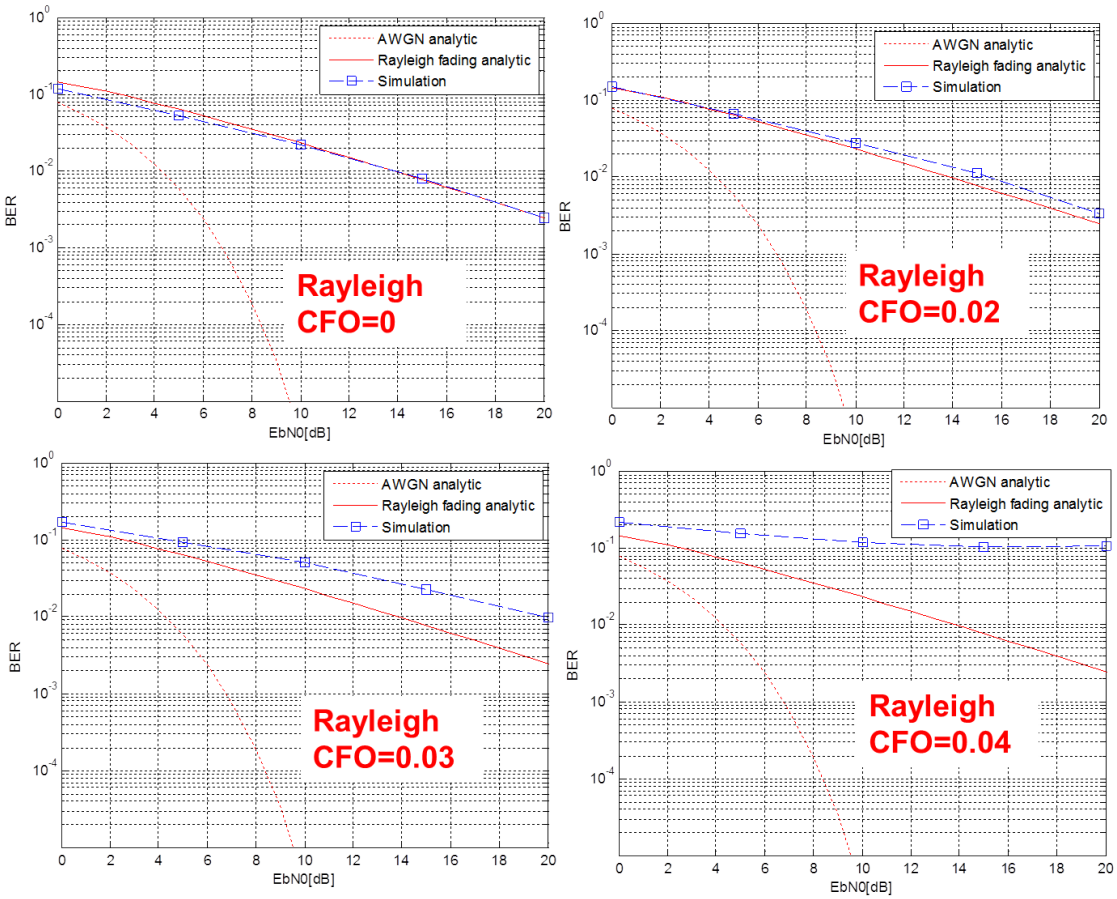

Figure 4.13: Impact CFO on BER in Rayleigh fading channel

in Fig. C.1

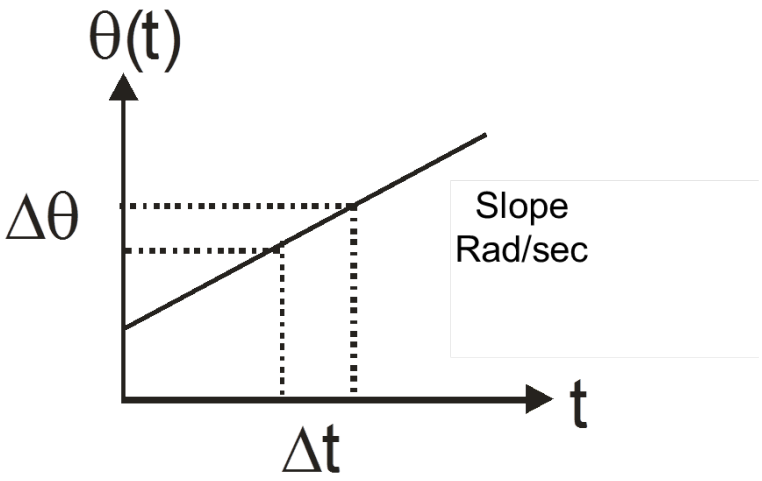

Figure 4.14: Measuring Frequency Offset in the time Domain

For CFO estimation in the time domain, cyclic prefix (CP) or training symbol is used. Each of these techniques is described as below.

CFO Estimation Techniques Using Cyclic Prefix (CP) in Time Domain

With perfect symbol synchronization, a CFO of ϵ results in a phase rotation of $2\pi n\epsilon/N$ in the received signal. Under the assumption of negligible channel effect, the phase difference between CP and the corresponding rear part of an OFDM symbol (spaced N samples apart) caused by CFO is $2\pi N\epsilon/N = 2\pi\epsilon$ Then, the CFO can be found from the phase angle of the product of CP and the corresponding rear part of an OFDM symbol.

$$\hat{\epsilon} = \frac{1}{2\pi} arg\left\{y_l^*[n] y_l[n+N]\right\}, \quad n = -1, -2, \cdots - N_g. \tag{4.4}$$

In order to reduce the noise effect, its average can be taken over the samples in a CP interval as

$$\hat{\epsilon} = \frac{1}{2\pi} arg\left\{\sum_{n=-N_g}^{-1} y_l^*[n] y_l[n+N]\right\}, \quad n = -1, -2, \cdots - N_g. \tag{4.5}$$

Since the argument operation $arg()$ is performed by using $tan^{-1}()$, the range of CFO estimation is $[-\pi, +\pi)/2\pi = [-0.5, +0.5)$ so that $|\hat{\epsilon}| < 0.5$ and consequently, integral CFO cannot be estimated by this technique.

Note that $y_l^*[n]y_l[n+N]$ becomes real only when there is no frequency offset. This implies that it becomes imaginary as long as the CFO exists. In fact, the imaginary part of $y_l^*[n]y_l[n+N]$ can be used for CFO estimation In this case, the estimation error is defined as

$$e_\epsilon = \frac{1}{L}\sum_{n=1}^{L} Im\left\{y_l^*[n]y_l[n+N]\right\} \tag{4.6}$$

where L denotes the number of samples used for averaging. Note that the expectation of the error function in eqn. (4.6) can be approximated as

$$E\left\{e_\epsilon\right\} = \frac{\sigma_d^2}{N} sin\left(\frac{2\pi\epsilon}{N}\right) \sum_{k\ correspond\ to\ useful\ carriers}^{L} |H_k|^2 \approx K\epsilon \tag{4.7}$$

where σ^2 is the transmitted signal power, H_k is the channel frequency response of the k^{th} subcarrier, and K is a term that comprises transmit and channel power. Frequency synchronization can be maintained by controlling VCO in accordance with the sine function shown in Fig. 4.15

$$|\hat{\epsilon}| < 0.5 \tag{4.8}$$

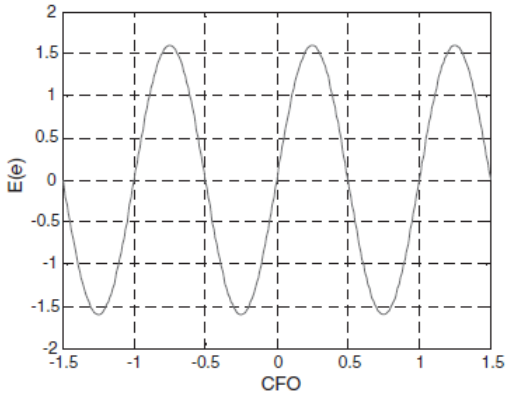

Figure 4.15: S-curve around the origin

CFO Estimation Techniques Using Training Symbol in Time Domain

The range of CFO estimation can be increased by reducing the distance between two blocks of samples for correlation. Let D be an integer that represents the ratio of the

OFDM symbol length to the length of a repetitive pattern. Let a transmitter send the training symbols with D repetitive patterns in the time domain, which can be generated by taking the IFFT of a comb-type signal in the frequency domain given as

$$x_l[k] = \begin{cases} A_m, & \text{if } k = D.i, \quad i = 0, 1, \cdots, (N/D - 1) \\ 0 & \text{otherwise} \end{cases} \tag{4.9}$$

where A_m represents an M-ary symbol and N/D is an integer. As $x_l[n]$ and $x_l[n+N/D]$ are identical (i.e., $y_l*[n]y_l[n+N/D] = |y_l[n]|^2 e^{j\pi\epsilon}$ a receiver can make CFO estimation as

$$\hat{\epsilon} = \frac{D}{2\pi} arg \left\{ \sum_{n=0}^{N/D-1} y_l^*[n] y_l[n + N/D] \right\} \tag{4.10}$$

The CFO estimation range covered by this technique is $\{|\epsilon| \leq D/2\}$,which becomes wider as D increases. Note that the number of samples for the computation of correlation is reduced by $1/D$, which may degrade the MSE performance. In other words, the increase in estimation range is obtained at the sacrifice of MSE (mean square error) performance. Fig. 4.16 shows the estimation range of CFO vs. MSE performance for $D = 1$ and 4. Here, a trade-off relationship between the MSE performance and estimation range of CFO is clearly shown. As the estimation range of CFO increases, the MSE performance becomes worse.

By taking the average of the estimates with the repetitive patterns of the shorter period as

$$\hat{\epsilon} = \frac{D}{2\pi} arg \left\{ \sum_{m=0}^{D-2} \sum_{n=0}^{N/D-1} y_l^*[n + mN/D] y_l[n + (m+1)N/D] \right\} \tag{4.11}$$

the MSE performance can be improved without reducing the estimation range of CFO.

As an example, in IEEE 802.11a system, the carrier frequency is approximately 5.3GHz, standard specifies a maximum oscillator error of 20 parts per million (ppm). Thus, with opposite signs, the amounts to a frequency error of $f_\Delta = 40 \times 10^{-6} \times 5.3 \times$

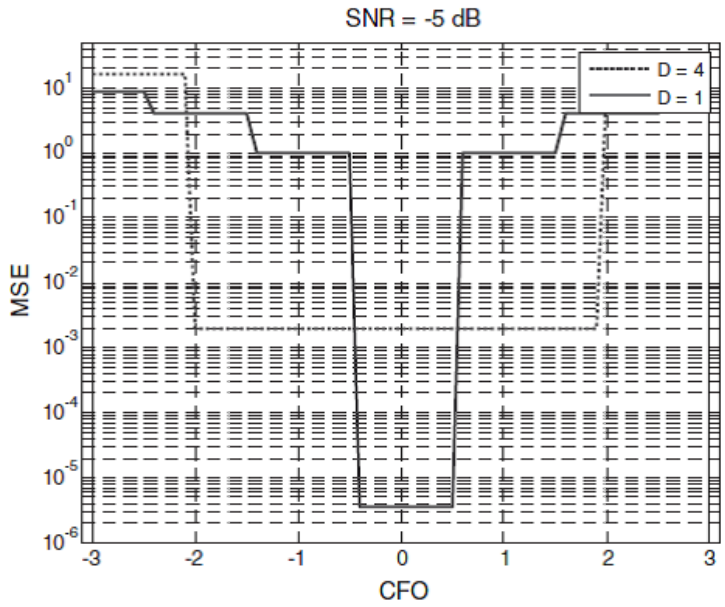

Figure 4.16: Estimation range of CFO vs. MSE performance.

$10^9 = 212kHz$. Now consider the long training symbols. The delay is $D = 64$.

$$f_\Delta = \frac{1}{2\pi DT_s} = 156.25kHz \tag{4.12}$$

Observe that this is less than the maximum possible error defined in the standard. Thus this estimator would not be reliable if only the long training symbols are used. In the IEEE 802.11a short training symbols are also specified with the sample time of 50ns and the delay $D = 16$ (which is 4 times shorter), Thus the maximum frequency error that can be estimated is

$$f_\Delta = \frac{1}{2\pi DT_s} = 625kHz \tag{4.13}$$

Now the max possible frequency error is well within the range of the algorithm. IEEE 802.11a suggests a **two-step** frequency estimation process with a **coarse** frequency estimate performed from the short training symbols and a **fine** frequency synchronization from the long training symbols.

4.4.2 Frequency-Domain Estimation Techniques for CFO

Preamble based Method/Moose Method

If two identical training symbols are transmitted consecutively, the corresponding signals with CFO of ϵ are related with each other as follows:

$$y_2[n] = y_1[n]e^{j2\pi N\epsilon/N} \leftrightarrow Y_2[k] = Y_1[k]e^{j2\pi\epsilon} \tag{4.14}$$

Using the relationship in(4.14), the CFO can be estimated as

$$\hat{\epsilon} = \frac{1}{2\pi} tan^{-1} \left\{ \frac{\sum_{k=0}^{N-1} Im\left[Y_1^*[k]Y_2[k]\right]}{\sum_{k=0}^{N-1} Re\left[Y_1^*[k]Y_2[k]\right]} \right\} \tag{4.15}$$

which is a well-known approach (Moose, 1994).Although the range of CFO estimated by (4.15) is $|\epsilon| = \pi/2\pi = 1/2$, that is, $\pm 1/2$ the inter carrier-spacing. It can be increased D times by using a training symbol with D repetitive patterns. The repetitive patterns in the time-domain signal can be generated by (4.9). In this case, (4.15) is applied to the sub-carriers with non-zero value and then, averaged over the sub-carriers. As discussed in the previous subsection, the MSE performance may deteriorate due to the reduced number of non-zero samples taken for averaging in the frequency domain. Note that this particular CFO estimation technique requires a special period, usually known as a preamble period, in which the consecutive training symbols are provided for facilitating the computation in (4.15). In other words, it is only applicable during the preamble period, for which data symbols cannot be transmitted. As $\epsilon \rightarrow 0.5$, ϵ may, due to noise and the discontinuity of the arctangent, jump to -0.5. When this happens, in practice, the estimate becomes useless.

Pilot tones based/Classen's Maethod

We can think about another technique that allows for transmitting the data symbols while estimating the CFO. As proposed by (F. Classen and Meyr, 1994), pilot tones can be inserted in the frequency domain and transmitted in every OFDM symbol for CFO tracking. Figure 5.16 shows a structure of CFO estimation using pilot tones. First, two OFDM symbols, $y_l[n]$ and $y_{l+D}[n]$, are saved in the memory after synchronization.

Then, the signals are transformed into $\{Y_l[k]\}\,|_{k=0}^{N-1}$ and $\{Y_{l+D}[k]\}\,|_{k=0}^{N-1}$ via FFT, from which pilot tones are extracted. After estimating CFO from pilot tones in the frequency domain, the signal is compensated with the estimated CFO in the time domain. In this process, two different estimation modes for CFO estimation are implemented: acquisition and tracking modes. In the acquisition mode, a large range of CFO including an integer CFO is estimated. In the tracking mode, only fine CFO is estimated. The integer CFO is estimated by

$$\hat{\epsilon}_{acq} = \frac{1}{2\pi.T_{sub}} \max_{\epsilon} \left\{ \left| \sum_{j=0}^{L-1} Y_{l+D}\left[p[j],\epsilon\right] Y_l^*\left[p[j],\epsilon\right] X_{l+D}^*\left[p[j]\right] X_l\left[p[j]\right] \right| \right\} \tag{4.16}$$

where $L, p[j]$, and $X_l[p[j]]$ denote the number of pilot tones, the location of the j^{th} pilot tone, and the pilot tone located at $p[j]$ in the frequency domain at the l^{th} symbol period, respectively. Meanwhile, the fine CFO is estimated by

$$\hat{\epsilon}_f = \frac{1}{2\pi.T_{sub}D} \arg \left\{ \sum_{j=1}^{L-1} Y_{l+D}\left[p[j],\hat{\epsilon}_{acq}\right] Y_l^*\left[p[j],\hat{\epsilon}_{acq}\right] X_{l+D}^*\left[p[j]\right] X_l\left[p[j]\right] \right\} \tag{4.17}$$

In the acquisition mode, $\hat{\epsilon}_{acq}$ and $\hat{\epsilon}_f$ are estimated and then, the CFO is compensated by their sum. In the tracking mode, only $\hat{\epsilon}_f$ is estimated and then compensated. The block diagram is shown in the Fig. 4.17

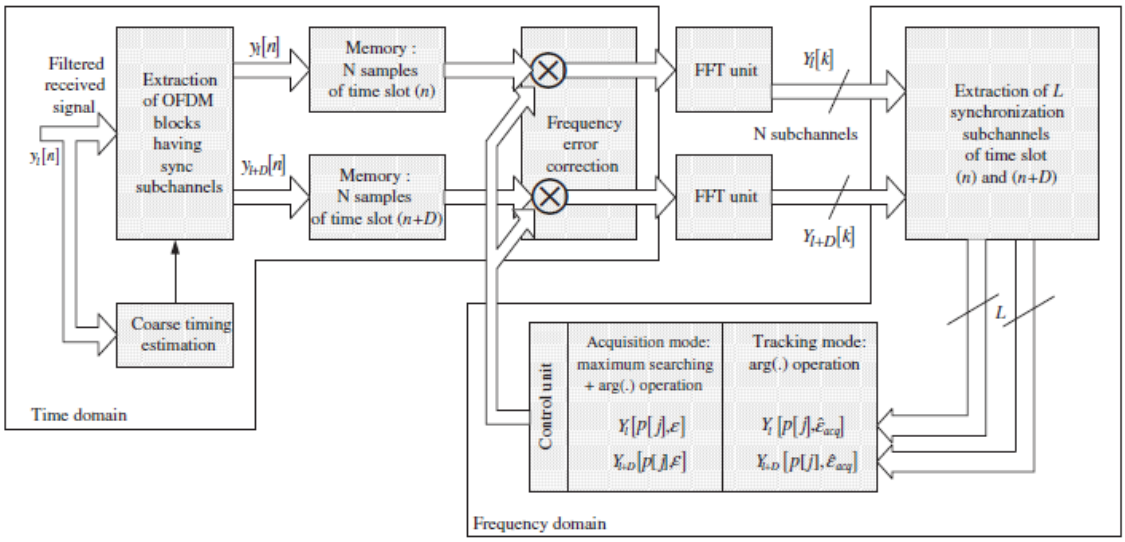

Figure 4.17: CFO synchronization scheme using pilot tones. *Adapted from (F. Classen and Meyr, 1994)*

The simulated results of MSE performance of all the three CFO estimation techniques described is shown in the Fig. 4.18

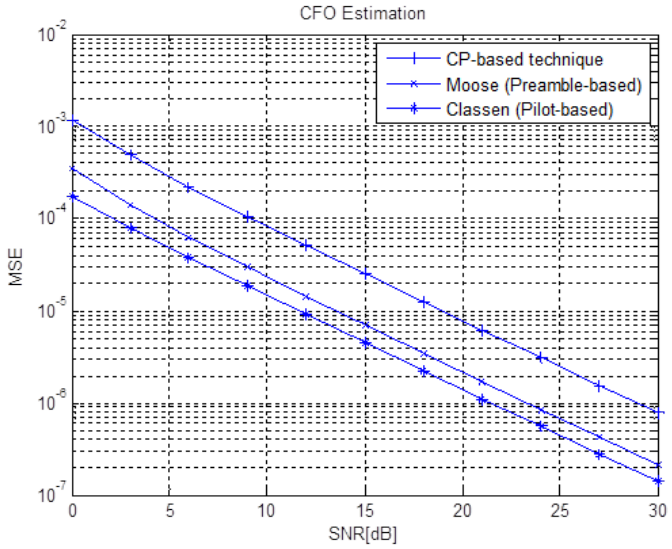

Figure 4.18: MSE of CFO estimation techniques (simulated)

CHAPTER 5

Differential Techniques to Combat Uncertainties in Phase and Phase Derivatives

For coherent detection, the path gains must be known at the receiver which is referred to in literature as Channel State Information at the Receiver (CSIR). In practice, the path gains are estimated at the receiver by transmitting pilot signals which causes reduction in the effective data rate. There will be mismatch between the path gains and their estimates and it is almost impractical to track the variations for very fast fading channels such as UWA channels. In differential detection, the decoder does not need channel estimation (no CSIR) and compensation. The transmitted symbols depend on each other and the decoder can detect from successive symbols. The single differential technique is tolerant to phase errors and double differential technique is tolerant to phase as well as frequency errors. Different Possible Options exist with Differential Detection as listed below.

1. Single Carrier Vs Multiple Carriers (OFDM)
2. Time Domain Vs Frequency Domain
3. Single Symbol Vs Multiple Symbols
4. Single Differential Vs Double Differential
5. Single Tx Antenna Vs Multiple Tx Antenna (Diff STBC)

Designer has to choose the best option for suitable for his application. The following sections in this chapter compare the theoretical and simulation results mostly available in literature. *The focus is not an in depth study of a specific result but to come up with a combination of results suitable for UWA channels*.

5.1 Single Carrier vs. Multi Carrier Modulation Schemes

From Table 1.2, the coherence bandwidth (delay spread) is seen to limit the number of symbols transmitted per second. Multi carrier modulation schemes such as OFDM

can effectively transform the frequency-selective fading channel into multiple parallel flat fading channels without requiring knowledge of channel gains at the transmitter. Depending upon the worst case delay spread encountered in the channel the length cyclic prefix/zero padding can be adjusted in OFDM-based systems. This approach is much simpler than single carrier modulation approaches with prohibitively complex adaptive equalization requirement for UWA channel.

5.2 Time Domain Differential OFDM vs. Frequency Domain Differential OFDM

In OFDM, differential modulations can be applied either in time domain (between successive OFDM symbols on the same sub carrier) or in frequency domain (between adjacent sub carriers in the same OFDM symbol). The idea is illustrated in Fig. 5.1

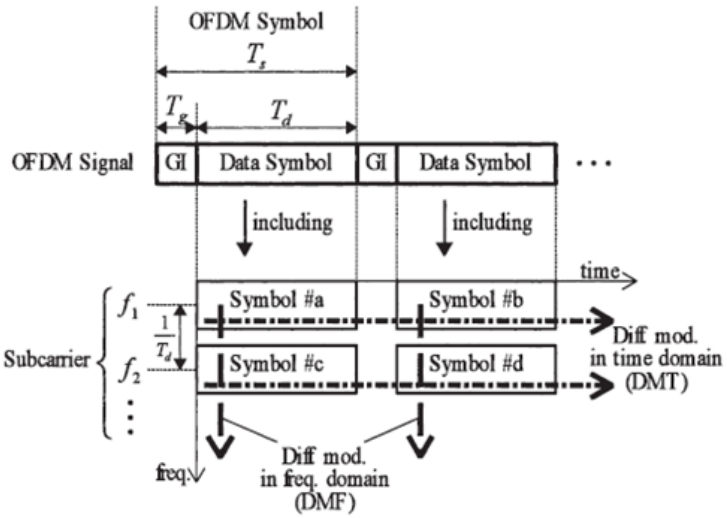

Figure 5.1: Time Domain Differential vs. Frequency Domain Differential OFDM

Referring to Fig. 5.2, if the fading is not frequency selective, then frequency domain differential OFDM performs well because of good coherence between sub carriers even under fast fading (high Doppler). Similarly, if the fading is not fast (low Doppler), time domain differential OFDM performs well because of good coherence between adjacent OFDM symbols, even under frequency selective fading (large RMS delay spread). So in the most general case, neither technique provides any benefit for underwater acoustic channels, because the fading phenomenon is both frequency selective and fast. How-

ever if the relative velocity between platforms is slow to moderate (low Doppler), time domain differential OFDM is a good choice as against coherent techniques.

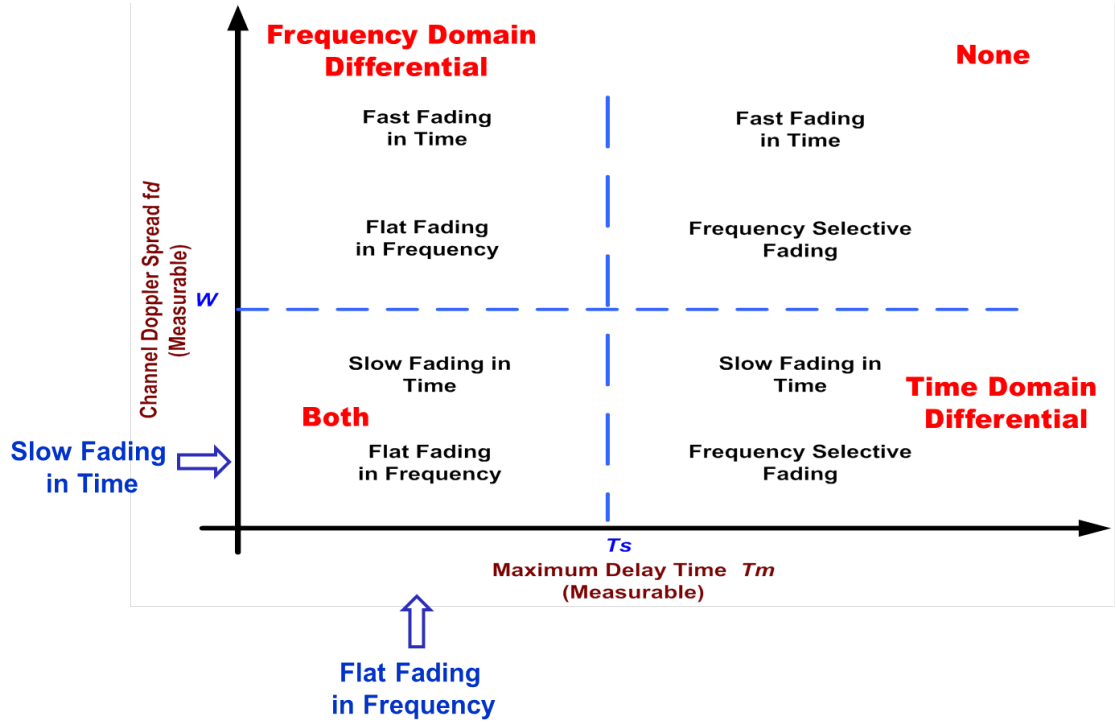

Figure 5.2: Explanation using four quadrant description

5.3 Single Symbol vs. Multiple Symbols

The figure shows the influence of frequency offset on the reception of OFDM/DQPSK signal using muti-bit Differential Detection algorithm, in an AWGN channel. From Fig. 5.3 we can see that system is less sensitive to frequency offset for smaller values of the number of bits that are compared during the detection (N_B), but the system has a better BER for larger values of parameter N_B.

5.4 Single Differential vs. Double Differential Schemes

In the previous section, we have seen that time domain differential technique is a good choice for UWA channels provided Doppler is low (slow fading). This is due to the well-known fact that DPSK/DQPSK eliminates the performance degradation due to phase differences between the carrier signal and the receiver's local reference signal if

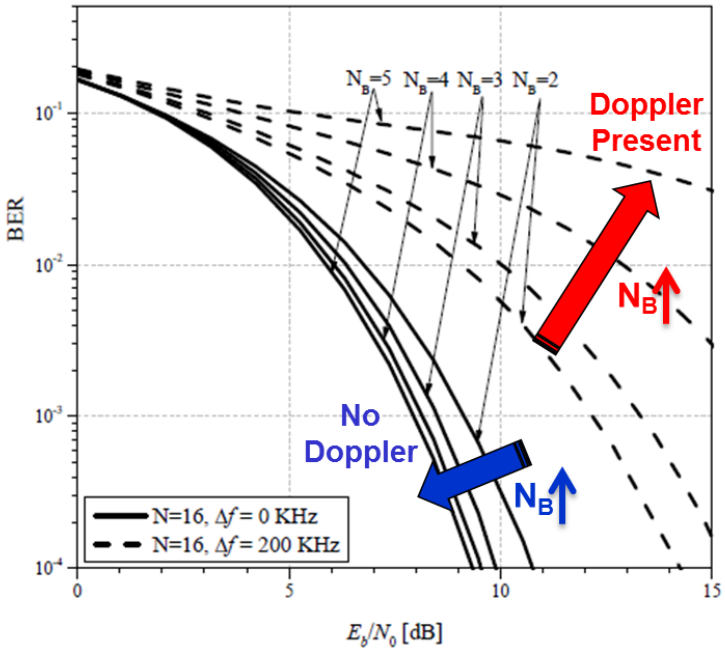

Figure 5.3: Influence of Frequency Offset on the Reception of OFDM/DQPSK Signal using Muti-Bit Differential Detection Algorithm [*Adapted from* (Bojan Dimitrijevic *et al.*, 2011)]

the differences are constant over two symbol intervals; however, it does not eliminate degradation due to frequency differences/offsets. In the late 1970's, several modulation schemes were proposed (Pent, 1978),(Okunev, 1979) that employed second-order differential encoding of the data, i.e., encoding the data into the signal phase as the difference of two adjacent phase angle differences, thereby requiring three symbol intervals for decoding. Such modulation schemes, together with second-order differentially coherent detection, can be shown to reduce the effects on performance degradation due to both phase and frequency differences when the differences are constant over three symbol intervals. Such systems were referred to by Pent (Pent, 1978) as "Doubly Differential PSK (DDPSK)." This modulation technique was first introduced in Russian literature for high Doppler, Low Earth Orbit (LEO) satellite communication applications. The block diagram of DDPSK Encoder and Detector is given in the Fig. 5.4.

The error probability for DDPSK as a function of signal energy-to-noise ratio (E/N_0)

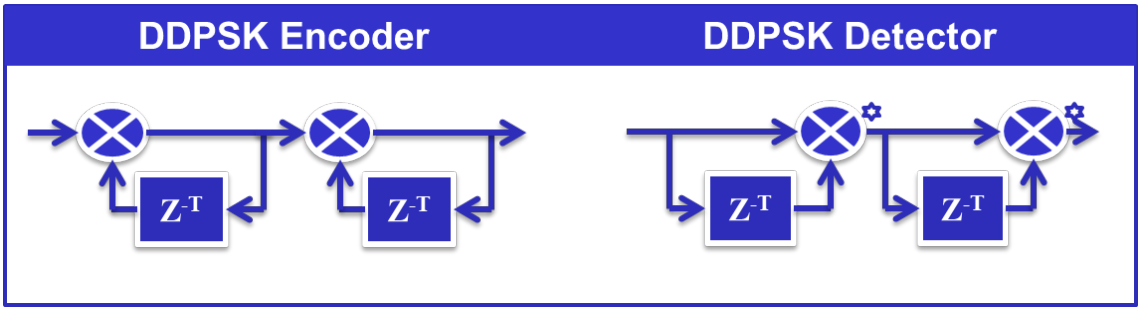

Figure 5.4: The block diagram of DDPSK Encoder and Detector

is given in below (van Alphen and Lindsey, 1994)

$$P_{DDPSK}(E') = \frac{1}{2} - \frac{E'}{2\pi N_0}\int_0^{\pi}\int_0^{\pi} erf\left(\sqrt{\frac{E'}{N_0}cos(2\eta_2 - \eta_1)}\right) .erf\left(\frac{E'}{N_0}cos\eta_2\right) cos\eta_1 cos\eta_2 .exp\left(\frac{E'[sin^2\eta_1 + sin^2\eta_2]}{-N_0}\right) d\eta_1 d\eta_2 \tag{5.1}$$

In Fig. 5.5 we plot the error probability given in (5.1) as a function of signal energy-to-noise ratio (E/N_0) for the special case of no frequency difference between the carrier signal and the receiver's local reference signal. i.e.,

$$\omega_d T = 0 \implies E' = E.\left(\frac{sin(\omega_d T/2)}{\omega_d T/2}\right)^2 = E \tag{5.2}$$

For the purpose of comparison, we also plot the probability of error for classical Binary Phase Shift Key (BPSK) and first-order binary Differentially Coherent Phase Shift Key (DPSK) assuming no frequency difference which are given by the following expressions.

$$P_{BPSK}(E) = \frac{1}{2}erfc\left(\sqrt{\frac{E}{N_0}}\right) \tag{5.3}$$

$$P_{DPSK}(E) = \frac{1}{2}exp\left(-\frac{E}{N_0}\right) \tag{5.4}$$

In Fig. 5.6 we plot the error probability given by (5.1) for binary DDPSK and the

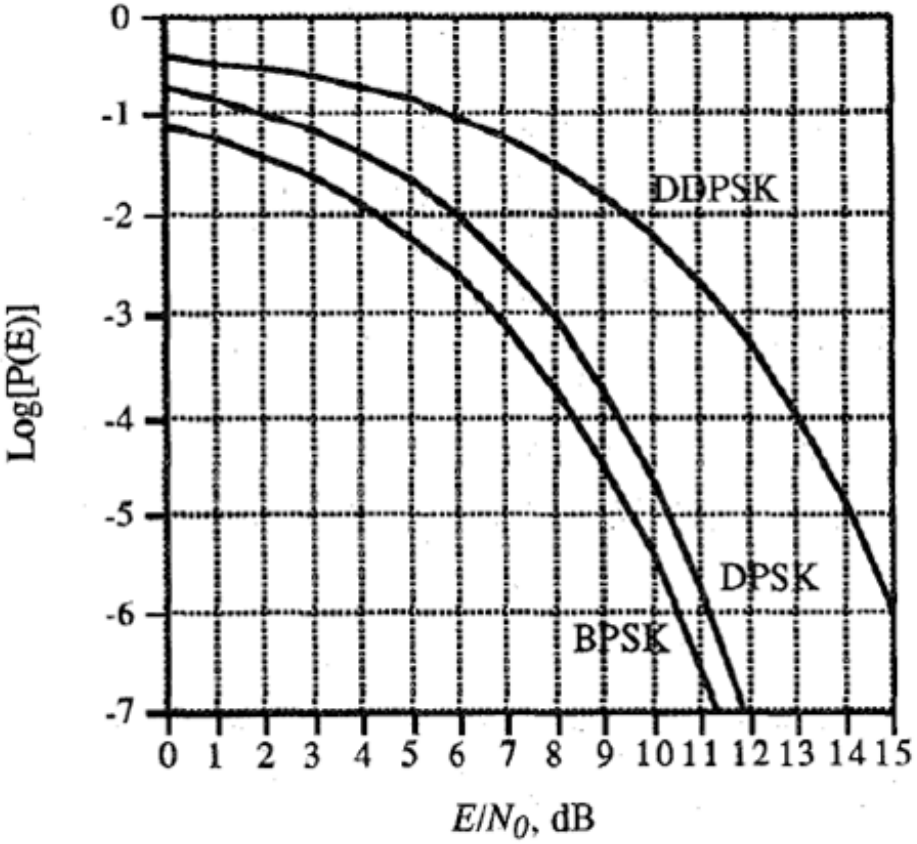

Figure 5.5: Performance Curves for Binary Modulation Techniques ($f_dT = 0$) [*Adapted from* (van Alphen and Lindsey, 1994)]

probability of error for binary DPSK with various frequency difference. i.e., when

$$\omega_d T \neq 0 \implies E' = E.\left(\frac{sin(\omega_d T/2)}{\omega_d T/2}\right)^2 \tag{5.5}$$

The error probability for DPSK as a function of signal energy-to-noise ratio (E/N_0) is given in below (van Alphen and Lindsey, 1994)

$$P_{DPSK}(E') = \frac{1}{2} - \frac{1}{2}\sqrt{\frac{E'}{\pi N_0}} \times \int_0^{\pi} \left[erf\left(\sqrt{\frac{E'}{N_0}cos(\eta - \omega_d T)}\right)\right] cos\eta \; exp\left(-\frac{E'}{N_0}sin^2\eta\right) d\eta \tag{5.6}$$

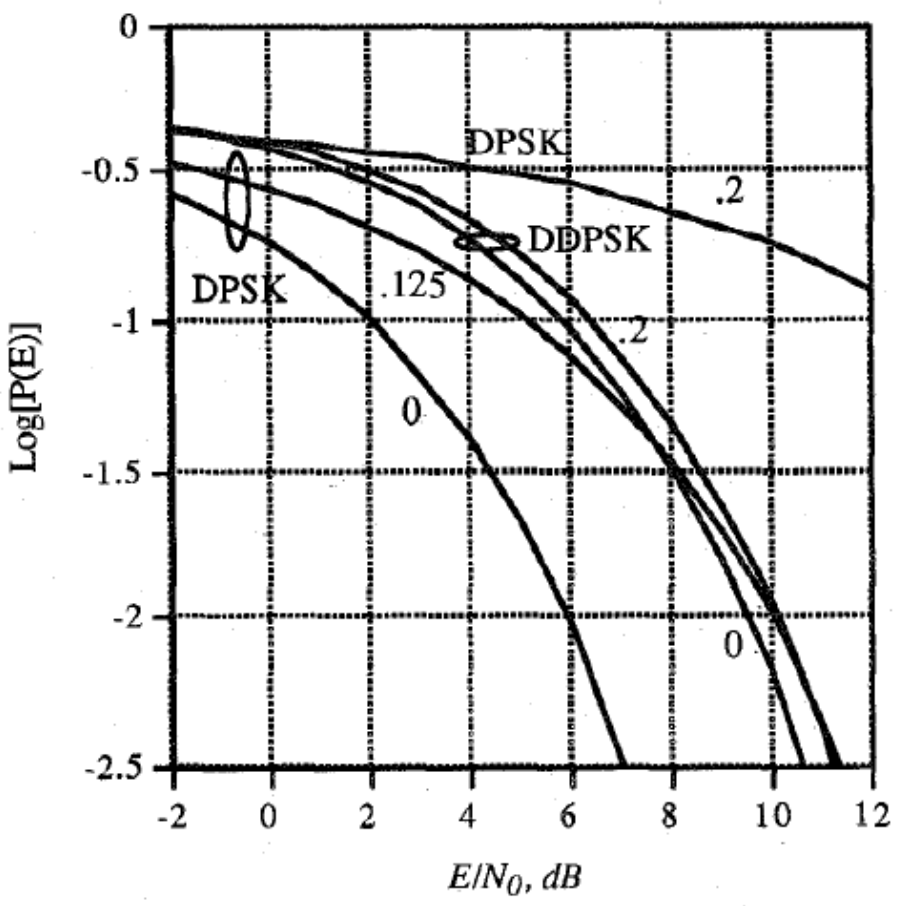

Figure 5.6: Performance Curves: Binary DDPSK Vs. Binary DPSK with Normalized Frequency Offsets $f_d T$ [*Adapted from* (van Alphen and Lindsey, 1994)]

It has been shown (M. Simon and Divsalar, 1992) that a 2dB SNR advantage over classical DDPSK can be obtained by choosing a delay of $2T$ rather than T in the first stage of the encoder and the second stage of the decoder under AWGN scenario. This improvement in performance could understood by noting the difference in the noise

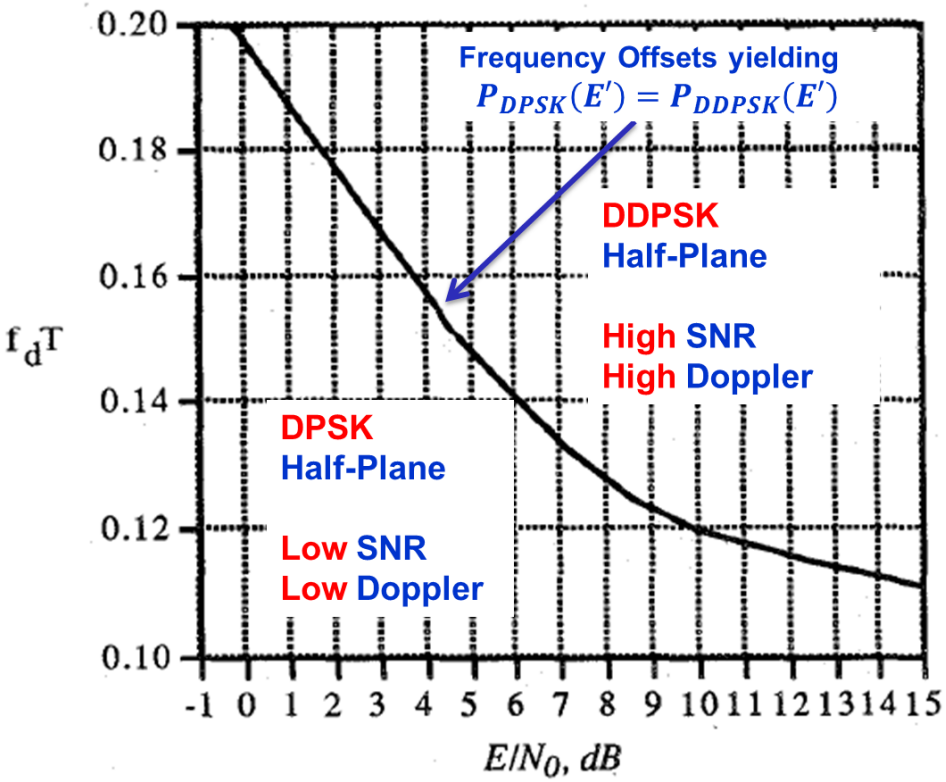

Figure 5.7: Frequency Offsets Yielding $P_{DPSK}(E') = P_{DDPSK}(E')$ [*Adapted from* (van Alphen and Lindsey, 1994)]

output in the two scenarios.

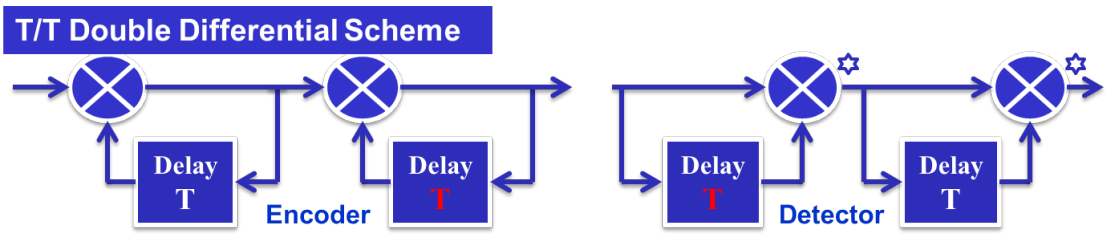

Figure 5.8: T/T Double Differential Scheme

The noise output of T/T scheme is given by $\eta(t) - 2\eta(t-T) + \eta(t-3T)$. The noise terms are repeated in this scheme.

The noise output of $T/2T$ scheme is given by $\eta(t) - \eta(t-T) - \eta(t-2T) + \eta(t-3T)$. The noise terms are NOT repeated in this scheme.

In the absence of frequency error, the exact performance binary DDPSK is given by (M. Simon and Divsalar, 1992)

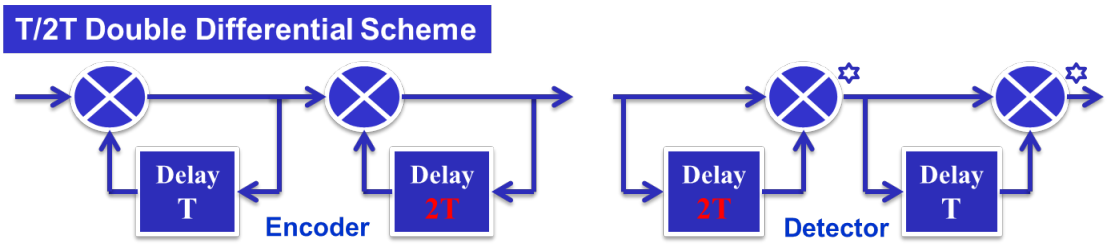

Figure 5.9: $T/2T$ Double Differential Scheme

For T/T Delay Combination:

$$\begin{aligned} P_E =& \frac{1}{2} - \frac{\sqrt{\pi}}{4}\left(\frac{E}{N_0}\right)^{3/2} exp\left(-\frac{3}{2}\frac{E}{N_0}\right) \\ & \times \sum_{m=0}^{\infty} \frac{(-1)^m}{2m+1}\left\{I_m\left(\frac{E}{2N_0}\right) + I_{m+1}\left(\frac{E}{2N_0}\right)\right\}^2 \\ & \times \left\{I_{2m+1/2}\left(\frac{E}{2N_0}\right) + I_{2m+1+1/2}\left(\frac{E}{2N_0}\right)\right\} \end{aligned} \tag{5.7}$$

For T/2T Delay Combination:

$$\begin{aligned} P_E =& \frac{1}{2} - \frac{\pi}{8}\left(\frac{E}{N_0}\right)^2 exp\left(-\frac{2E}{N_0}\right) \sum_{m=0}^{\infty} \frac{-1)^m}{2m+1} \\ & \times \left\{I_m\left(\frac{E}{2N_0}\right) + I_{m+1}\left(\frac{E}{2N_0}\right)\right\}^4 \end{aligned} \tag{5.8}$$

where $I_m(x.)$ is the modified Bessel function of the first kind of order m and argument x. P_E for both the cases are plotted in Fig. 5.10

A summary of Comparison of Time and Frequency Domain Single and Double Differential Schemes are given in the table Table 5.1 (Islam *et al.*, 2007)

5.5 Single Tx Antenna vs. Multiple Tx Antenna

Space-time codes such as Alamouti codes provide transmit diversity with only linear processing complexity at the receiver. Differential STBC schemes with two or more (H. Jafarkhani and Tarokh, 2001) transmit antennas have been proposed for flat fading channels. The advantage of differential schemes is that they do not require CSIR. (S.

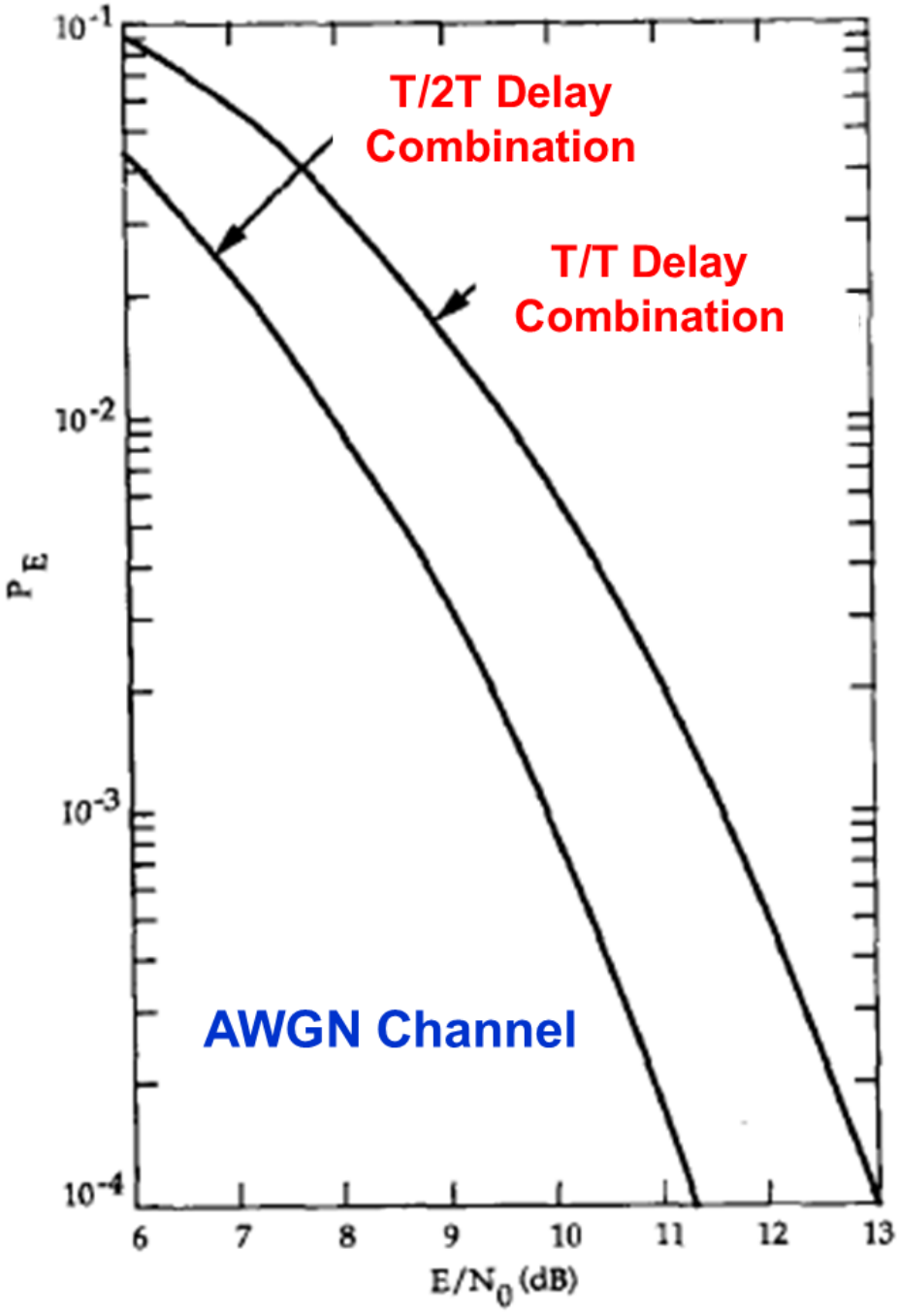

Figure 5.10: Advantage of T/2T Double Differential Scheme in AWGN [*Adapted from* (M. Simon and Divsalar, 1992)]

Table 5.1: Summary of Comparison of Time and Frequency Domain Single and Double Differential Schemes

	High/Low SNR	Low SNR	High SNR
	Low Doppler	High Doppler	High Doppler
Time Domain Single Differential	√	X	X
Frequency Domain Single Differential	X	√	X
Time Domain Double Differential (T/2T)	X	X	√
Frequency Domain Double Differential	Not useful		

N. Diggavi *et al.*, 2002) combines this form of differential coding with OFDM for signal transmission over frequency selective fading channels. Generalizing single-antenna double differential coding ideas to space-time context, Double Differential Space-Time Block Codes (DDSTBC) for Time-Selective Fading Channels have been developed (Zhiqiang Liu and Giannakis, 2001). DDSTBC can recover the information symbols with antenna diversity gains without estimating the channel at the receiver regardless of frequency offsets, hence is suitable for UWA applications.

CHAPTER 6

Conclusions and Future Works

6.1 Conclusions

An overview of the unique challenges in underwater acoustic (UWA) communication in ocean environment is presented. The UWA channel is compared with conventional RF channels. Several design considerations applicable to the physical layer design of a UWA communication system is described based on field measurements. The unique problems in synchronization under high Doppler are described highlighting the key differences in the way Doppler affects the RF and UWA channels.

A novel timing synchronization mechanism has been introduced in this study which caters for both the sampling skew offset and the Doppler shift between the transmitter and the receiver. The method is analysed under different scenarios both theoretically and by simulation. The trade-offs and performance bounds involved are clearly brought out.

A practical re-sampling filter with arbitrary re-sampling factor is designed and analysed its performance. Showed that re-sampling/rescaling in time essentially convert the wideband problem in to a narrowband problem. At this stage, conventional synchronization techniques applicable to narrowband OFDM systems have become relevant. Hence, a comparative study of such techniques available in literature has been carried out.

Doppler tolerant waveforms and modulation schemes are studied using analytical tools and simulation. Several unconventional techniques to combat uncertainties in Phase and Phase Derivatives are studies to further improve the robustness of the system.

In addition to simulation, the techniques are tried out in realistic environments with a Software Defined LabVIEW Test bed and with respect to the earlier field measurements carried at NPOL test facilities. Throughout the work, the focus was on the immediate

practical applicability of the techniques to improve the performance and robustness of the existing operational system.

6.2 Future Works

Owing to the absence of good statistical models for UWA channels, we have to resort to the field demonstration to completely validate the schemes that have emerged out. The system has to be tested under several channel conditions with different settings to build confidence. In addition to this, several channel sounding techniques mentioned in the thesis has to be carried out to better characterize the UWA channel. The transmit diversity schemes described using multiple transmit antennas has to be experimentally verified.

APPENDIX A

Software Defined LabVIEW Test bed for Acoustic OFDM

We have seen in Chapter 1 that unlike in a radio channel, where a number of models for both the probability distribution (e.g., Rayleigh fading) and the power spectral density of the fading process (e.g., the Jakes' model) are well accepted and even standardized, there is no consensus on statistical characterization of acoustic communication channels. Quoting Milica Stojanovic *"In the absence of good statistical models for simulation, experimental demonstration of candidate communication schemes remains a de facto standard"* (Stojanovic, 2009). A software defined LabVIEW testbed for Acoustic OFDM is developed and tested.The Transmitter and Receiver Algorithms were developed in National Instruments LabVIEW/ MathWorks MATLAB Software. NI USB DAQ is preferred instead of Laptop Sound card because of its better control and accuracy($\pm$100ppm max) of sampling frequency due to superior crystal used. The test-bed set-up is shown in the Fig. A.1

Figure A.1: The Test-bed Set-up

A snapshot of GUI at the transmitter and receiver are shown in Fig. A.2 and Fig. A.3 respectively.

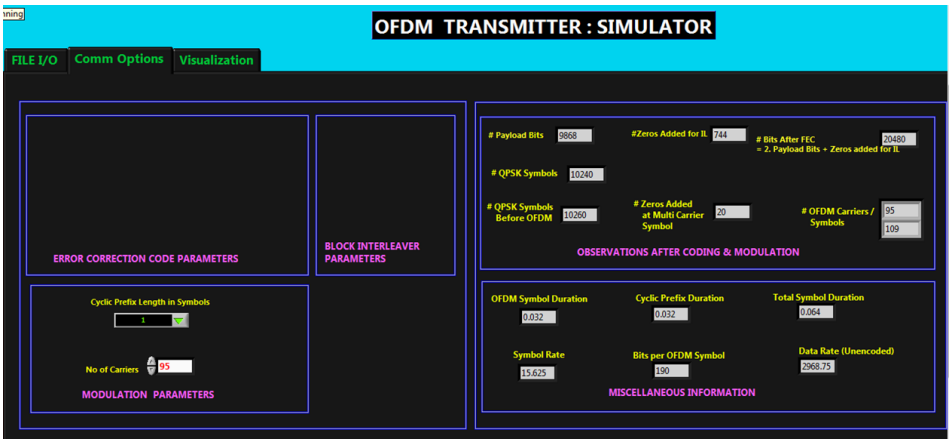

Figure A.2: GUI for Transmitter

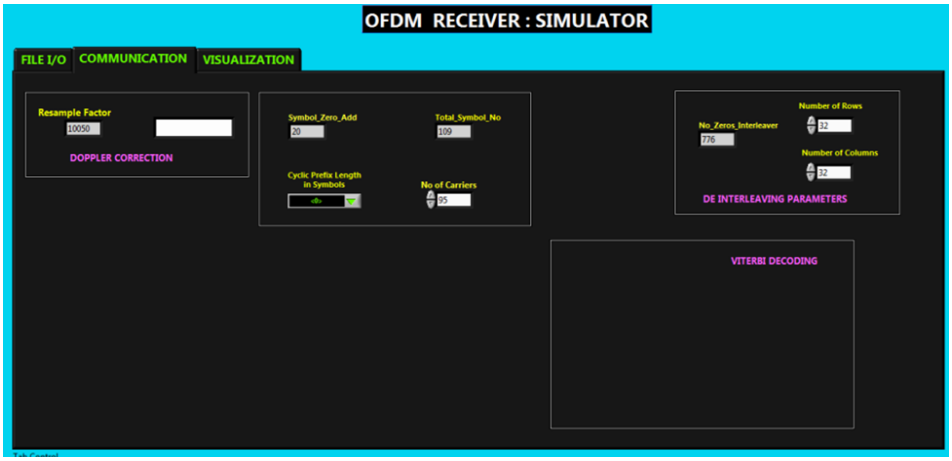

Figure A.3: GUI for Receiver

The real-time display showing the Time Series and Spectrogram of the received signal is shown in Fig. A.4. The initial chirp followed by OFDM signal receiving can be clearly seen in the display.

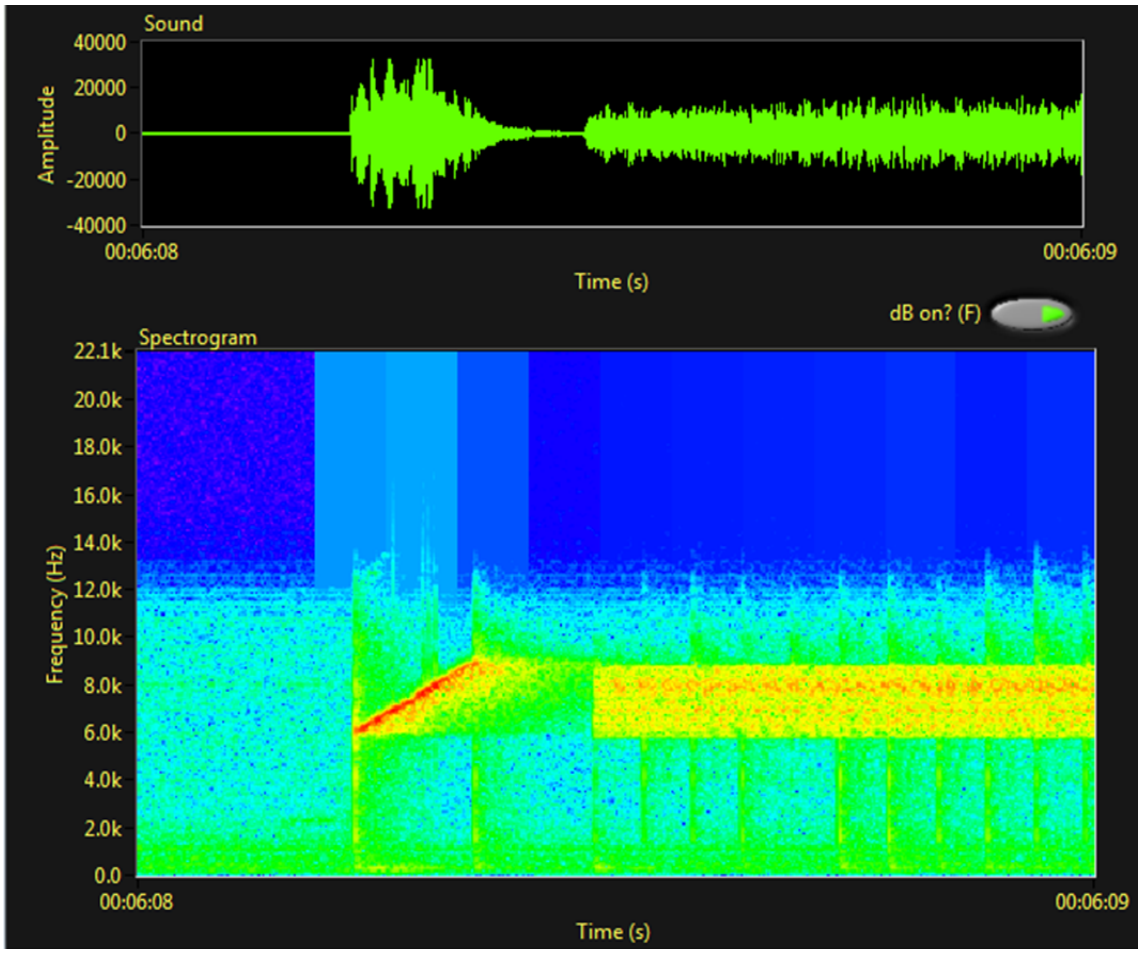

Figure A.4: Real-time Display Showing the Time Series and Spectrogram of the Received Signal.

The display showing the matched filter output crossing the detection threshold is shown in Fig. A.5. The red line is used to adjust the detection threshold at the Receiver.

The real-time Spectrum Analyzer at the receiver is shown in Fig. C.1

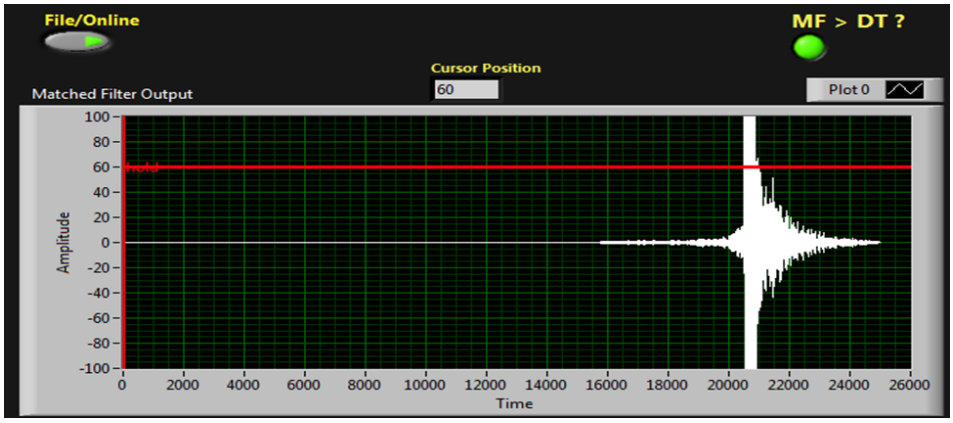

Figure A.5: Matched Filter output crossing the Detection Threshold.

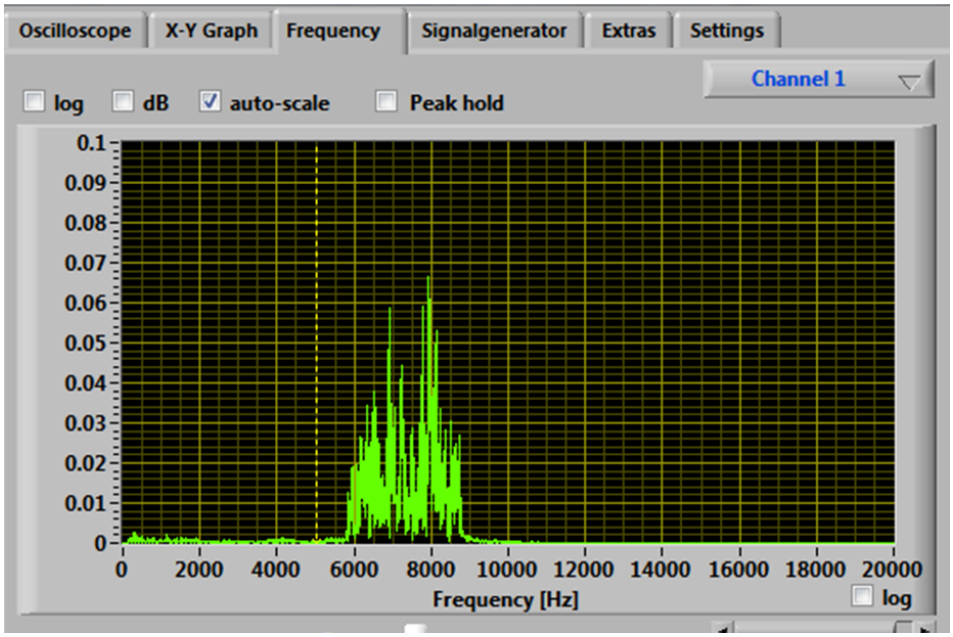

Figure A.6: The real-time Spectrum Analyzer at the receiver

APPENDIX B

Underwater Acoustics: Effects on Communication Systems Design

In this section, we discuss the effects of the ocean environment on the performance of underwater wireless communication systems. The aim of this section is to describe the various environmental factors that play a key role in the design of acoustic communication systems.

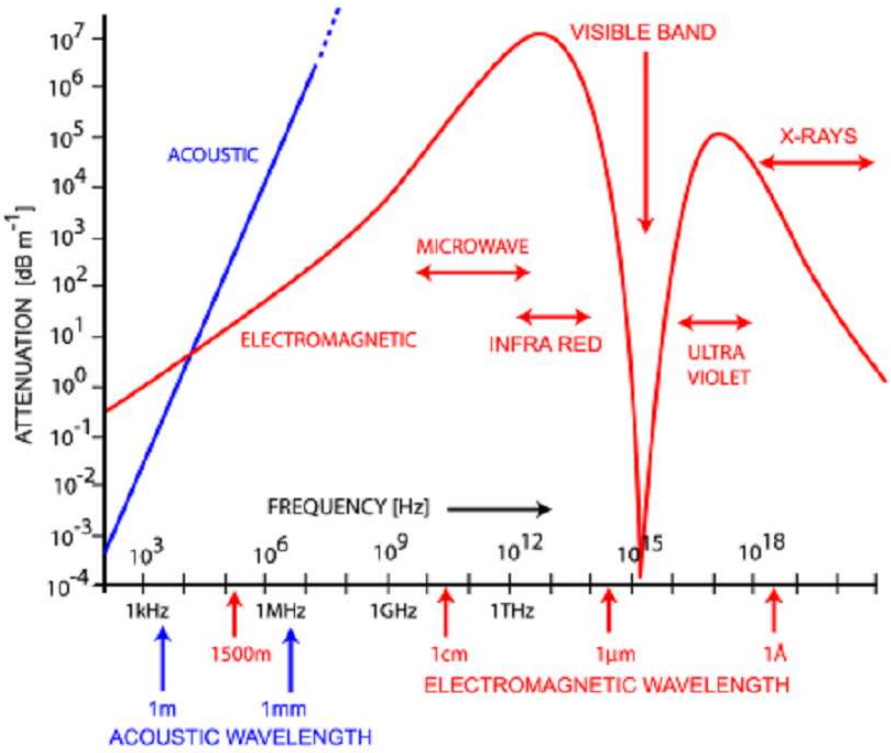

Figure B.1: Attenuation of Electromagnetic and Acoustic Waves in Seawater

The traditional RF wireless communication systems uses electromagnetic waves as the physical medium for data transfer. Such an eventuality is ruled out in the case of underwater wireless systems due to the large attenuation offered by the acoustic medium to electromagnetic waves (Coates, 2002). Fig. B.1[1] illustrates the typical attenuation characteristics offered by seawater for both electromagnetic waves and acoustic waves.

[1]Fig. B.1 is adapted from (Coates, 2002)

It can be seen that for all practical purposes, the attenuation profile of electromagnetic waves is unacceptable for any reasonable desirous range performance. Note also the increased attenuation (almost linear) with increase in frequency in the case of acoustic waves also. The main inference to be made is that the range performance of an underwater communication system has primarily to do with the choice of the carrier frequency bands which are used for the data transmission. In addition to the transmission loss which we will deal in detail in the next section, there is also the phenomenon of reverberation and scattering (Uricks, 1975). More serious is the multipath which is prevalent in shallow waters. The presence of the multipath will lead to a range-data rate trade off or range-dependant capacity for the underwater acoustic channel (Stojanovic, 2006).

B.1 Attenuation

A distinguishing property of acoustic channels is the fact that path loss depends on the signal frequency. This dependence is a consequence of absorption (i.e., transfer of acoustic energy into heat).

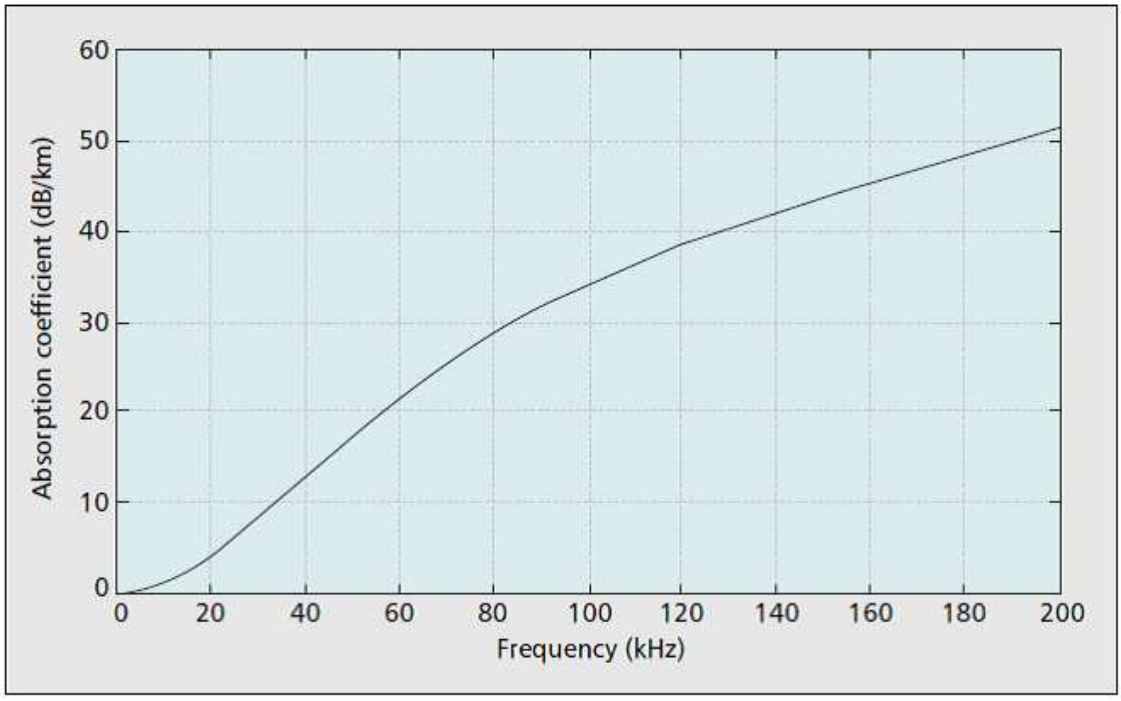

Figure B.2: Absorption coefficient, 10 log a(f) in dB/km.

In addition to the absorption loss, the signal experiences a spreading loss, which

increases with distance. The overall path loss is given by (Stojanovic, 2009)

$$A(l, f) = (l/l_r)^k a(f)^{l-l_r} \tag{B.1}$$

where f is the signal frequency and l is the transmission distance, taken in reference to some l_r. The path loss exponent k models the spreading loss, and its usual values are between 1 and 2 (for cylindrical and spherical spreading, respectively). The absorption coefficient $a(f)$ can be obtained using an empirical formula (L. Berkhovskikh and Lysanov, 1982). Fig. B.2[2] illustrates its rapid increase with frequency.

B.2 Ambient Noise

The main sources of ambient noise in ocean are turbulence, shipping, surface agitation (wave action) and thermal noise. The ocean ambient noise is seen to have typical $1/f$ frequency spectral characteristics at lower frequency range. While this noise is often approximated as Gaussian, it is not white. Unlike ambient noise, site-specific noise often contains significant non-Gaussian components. The typical deep water ambient spectrum noise level is indicated in Fig. B.3[3]. The power spectral density of ambient noise decays at a rate of approximately 18 dB/decade The following empirical relations give the power spectral density of the four noise components in $dB\ re\ 1\mu Pa/Hz$ as a function of the frequency in kHz (Chitre, 2007),(W. B. Yang and Yang, 2006), (Preisig, 2007).

An acoustic signal propagates as a pressure wave, whose power is measured in Pascals (commonly, in dB relative to a micro Pascal). In seawater, 1 W of radiated acoustic power creates a sound field of intensity $172dB\ re\ \mu Pa\ @1m$ away from the source.

[2]Fig. B.2 is adapted from (Stojanovic, 2009)
[3]Fig. B.3 is adapted from (Coates, 2002)

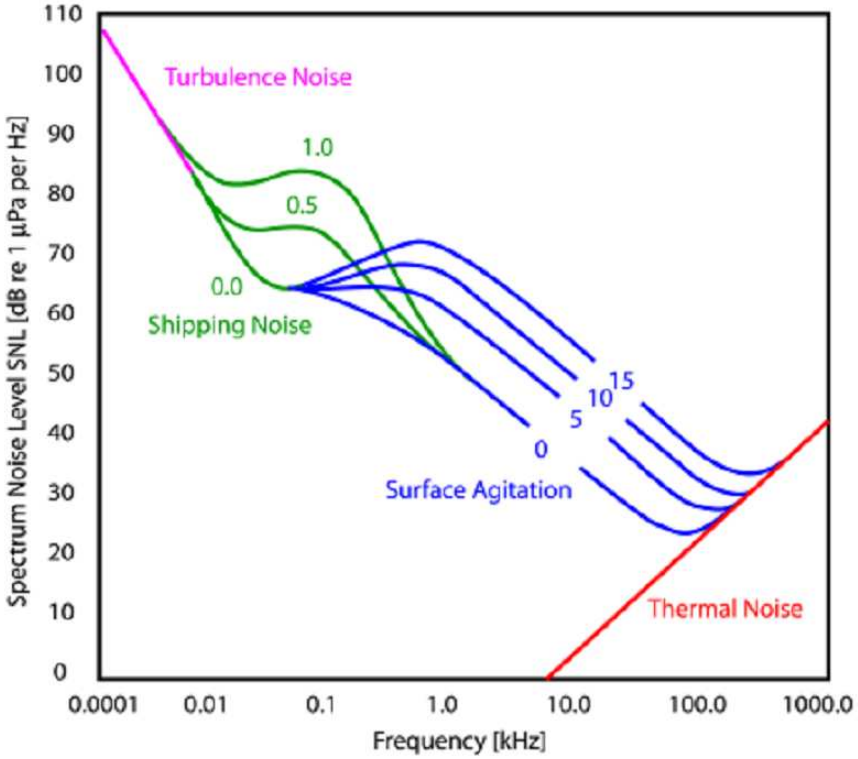

Figure B.3: Ambient Spectrum Noise Level

$$10logN_t(f) = 17 - 30log(f) \tag{B.2a}$$

$$10logN_s(f) = 40 + 20(s - 0.5) + 26log(f) - 60log(f + 0.3) \tag{B.2b}$$

$$10logN_w(f) = 50 + 7.5w^{0.5} + 20log(f) - 40log(f + 0.4) \tag{B.2c}$$

$$10logN_{th}(f) = -15 + 20log(f) \tag{B.2d}$$

where the variable$s$ is an indication of the shipping activity which takes values in the range (0,1), the variable w is the wind speed in m/s. The overall p.s.d of the ambient noise$N(f) = N_t + N_s + N_w + N_{th}$ is as illustrated above. The spatial variability of the ambient noise is another factor which has to be considered. The range of ambient noise capable of corrupting the communication system is given in Fig. B.4[4].

The locations at which the system is to be deployed will influence the noise margins to be considered at the design stage. Taking into consideration, the actual transmission

[4]Fig. B.4 is adapted from (Coates, 2002)

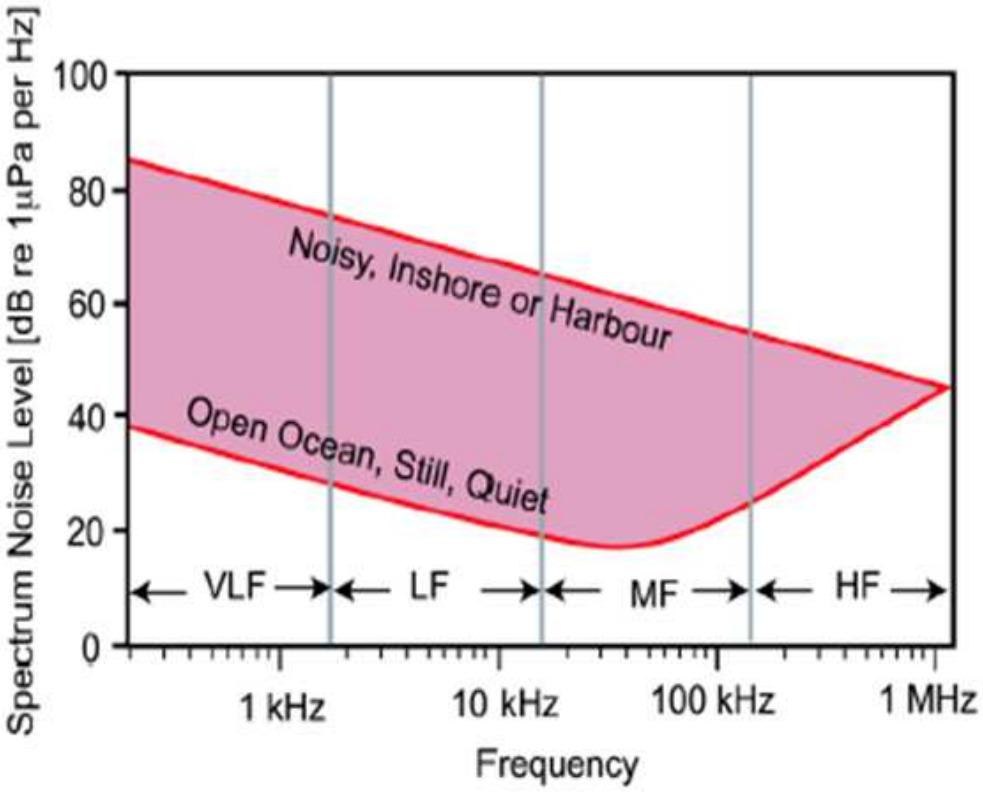

Figure B.4: Location Dependence of Ambient Spectrum Noise Level.*Adapted from (Coates, 2002)*

bandwidth B Hz, the noise level can be computed as

$$NL = NSL + 10log_{10}(B) \tag{B.3}$$

B.3 Maximum Achievable Range

In the earlier section, it was mentioned that the carrier signal attenuation is dependent on the transmitting frequency. The following Fig. B.5[5] illustrates the maximum achievable range as a function of the transmitting frequency. It can be seen from the plot that the carrier frequency influences the design of the acoustic modem significantly. The choice of the hardware and transducers will be critically influenced by this single factor. A practical implication of this is that depending on the applications requirements, range must be decided before hand while designing a particular underwater wireless system. Moreover, Coates mentions that "Once attenuation loss sets in, a threshold develops

[5]Fig. B.5 is adapted from (Coates, 2002)

after which there is no advantage to be gained by trying to attain greater range by pumping in more power" (Coates, 1989).

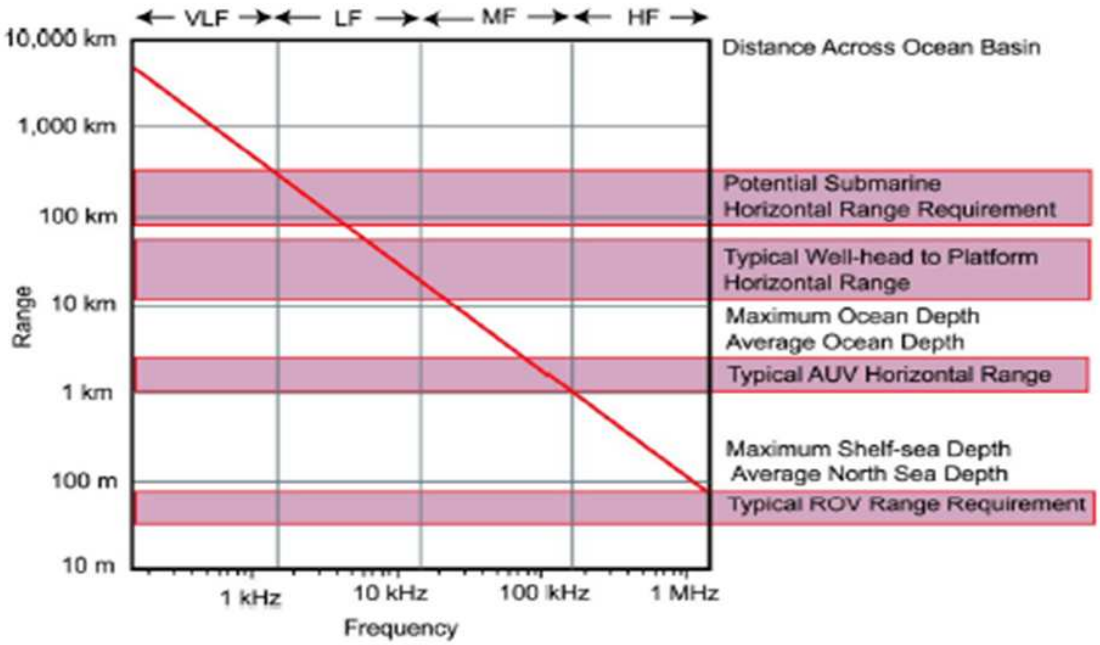

Figure B.5: Maximum Achievable Range as a function of Frequency

Another important factor to be considered is the variation of maximum achievable range as a function of transmitted power. There exists a range of required power from a best possible scenario to a worst possible scenario for a given carrier frequency. The choice of the projector and receiving hydrophone (whether directive) also influences the system. Fig. B.6[6] illustrates the relation of range as a function of transmitted frequency and power of transmission for two separate cases. In the first case, the left side of the graph gives the value of required power assuming that there is no directive gain from the transducers.

The right side of the graph gives the required power assuming a directive gain of 20 dB. The graph can be used as follows: if the required range is 2 Km, from the plot, we can infer that the maximum allowable frequency is 100 kHz. The worst case power is of the order of 1 W and the best case power is of the order of 1mW which depends on the environmental conditions.

The attenuation, which grows with frequency, and the noise, whose spectrum decays with frequency, result in a signal-to-noise ratio (SNR) that varies over the signal band-

[6]Fig. B.6 is adapted from (Coates, 2002)

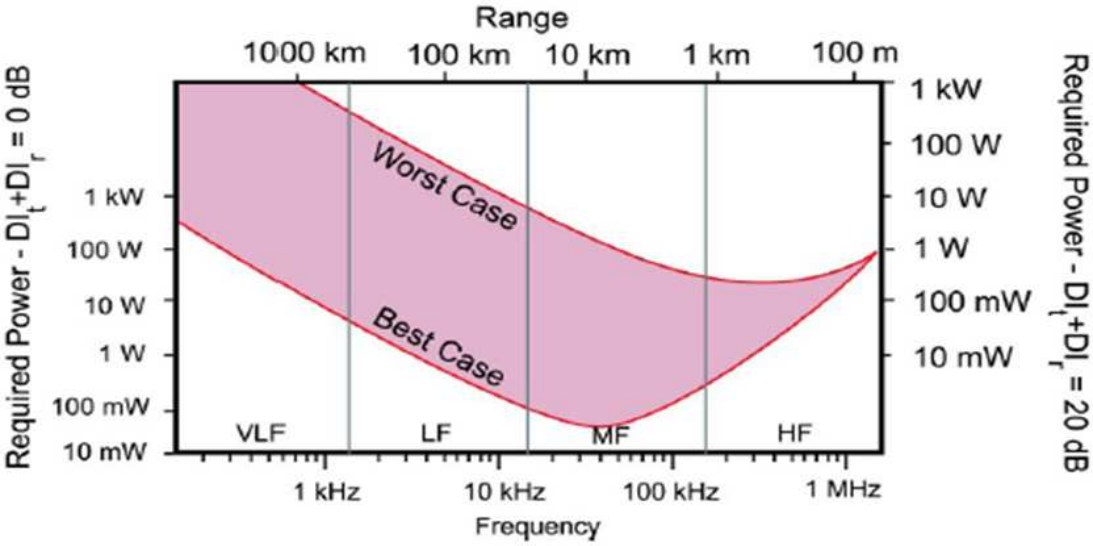

Figure B.6: Maximum Achievable Range as a function of Transmitted Power

width. If one defines a narrowband of frequencies of width Δf around some frequency f , the SNR in this band can be expressed as

$$SNR(l, f) = S_f / A(l, f) N(f) \tag{B.4}$$

where $S_l(f)$ is the power spectral density of the transmitted signal. For any given distance, the narrowband SNR is thus a function of frequency, as shown in Fig. B.7.

From Fig. B.7[7] it is apparent that the acoustic bandwidth depends on the transmission distance. In particular, the bandwidth and power needed to achieve a pre-specified SNR over some distance can be approximated as $B(l) = bl^{-b}, P(l) = pl^{y}$, where the coefficients b, p and the exponents$\beta \in (0, 1), y \geq 1$ depend on the target SNR, the parameters of the acoustic path loss, and the ambient noise (Stojanovic, 2006). The bandwidth is severely limited at longer distances: at 100 km, only about 1kHz is available. At shorter distances, the bandwidth increases, but will ultimately be limited by that of the transducer. The fact that bandwidth is limited implies the need for bandwidth-efficient modulation methods if more than 1 b/s/Hz is to be achieved over these channels.

[7]Fig. B.7 is adapted from (Stojanovic, 2009)

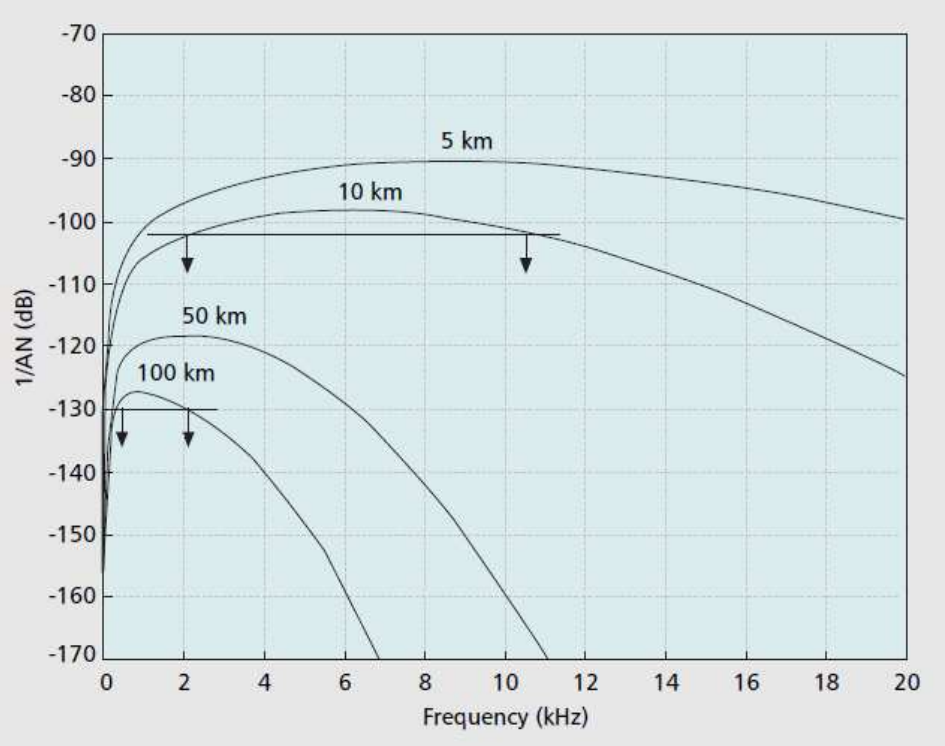

Figure B.7: Signal-to-noise ratio in an acoustic channel depends on the frequency and distance through the factor $1/A(l, f)N(f)$

B.4 Multipath

Multipath formation in the ocean is governed by two effects: sound reflection at the surface, bottom, and any objects, and sound refraction in the water. The latter is a consequence of the spatial variability of sound speed. Fig. B.8[8] illustrates the two mechanisms.

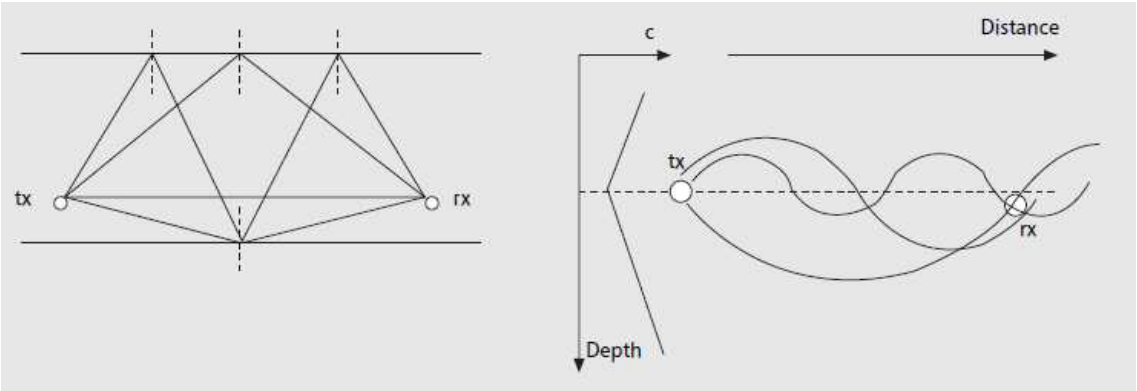

Figure B.8: Multipath formation in shallow and deep water.

Typical sound speed profile as a function of depth and the corresponding ocean

[8]Fig. B.8 is adapted from (Stojanovic, 2009)

cross-section is shown in Fig. B.9[9]

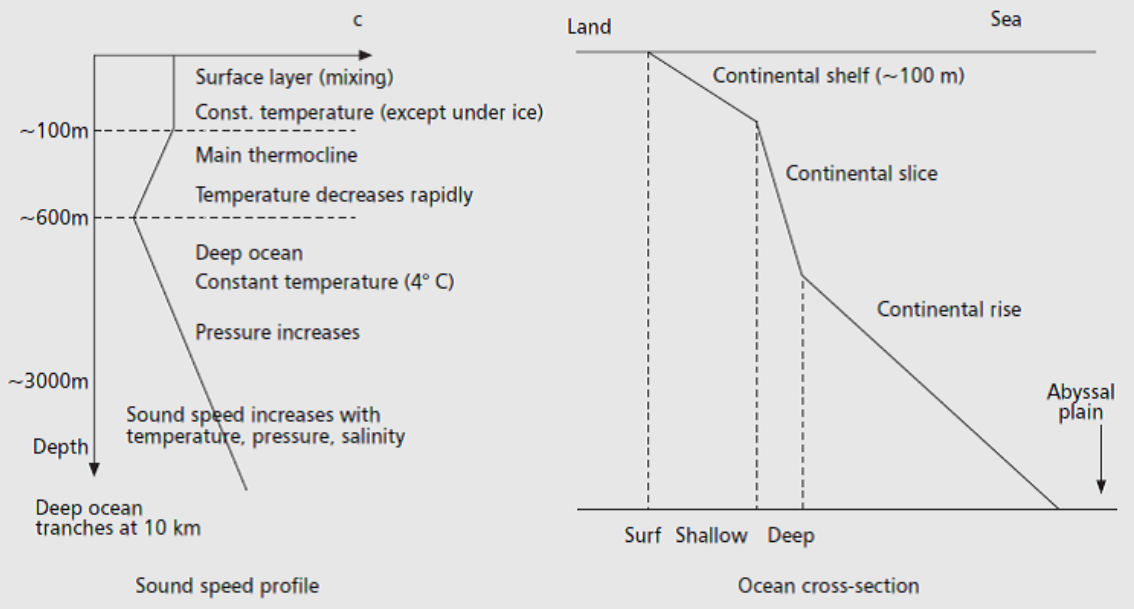

Figure B.9: Sound speed as a function of depth and the corresponding ocean cross-section

The sound speed v is controlled by two physical properties of the medium, namely its bulk modulus, K and its density,. The inter-relationship between these various quantities is given by the following equation, which is attributed to Newton.

$$v = \sqrt{K/\rho} \tag{B.5}$$

In distilled water at 20 degree C and at standard atmospheric pressure, the sound speed is 1481 m/s. In practice, constraints in measurement accuracy of K and ρ limit the value of this equation in providing a prediction of sound speed. It is, perhaps, sufficient to note that both density and elasticity are quantities which depend upon temperature, T, pressure, P and, for sea-water, chemical composition. Chemical composition is typically expressed in terms of salinity, S and more recently in terms of electrical conductivity, G. Consequently, sound speed may be expressed, to adequate accuracy, as some suitable function of temperature, pressure (or depth, Z) and salinity (or conductivity). i.e., $v = f(T, P, S)$, which vary with depth and location; and a ray of sound always bends toward the region of lower propagation speed, obeying Snell's law. Near the surface, both the temperature and pressure are usually constant, as is the sound speed.

[9]Fig. B.9 is adapted from (Stojanovic, 2009)

In temperate climates the temperature decreases as depth begins to increase, while the pressure increase is not enough to offset the effect on the sound speed. The sound speed thus decreases in the region called the main thermocline. After some depth, the temperature reaches a constant level of 4^0C, and from there on, the sound speed increases with depth (pressure). When a source launches a beam of rays, each ray will follow a slightly different path, and a receiver placed at some distance will observe multiple signal arrivals. Note that a ray travelling over a longer path may do so at a higher speed, thus reaching the receiver before a direct stronger ray. This phenomenon results in a non-minimum phase channel response.

B.5 Time Variability

There are two sources of the channel's time variability: inherent changes in the propagation medium and those that occur because of the transmitter/receiver motion. Inherent changes range from those that occur on very long time-scales that do not affect the instantaneous level of a communication signal (e.g., monthly changes in temperature) to those that occur on short time-scales and affect the signal. Prominent among the latter are changes induced by surface waves, which effectively cause the displacement of the reflection point, resulting in both scattering of the signal and Doppler spreading due to the changing path length. Unlike in a radio channel, where a number of models for both the probability distribution (e.g., Rayleigh fading) and the power spectral density of the fading process (e.g., the Jakes' model) are well-accepted and even standardized, there is no consensus on statistical characterization of acoustic communication channels. Experimental results suggest that some channels may just as well be characterized as deterministic, while others seem to exhibit Ricean or Rayleigh fading (Chitre, 2007). However, current research indicates K-distributed fading in other environments (Preisig, 2007). Channel coherence times below 100 ms have been observed (M. Stojanovic and Proakis, 1993) but not often. For a general-purpose design, one may consider coherence times on the order of hundreds of milliseconds. In the absence of good statistical models for simulation, experimental demonstration of candidate communication schemes remains the only option.

APPENDIX C

Derivation of CRLB for the Estimation of Packet Duration

The derivation of (2.58) is given in this appendix.

C.1 ML Estimator for Delay (Range): CRLB

We have seen that the Doppler parameter $'a'$ can be estimated from the received packet length. This brings us to the most critical analysis-that of finding a maximum likelihood (ML) estimator for the received packet length. We have derived from first principles, a scheme which in addition being analytically tractable with respect to performance parameters is also compact and efficient with respect to implementation. The signals that are used as preamble/postamble need to have some desirable properties which will be discussed in detail. As a first step, we will use the results for ML estimation of range/delay and obtain the expression for it's Cramer Rao Lower Bound(CRLB). This part of derivation is based on well-known theory (Kay, 1995). As the second step, we derive the ML estimator of the received packet length.

If a single pulse is transmitted, the trip delay τ_0 from the transmitter to the receiver is related to the distance R as $\tau_o = R/c_s$ where c_s is the velocity of sound propagation. Given that $s(t)$ is transmitted, a simple model for the received continuous waveform assuming an observation interval T is

$$x(t) = s(t - \tau_0) + w(t) \qquad 0 \leq t \leq T \tag{C.1}$$

The transmitted signal pulse is assumed to be non-zero over the interval $[0, T_p]$ with a bandwidth of B Hz. Here we have neglected the doppler scale $'a'$ for the pulse of duration T_p. If we bound the maximum delay to τ_{0max}, then the observation interval is chosen so as to include the entire signal by letting $T = T_p + \tau_{0max}$. The noise is

modelled as band-limited Gaussian with a bandwidth B Hz. The continuous received waveform is sampled at the Nyquist rate (samples taken at ever $\Delta = 1/(2B)$ seconds) to form the observed data

$$x(n) = s(n\Delta - \tau_0 + w(n)) \qquad n = 0, 1, \ldots, N-1 \tag{C.2}$$

The additive noise $w[n]$ is IID since the samples are separated by $k\Delta = k/(2B)$ which corresponds to the zero crossings of the auto correlation function of $w(t)$ (Kay, 1995). For independence in the case of Gaussian process, interrelatedness is sufficient. Due to the band-limiting, the variance of the noise $\sigma_w = N_0 B$ where N_0 is the power spectral density of the unfiltered noise process. The discrete model for the received signal can be written as

$$x[n] = \begin{cases} w[n]; & 0 \leq n \leq n_0 - 1 \\ s(n\Delta - \tau_0) + w[n]; & n_0 \leq n \leq n_0 + Np \\ w[n]; & n_0 + N_p \leq n \leq N - 1 \end{cases} \tag{C.3}$$

where N_p is the length of the sampled signal and $n_0 = \tau_0/\Delta$ is the delay in samples. We assume that Δ is small so that n_0 can be approximated by an integer value. Due to IID nature of the additive Gaussian noise, The likelihood PDF can be written as

$$\begin{aligned} p(x; n_0) = & \prod_{n=1}^{n_0-1} \frac{1}{\sqrt{2\pi\sigma^2}} exp\left[-\frac{1}{2\sigma^2} x^2[n]\right] \\ & \prod_{n=n_0}^{n_0+N_p-1} \frac{1}{\sqrt{2\pi\sigma^2}} exp\left[-\frac{1}{2\sigma^2}(x[n] - s[n-n_0])^2\right] \\ & \prod_{n=n_0+N_p}^{N-1} \frac{1}{\sqrt{2\pi\sigma^2}} exp\left[-\frac{1}{2\sigma^2} x^2[n]\right] \end{aligned} \tag{C.4}$$

The likelihood function gets simplified by collecting the common terms as

$$\begin{aligned} p(x; n_0) = & \frac{1}{(2\pi\sigma^2)^{N/2}} exp\left[-\frac{1}{2\sigma^2} \sum_{n=0}^{N-1} x^2[n]\right] \\ & \prod_{n=n_0}^{n_0+N_p-1} exp\left[-\frac{1}{2\sigma^2}(-2x[n]s[n-n_0] + s^2[n-n_0])\right] \end{aligned} \tag{C.5}$$

The MLE n_0 is the argument that maximizes the term

$$\arg\max_{n_0} \left\{ exp \left[-\frac{1}{2\sigma^2} \sum_{n=n_0}^{n_0+N_p-1} \left(-2x[n]s[n-n_0] + s^2[n-n_0] \right) \right] \right\} \tag{C.6}$$

or equivalently the argument that minimizes the term

$$\arg\min_{n_0} \left\{ \sum_{n=n_0}^{n_0+N_p-1} \left(-2x[n]s[n-n_0] + s^2[n-n_0] \right) \right\} \tag{C.7}$$

The term $\sum_{n=n_0}^{n_0+N_p-1} s^2[n-n_0] = \sum_{n=n_0}^{N_p-1} s^2[n]$ is not a function of n_0. Hence the MLE of n_0 is the argument that maximizes the term

$$\arg\max_{n_0} \left\{ \sum_{n=n_0}^{n_0+N_p-1} \left(x[n]s[n-n_0] \right) \right\} \tag{C.8}$$

Note that the MLE of the delay n_0 is obtained by correlating the data with all the possible received signals and then choosing the index at which the correlation attains the maximum. The Cramer Rao lower bound for the estimator can be derived as follows: The CRLB is given by the expression

$$var(\hat{\theta}) \geq \frac{\sigma^2}{\sum_{n=0}^{N-1} \left(\frac{\partial s[n;\theta]}{\partial \theta} \right)^2} \tag{C.9}$$

where θ is the parameter of interest and the measurement model is given by

$$x[n] = s[n;\theta] + w[n] \qquad n = 0, 1, \cdots, N-1 \tag{C.10}$$

σ is the variance of the additive white Gaussian noise. The dependence of the signal on the parameter θ is explicitly given by the likelihood function

$$p(x;\theta) = \frac{1}{(2\pi\sigma^2)^{N/2}} exp \left\{ -\frac{1}{2\sigma^2} \sum_{n=0}^{N-1} \left(x[n] - s[n;\theta] \right)^2 \right\} \tag{C.11}$$

Substituting (C.3) in (C.10), we get

$$\begin{aligned} var(\hat{\tau_0}) &\geq \frac{\sigma^2}{\sum_{n=0}^{N-1}\left(\frac{\partial s[n;\tau_0]}{\partial \tau_0}\right)^2} = \frac{\sigma^2}{\sum_{n=n_0}^{n_0+N_p-1}\left(\frac{\partial s[n\tau-\tau_0]}{\partial \tau_0}\right)^2} \\ &= \frac{\sigma^2}{\sum_{n=n_0}^{n_0+N_p-1}\left(\frac{ds(t)}{dt}|_{t=n\Delta-\tau_0}\right)^2} = \frac{\sigma^2}{\sum_{n=0}^{N_p-1}\left(\frac{ds(t)}{dt}|_{t=n\Delta}\right)^2} \end{aligned} \tag{C.12}$$

since $\tau_0 = n_0\Delta$. We can assume Δ is small so that the discrete sum can be replaced by the integral to obtain[1]

$$var(\hat{\tau_0}) \geq \frac{\sigma^2}{\frac{1}{\Delta}\int_0^{T_p}\left(\frac{ds(t)}{dt}\right)^2} \tag{C.13}$$

Noting that $\Delta = 1/(2B)$ and $\sigma^2 = N_0 B$, we get

$$var(\hat{\tau_0}) \geq \frac{N_0/2}{\int_0^{T_p}\left(\frac{ds(t)}{dt}\right)^2} \tag{C.14}$$

The energy ε of a pulse $s(t)$ is given by $\varepsilon = \int_0^{T_p} s^2(t)dt$ The term $\frac{\varepsilon}{(N_0/2)}$ is the SNR of the pulse signal (H. L. VanTrees, 2001). If $S(f)$ is the Fourier transform of $s(t)$, the mean square bandwidth of the signal B^2 is given by

$$B = \frac{\int_{-\infty}^{\infty}(2\pi f)^2|S(f)|^2 df}{\int_{-\infty}^{\infty}|S(f)|^2 df} \tag{C.15}$$

By using the properties of the Fourier transform, the above expression can be written as

$$B = \frac{\int_0^{T_p}\left(\frac{ds(t)}{dt}\right)^2 dt}{\int_0^{T_p} s^2(t)dt} \tag{C.16}$$

On substituting in (C.14), we get

$$var(\hat{\tau_0}) \geq \frac{1}{\left(\frac{\varepsilon}{N_0/2}\right)}B \tag{C.17}$$

[1]The transformation from (C.12) to (C.13) is obtained by the Riemann integral $\int_a^b g(x)dx \cong \sum_{n=0}^{N-1}\left\{\int_{x_n}^{x_{n+}} g(x)dx\right\} \cong \sum_{n_1=0}^{N-1}\Delta g(x_{n1})$ where n_1 is the midpoint of $[(n+1), n]$. $\Longrightarrow \frac{1}{\Delta}\int_a^b g(x)dx \cong \sum_{n_1=0}^{N-1} g(x_{n1})$

[2]for all practical purposes, we can consider the mean square bandwidth as the same as the bandwidth of the signal

From the expression in (C.17) it is clear that for a large bandwidth signal, the lower will be the Cramer Rao lower bound in the variance. This result is of utmost importance and we will use the same in deriving the high resolution ML Doppler scale estimator $'a'$.

C.2 ML Estimator for Packet Length

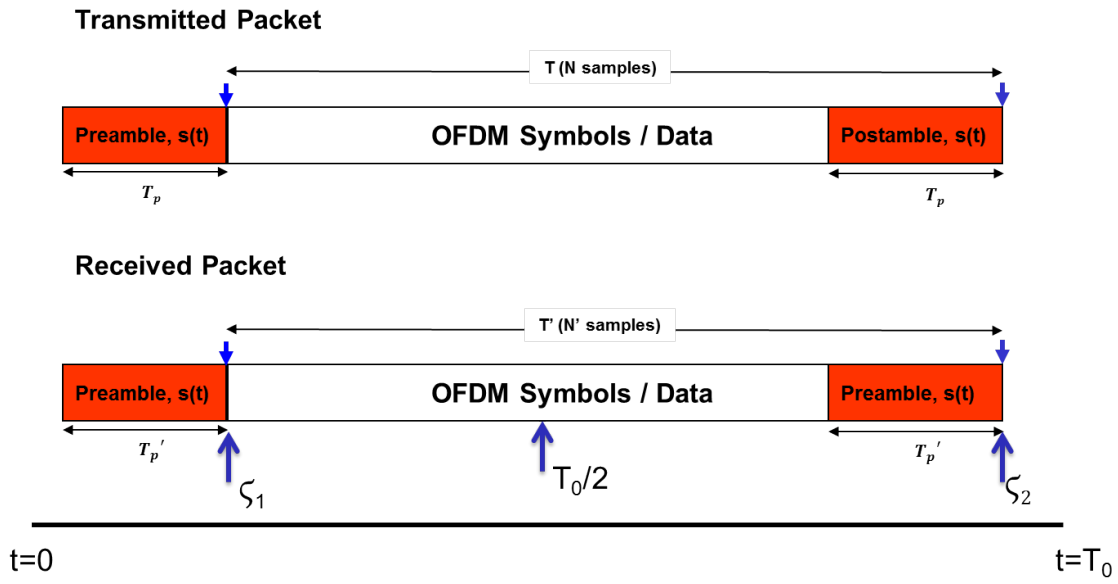

Figure C.1: ML Estimator for Received packet Length

With reference to Fig. C.1, the transmitted signal $x(t)$ is composed of two pulses of the signal waveform $s(t)$ with pulse width T_p seconds. The separation between them is T seconds. The pulses are transmitted and received. Due to the relative velocity the pulse width as well as the separation changes to T_p' and T' respectively. The received signal $y(t)$ can be expressed as

$$y(t) = x(t) + n(t) \tag{C.18}$$

where $n(t)$ is AWGN distributed as $N(0, \sigma^2)$. Consider the scenario as given in Fig. C.1, there are two pulses of width $T_p'(N_p'$ samples) separated by a distance T' (N' samples). It is needed to estimate T' given that we know all the properties of the pulse waveforms. The observation interval T_0 (N_0 samples) is chosen so as to encompass both the pulses and also ensuring that at least one pulse is within the time interval $T_0/2$. Given the measured signal $y(t)$ over the observation interval T_0, the ML estimator of T' can be

written as

$$T' = \frac{T_0}{2} + \arg\max_{\zeta} \left\{ \int_0^{T_p} y(t)s(t-\zeta)dt \right\}_{\frac{T_0}{2} \leq t \leq T_0} - \arg\max_{\zeta} \left\{ \int_0^{T_p} y(t)s(t-\zeta)dt \right\}_{0 \leq t \leq \frac{T_0}{2}} \tag{C.19}$$

Note that the time of integration is T_p since we are correlating with the original transmitted signal $s(t)$. In discrete time, the above expression can be written as

$$N' = \frac{N_0}{2} + \arg\max_{m} \left\{ \sum_{0}^{N_p-1} y[i]s[i-m]dt \right\}_{\frac{N_0}{2}+1 \leq i \leq N_0} - \arg\max_{m} \left\{ \sum_{0}^{N_p-1} y[i]s[i-m]dt \right\}_{0 \leq i \leq \frac{N_0}{2}} \tag{C.20}$$

On comparing (C.17) and (C.20), we can see that the ML estimator of the Packet length can be interpreted in terms of two independent range/delay measurements. From Fig. C.1, we also know that the relative movement in the time duration between the pulses causes the time scaling effect. Thus the two pulses get received from two separate ranges due to the motion of the receiver. This observation is going to play a very crucial role in the choice of the waveform for the transmit pulses. The notion of two independent measurements is very critical and necessary. From the mathematical expression in (C.20), we can infer that the two range/propagation delay measurements individually will have a CRLB as given in (C.17). Since the measurements are independent, the variances will add up for the packet length estimate. The Cramer Rao lower bound for the packet length estimate is thus given by

$$var(\hat{T}') \geq \frac{2}{\left(\frac{\varepsilon}{N_0/2}\right)} B \tag{C.21}$$

As in the case of delay estimation, we see that the signal bandwidth is a critical parameter in deciding the estimator accuracy. The CRLB expression does not give any insight into other desirable properties that the waveform should possess.

REFERENCES

1. **A. Batra, G. R. A. J. R. F., J. Balakishnan** and **A. Dabak** (2004). Design of a multi-band ofdm system for realistic uwb channel environments. *IEEE Transactions on Microwave Theory and Technique*, **52**(9), 2123 – 2138.

2. **Anthony G. Bessios** and **F. M. Caim** (1996). High rate wireless data communications: An underwater acoustic communications frame work at the physical layer. *Mathematical Problems in Engineering*, **2**(6), 449–485.

3. **Arthur B. Baggeroer** (1984). Acoustic telemetry: An overview. *IEEE Journal of Oceanic Engineering*, **9**(4), 229–235.

4. **B. Muquet**, **Z. Wang**, **G. B. Giannakis**, **M. de Courville**, and **P. Duhamel** (2002). Cyclic prefix or zero-padding for multi-carrier transmissions? *IEEE Transactions on Communications*, **50**(12), 2136 – 2148.

5. **B. Sharif**, **J. Neasham**, **O. R. Hinton**, and **A. E. Adams** (2000). A computationally efficient doppler compensation system for underwater acoustic communications. *IEEE Journal of Oceanic Engineering*, **25**(1), 52 – 60.

6. **Bojan Dimitrijevic**, **S. Stosovis**, **N. Milosevic**, and **Z. Nikolic** (2011). Influence of frequency offset on the reception of ofdm/qpsk signal using mbdd algorithm. *Telfor Journal*, **3**(2), 2908 – 2914.

7. **Chaiyasena, A. P.**, **L. H. Sibul**, and **A. Banyaga**, Wavelet transforms, wideband ambiguity functions and group theory. *In 6th Asilomar Conference on Signals, Systems, and Computers*. 1992.

8. **Chitre, M.** (2007). A high-frequency warm shallow water acoustic communications channel model and measurements. *J. Acoust. Soc. America*, **122**(5), 2580–2586.

9. **Christian Meinig**, **S. E. Stalin**, **A. I. Nakamura**, **F. Gonzalez**, and **H. B. Milburn** (2006). Technology developments in real time tsunami measuring, monitoring and forecasting. *Technical report, NOAA, Pacific Marine Environmental Laboratory*.

10. **Christian Meinig**, **S. E. Stalin**, **A. I. Nakamura**, and **H. B. Milburn** (2005). Real time deep ocean tsunami measuring, monitoring and reporting system: Noaa dart ii description and disclosure. *Technical report, NOAA, Pacific Marine Environmental Laboratory*.

11. **Coates, R.**, *Underwater Acoustic Systems*. Wiley, 1989.

12. **Coates, R.**, *Advanced Sonar Course*. Seiche Publisher, 2002.

13. **Cook, C. E.** and **M. Bernfeld**, *Radar Signals: An Introduction to Theory and Application*. Academic Press, New York, 1967.

14. **Cook, C. E.** and **W. M. Seibert** (1988). The early history of pulse compression radar. *IEEE Transactions on Aerospace and Electronic Systems*, (6), 825 – 837.

15. **C.W. Farrow**, A continuously variable digital element. *In Proc IEEE Int. Symp. Circuits and Systems,(ICAS-88)*. 1988.

16. **E.J. Kelly** and **R. Wishner** (1965). Matched-filter theory for high-velocity,accelerating targets. *IEEE Trans Mil Electron*, (9), 56 – 657.

17. **Eric T. M. Law**, **R. Bradbeer**, **L. F. Yeung**, **L. Bin**, **G. ZhongGuo**, and **T. H. T. Kwan.**, Using multicarrier modulation in an ultrasonic data link to communicate with an underwater vehicle. *In IEEE International Conference in Mechatronics and Machine Vision in Practise*. IEEE, 2002.

18. **F. Classen** and **H. Meyr**, Frequency synchronization algorithms for ofdm systems suitable for communication over frequency-selective fading channel. *In in Proc. 44th Vehicular Technology Conf.*. 1994.

19. **Feher, K.**, *Wireless Digital Communications*. Prentice Hall, 1996.

20. **Goldsmith, A.**, *Wireless Communications*. Cambridge University Press, 2005.

21. **H. Jafarkhani** and **V. Tarokh** (2001). Multiple transmit antenna differential detection from generalized orthogonal designs. *IEEE Trans. Inf. Theory*, **47**(7), 2626 –2631.

22. **H. L. VanTrees**, *Detection, Estimation and Modulation Theory, Part - 1*. Wiley, 2001.

23. **Harris, F.**, Forming arbitrary length windows or filter sequences from a fixed length reference table. *In 18-th Annual Asilomar Conf. on Circ, Syst, and Computers*. 1984.

24. **Islam, S.**, **N. Al-Dhahir**, **H. Minn**, and **S. Lu** (2007). Comparison of time and frequency domain single and double differential schemes for ofdm uwb systems. *Sarnoff Symposium Nassau Inn, Princeton, NJ*, 1 – 5.

25. **J. G. Proakis**, **J. A. Rice**, and **M. Stojanovic** (2001). Shallow water acoustic networks. *IEEE Communications Magazine*, 234–250.

26. **J. Yang** and **T. K. Sarkar** (2006). Doppler-invariant property of hyperbolic frequency modulated waveforms. *Microwave and Optical Technology Letters*, **48**(6), 1174 – 1179.

27. **Joseph A. Rice**, **R. K. Creber**, **K. E. R. Christopher L. Fletcher, Paul A. Baxley**, and **D. C. Davison** (2005). Seaweb underwater acoustic nets. in proceedings of the international conference on underwater acoustic measurements: Technologies results. *IEE Radar, Sonar and Navigation*, 234–250.

28. **Kay, S.**, *Fundamentals of Statistical Signal Processing : Estimation Theory*. Prentice Hall, 1995.

29. **Kilfoyle, D.** and **A. Baggeroer** (2000). The state of the art in underwater acoustic telemetry. *IEEE Journal of Oceanic Engineering*, **25**(1), 4–27. ISSN 0364-9059.

30. **L. Auslander** and **I. Gertner** (1992). Wideband ambiguity function and ax+b group. signal processing : Part 1. *Signal Processing Theory*, 1 – 11.

31. **L. Berkhovskikh** and **Y. Lysanov**, *Fundamentals of Ocean Acoustics*. Springer, 1982.

32. **L. Liu**, **S. Zhou**, and **J. Cui** (2008). The prospects and problems of wireless communication for underwater sensor networks. *Wiley WCMC Special Issue on Underwater Sensor Networks*.

33. **M. Simon** and **D. Divsalar** (1992). On the implementation and performance of single and double differential detection schemes. *IEEE Trans. Commun.*, **40**(2), 278 – 291.

34. **M. Stojanovic, J. C.** and **J. Proakis** (1993). Adaptive multichannel combining and equalization for underwater acoustic communications. *J. Acoust. Soc. America*, **94**(3), 1621 – 31.

35. **M. Zheng**, **I. Wang**, **R. Stoner**, and **R. Coates** (1999). Underwater digital communication utilising parametric sonar with m ary dpsk modulation. *IEE Radar, Sonar and Navigation*, **146**(4), 213–218.

36. **Mommertz** and **S. Muller** (1995). Measuring impulse responses with digitally pre emphasized pseudorandom noise derived from maximum length sequences. *Applied Acoustics*, **44**(3), 195 – 214.

37. **Moose, P. H.** (1994). A technique for orthogonal frequency division multiplexing frequency offset correction. *IEEE Trans. Comm.*, **42**(10), 2908 – 2914.

38. **Okunev, Y. B.**, *Theory of Phase-Difference Modulation*. Svyaz Press, Moscow, 1979.

39. **Pent, M.** (1978). Doubly differential psk scheme in the presence of doppler shift. *Digital Communications in Avionics AGARD Proc*, **239**, 44–1 – 43–11.

40. **Preisig, J.** (2007). Acoustic propagation considerations for underwater acoustic communications network development. *ACM SIGMOBILE Mobile Comp. Commun. Rev*, **11**(4), 2–10.

41. **R. D. J. van Nee, M. M. H. T. M. A. W., G. A. Awater** and **K. W. Halford** (1999). New high-rate wireless lan standards. *EEE Communications Magazine*, **37**(12).

42. **Rice, M.**, *Digital Communications: A Discrete-Time Approach*. Pearson Prentice Hall, 2008.

43. **Rihaczek, A. W.**, *Principles of High Resolution Radar*. McGraw-Hill, New York, 1969.

44. **S. N. Diggavi**, **N. Al-Dhahir**, **A. Stamoulis**, and **A. R. Calderbank** (2002). Differential space-time coding for frequency-selective channels. *IEEE Commun. Lett*, **6**(6), 2626 –2631.

45. **Sinsky, A. I.** and **C. P. Wang** (1974). Standardization of the definition of the radar ambiguity function. *IEEE Transactions on Aerospace and Electronic Systems*, (4), 532 – 533.

46. **Stojanovic, M.** (1996). Recent advances in high speed underwater acoustic communications. *IEEE Journal of Oceanic Engineering*, **21**(2), 125–136.

47. **Stojanovic, M.**, On the relationship between capacity and distance in an underwater acoustic communication channel. *In WUWNet06, Los Angeles, California, USA*. IEEE, 2006.

48. **Stojanovic, M.** (2009). Underwater acoustic communication channels: Propagation models and statistical characterization. *IEEE Communications Magazine*, **47**(1), 84 – 89.

49. **T.P. SameerBabu**, **M. K. P**, **V. M.V**, and **Anand.P** (2007*a*). Ofdm based acoustic modem with adaptable delay spread compensation for underwater channels. *Proceedings of the International Symposium on Ocean Electronics (SYMPOL)*, 19 – 26.

50. **T.P. SameerBabu**, **M. K. P**, **V. M.V**, and **A. P** (2007*b*). Design and testing of a real time software defined radio based wireless acoustic modem prototype. *SEA TECH*, **4**, 1 – 15.

51. **Uricks, R. J.**, *Principles of Underwater Sound for Scientists and Engineers*. Mc Graw Hill, 1975.

52. **van Alphen, D.** and **W. C. Lindsey** (1994). Higher-order differential phase keyed modulation. *IEEE Transactions On Communications*, **42**(2).

53. **W. B. Yang** and **T. C. Yang** (2006). High-frequency channel characterization for m-ary frequency-shift-keying underwater acoustic communications. *J. Acoust. Soc. America*, **120**(5), 2615–2626.

54. **Weiss, L.** (1994). Wavelets and wideband correlation processing. *IEEE Signal Processing Magazine*, **11**(1), 13 – 32.

55. **Woodward, P. M.**, *Probability and Information Theory, with Applications to Radar*. Pergamon Press, Oxford, 1953.

56. **Z. Wang** and **G. B. Giannakis** (2000). Wireless multicarrier communications: Where fourier meets shannon. *IEEE Signal Processing Magazine*, **17**(3), 29 – 48.

57. **Zhiqiang Liu** and **G. B. Giannakis** (2001). Double differential spaceâĂŞtime block coding for time-selective fading channels. *IEEE Transactions On Communications*, **49**(9), 2626 –2631.

LIST OF PAPERS BASED ON THESIS

1. T.P. Sameer Babu, R.David Koilpillai, P. Murali Krishna, "Underwater Acoustic Communications: Design Considerations At the Physical Layer Based on Field Trials", *Eighteenth National Conference on Communications (NCC-2012) held at IIT Kharagpur, India, during 3-5 Feb 2012.*